Experimental investigation of wave coupling on a cylindrical shell with a keel

by

Patricia A. Manning

B.S. Mechanical Engineering 1987 MIT
M.S. Mechanical Engineering 1990 UC Berkeley

Submitted to the Department of Ocean Engineering in partial fulfillment of the requirements for the degree of

DOCTOR OF PHILOSOPHY in ACOUSTICS
at the
MASSACHUSETTS INSTITUTE OF TECHNOLOGY

FEBRUARY 1999

Signature of Author: .....
Department of Ocean Engineering
October 30, 1998

Certified by: .....
J. Kim Vandiver
Professor of Ocean Engineering
Thesis Supervisor

Accepted by: .....
J. Kim Vandiver
Chairman, Department Committee on Graduate Students

Experimental investigation of wave coupling on a cylindrical shell with a keel

by

Patricia A. Manning

Submitted to the Department of Ocean Engineering on October 30, 1998
in partial fulfillment of the requirements for the degree of
Doctor of Philosophy in Acoustics

ABSTRACT

Previous research has shown the importance of membrane waves to the radiation and scattering properties of submerged finite-length cylindrical shells. Membrane waves (shear and compressional) are the principal determinants of radiation and scattering in the mid-frequency (2<ka<12), high aspect angle (+/- 30 degrees of beam aspect) regimes because they are trace matched to sound waves in water. Conventional damping treatments are not effective in damping membrane waves, but they work well on out-of-plane flexural waves. This thesis studies the use of a circumferential discontinuity, a keel, to transfer membrane wave energy into flexural waves, where it can be dissipated.

This thesis shows that a longitudinal stiffener, or keel, couples mode 0 membrane waves to higher order flexural waves. Compressional and flexural mode 0 waves were excited on a cylindrical plastic shell using a circumferential source array. The source array was located in the middle of a long shell, and a keel was attached to one end of the shell. Longitudinal and circumferential array measurements were taken on each end of the shell. Wavenumber-frequency transforms were used to separate the data by modal order and wave type. The use of a plastic shell with high damping enabled measurement of direct and reflected wave amplitudes.

Data taken on the unmodified end of the shell were used to verify the functionality of the source array and to demonstrate the physics of wave propagation on cylindrical shells. Thick shell theory was shown to match the measured data. Data taken on the end with the keel were used to study wave coupling due to the keel. The keel introduces a new axial wave herein called the keel wave. Two mechanisms of coupling to higher order flexural waves are shown, one from the keel wave and one from the mode 0 compressional and flexural waves. The higher order flexural waves excited by these two mechanisms are measured and identified using both longitudinal and circumferential arrays. Wave coupling is shown to occur where the waves are trace matched along the keel.

Thesis Supervisor: J. Kim Vandiver
Title: Professor of Ocean Engineering

ACKNOWLEDGEMENTS

Dad, thank you for your interest in my work. I could not have done this without you. You and I must know more about waves on cylindrical shells than anyone in the world right now. Thank you for getting into it with me!

Kim, thank you for your constant support throughout my tenure at MIT. You helped me through the hard times with encouragement and understanding, and your advice was always empowering. Eduardo and Rama, thank you for being on my committee. It was a pleasure working with you. Ira, thank you for your part in helping me through this process. Thanks, Sheila for your wise remarks which always cheer me up. Thanks, Sabina for taking good care of me. Thank you to Professors Feng, Crandall, Leehey, and Fricke for sustaining the A&V community in spite of shrinking support from the Institute. Thank you to my LLNL support team: Jerry Gerich and Toni Nevis. Thank you to Brian Bonner for supporting me in the first two years - someday we'll write that paper. Thank you to Joe Weaver, for inspiration. Thank you to Cambridge Collaborative, Inc. for use of the SRS analyzer.

Mom and Dad, thank you for your love, guidance, inspiration, support... You were my first and most important teachers, and the learning continues! Thank you for enabling me to reach this goal. Mom, thank you for taking care of us, especially Madison, during the long days when I was finishing up.

Brad, thank you for sharing everything with me. You are always my biggest fan. And since I'm now a Doctor, we can finally settle it... I love you more!

Madison, thank you for putting it all in perspective. Everyone told me my priorities would change after you were born, but I didn't believe them. It turns out we were all right. My priorities did not change, but they all moved down a notch. You are my most precious (and most enjoyable) priority. I love you, Boo. (And thanks for your help in the lab!)

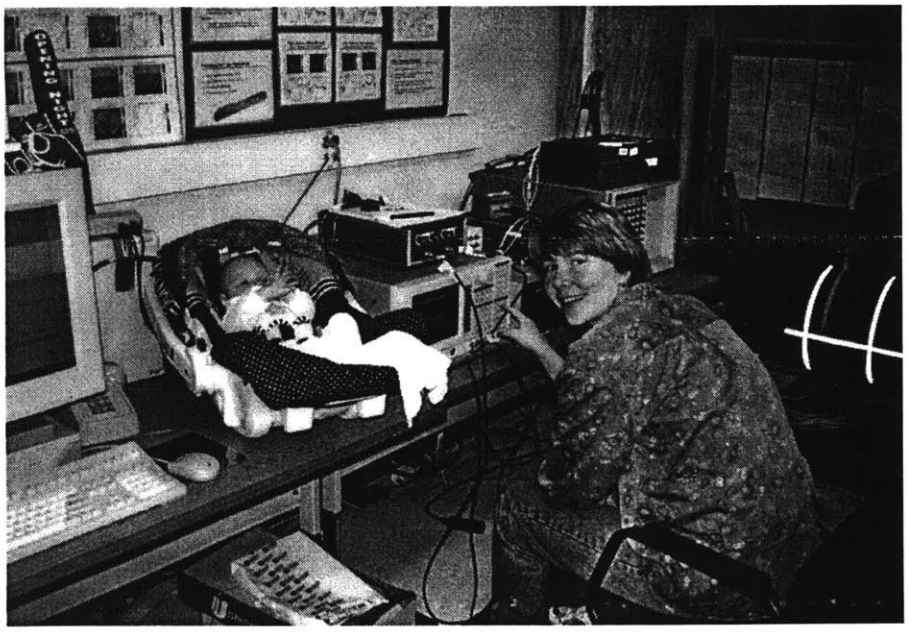

TABLE OF CONTENTS

LIST OF FIGURES

1. INTRODUCTION

The study of wave coupling in a cylindrical shell is motivated by the need for greater understanding of the structural-acoustic behavior of ships. Cylindrical shells are often used to model submarine hulls. They are also used to model ship piping. In both cases, the structural-acoustic behavior of these structures is important to the overall performance of the ship.

One problem of immediate interest is ship target strength, which controls the detectability of the ship. The scattering of incident acoustic waves by cylindrical shells bears a direct relationship to this problem. The incident acoustic waves excite structural vibration waves in the shell. The response and subsequent radiation of these waves has a major effect on the scattered acoustic field, particularly for non-specular observation angles.

A second problem of interest is ship radiated noise. Internal machinery and other ship components transmit vibratory energy to the hull where it is radiated to the acoustic far field and may be detected. The radiation properties of vibration waves on cylindrical shells relate directly to the calculation of hull radiated noise.

Membrane compressional and shear waves in the shell have been shown to have an important effect on scattering, particularly on back-scattering to the monostatic position for aspect angles between +/- 30 degrees of beam aspect (normal to the shell axis). Conversely, flexural waves have a small effect on the scattering. The phase velocity of the flexural waves is generally subsonic, so that they are weakly coupled to the incident acoustic field and inefficient radiators of sound.

Methods to reduce the response of the membrane waves merit consideration because of the importance of these waves to shell scattering. Use of visco-elastic materials to dampen the hull vibrations is common in ship design. However, these materials are found to be much more effective in damping the flexural waves than the membrane waves. Due to the high strain energy per unit displacement in the membrane waves, dissipation of membrane wave energy by typical damping treatments is ineffective.

The idea of converting the membrane wave energy to flexural wave energy is a promising idea for reducing membrane wave response, since the converted flexural wave energy can be dissipated by damping treatments. An infinite, homogeneous cylindrical shell provides no wave conversion mechanisms. However, addition of impedance discontinuities at the ends of the shell provides one technique for wave conversion. Impedance discontinuities along the shell in the form of ring stiffeners, bulkheads, and longitudinal stiffeners or keels also provide mechanisms for wave conversion. Unfortunately, these impedance discontinuities also increase the coupling of the flexural waves to the incident acoustic field, thereby increasing the subsequent response and re-radiation. It is unclear whether the benefit of reducing the response and radiation by membrane waves is outweighed by the detrimental effect of increasing the response and radiation by the flexural waves. The scattering of subsonic flexural waves at discontinuities is known to be a major source of radiated noise. Thus, any addition of structural discontinuities to the ship structure to reduce the scattered acoustic field may increase the radiated noise.

Previous measurements of the scattered pressure field of cylindrical shells with ring stiffeners and internal structures show a general increase in target strength due to the added discontinuities. On the basis of this result, one might conclude that the addition of a longitudinal stiffener, or keel would provide an added discontinuity and therefore increase target strength and acoustic radiation. However, the previous measurements did not include tests on shells with axial discontinuities, so this conclusion is open to question.

Analytical studies of the scattering by a cylindrical shell with both circumferential and axial discontinuities confirm the expected result that the discontinuities provide greater coupling to the incident acoustic field and greater radiation and scattering. In these studies, the increase in scattering is found to be due to an increase in the contribution of the flexural waves. However, the damping of the flexural waves is assumed to be small. It is recognized in one of the analytical studies that higher damping would make the increase due to the flexural waves less important.

The possibility of reducing the amplitude of the scattered acoustic field by converting the membrane wave energy to flexural wave energy and dissipating the flexural wave

energy so these waves do not contribute to the scattered field has not been demonstrated either from measured data or from analysis.

In this thesis, the use of a keel to convert membrane wave energy to flexural wave energy is explored experimentally. Measurements are carried out in air to reduce the cost that would be incurred by underwater scattering measurements. Membrane waves are excited in the shell by a circumferential array of piezoelectric transducers embedded in the shell wall. The keel provides a coupling mechanism whereby some of the energy in the membrane waves is converted to flexural waves. Because of the high wavenumber of the coupled flexural waves it is assumed that the flexural wave energy can be dissipated before it is re-radiated into the scattered acoustic field. A reduction in target strength would then be achieved.

The addition of a keel to the cylindrical shell creates a new coupled system. The coupled system supports waves associated with both the keel and the shell, but their dispersion relations will be different from the dispersion relations of the uncoupled systems. The significance of the changes depends on the frequency of interest and the strength of the coupling. In this thesis, the changes in the dispersion relations of the shell waves due to coupling were assumed to be smaller than the resolution of the measurements. The data supports this assumption.

Waves in the coupled shell-keel system which are associated with the keel will be called 'keel waves' in this thesis. The keel wave associated with bending of the keel in its stiff direction was observed in the measured data. The axial velocity of this wave was found to be slower than the shear wavespeed of the shell, but higher than the wavespeeds of bending waves in the shell. A model was developed for the keel wave which showed that it was a coupled bending wave in the stiff direction of the keel. The neutral axis of the bending motion was shifted away from the neutral axis of the uncoupled keel. The other keel waves were not seen in the data.

A plastic PVC shell is used for the experimental study. The selection of this material was based in large part on cost. Fabrication of a steel cylinder without an axial seam was found to be prohibitively expensive. The plastic material did provide some advantages over a steel shell. Because of its relatively slow compressional and shear

wavespeeds, membrane waves could be observed at lower frequencies in the plastic shell than in a steel shell. Also because of its relatively high damping, the reverberant build-up of wave amplitudes was not observed so that reflections from the ends of the shell did not interfere with the measurements.

Compressional and flexural mode 0 waves were excited on the plastic shell using a circumferential source array. The source array was located in the middle of the shell, and a keel was attached to one end of the shell. Longitudinal and circumferential array measurements were taken on each end of the shell. Wavenumber-frequency transforms were used to separate the data by modal order and wave type.

The following sections of this thesis describe the research work that was completed. Chapter 2 presents a review of previous work that has been carried out at MIT and work that has been reported in the literature. Chapter 3 gives a general discussion of scattering and radiation mechanisms in cylindrical shells. Chapter 4 describes the design of an experiment to study wave coupling in a cylindrical structure with an axial keel. Chapter 5 describes the longitudinal array data collected on the two ends of the test shell. The response of a keel wave on the end of the shell with the keel is shown. Chapter 6 discusses the keel wave and coupling mechanisms due to the keel. Chapter 7 discusses the circumferential array data collected on the two ends of the test shell. The high modal orders of the coupled flexural waves are shown. Chapter 8 presents the conclusions of this research and suggests possible avenues for further research.

2. PREVIOUS WORK

2.1 Previous experimental work

Previous experimental work to study wave propagation in cylindrical structures has been carried out both in air and in water. Many of these studies have focused on measurements of the resonance frequencies of the shell. However, the complexity of the end conditions and their effect on the resonance frequencies make it difficult to use these data to determine the wave characteristics in the shell. In-water experiments have been carried out in specially designed water tanks and in lakes. These experiments can provide direct measurements of acoustic scattering and radiation. However, their cost is very high. In-air experiments are less expensive, but do not provide a direct measurement of scattering and radiation due to the large differences in the acoustic wavespeed and characteristic impedance of air and water.

2.1.1 1-D experiments

A series of papers have been published describing work carried out as part of the MIT/Industry Program in Structural Acoustics to study wave propagation in one-dimensional systems with attached absorbers [1-6]. A description of the use of tuned absorbers to reduce bending wave vibrations in a beam is also presented by Cremer [7] and Klyukin [8].

Corrado, Zavistoski, and Dyer [6] present a general discussion of elastic waves in one-dimensional structures with attached point-reacting structures. They refer to work reported in references 1-5. Results for simple beams and rods with distributed elastic absorbers are presented. All such systems are shown to exhibit stop-bands that form at or near resonances of the coupled point-reacting structure. Results for other wave types, such as torsional and helical waves in cylindrical shells are not presented, but the authors believe it likely similar results would be exhibited.

Corrado, Zavistoski, and Dyer [6] also consider coupling between two wave-bearing one-dimensional structures. The coupling between flexural waves in two beams coupled by a spring layer is considered in addition to the coupling between longitudinal waves in two rods. When both structures are wave-bearing, two distinct wavenumber branches associated with different wave types can be found. In general, these correspond to in-phase and out-of-phase solutions, where the two structures are moving in or out of phase. The behavior of the coupled wave-bearing systems is somewhat different than the behavior of a system with a layer of point-reacting dynamic absorbers. The existence of a stop band depends critically on the relative phase velocity in the two uncoupled layers. Only if the velocities are significantly different will a significant stop band occur.

The feasibility of using tuned absorbers to control membrane waves on ship hulls has been considered. However, the following limitations are observed. First, high damping and high rates of spatial attenuation are obtained only over a band of frequencies - the stop band. Second, the width of the stop band and the attenuation rate within the stop band depend on the mass ratio of the absorber mass to the hull mass. High mass ratios are generally required. If it were possible to use the mass of components and machinery within the ship as the tuned absorbers, these high mass ratios could be achieved.

The goal of the work presented in this thesis is to control membrane wave amplitudes over broad ranges of frequency without the addition of large amounts of mass. Based on the work described above, tuned absorbers will not meet these requirements.

2.1.2 Underwater experiments

Corrado [9] has studied data from measurements carried out by NRL in the Building 71 scattering measurement tank. The goal of the study was to evaluate the influence of membrane waves, resiliently mounted internal structures, and typical structural discontinuities on the scattering properties of cylindrical shells. The structural discontinuities include ring stiffeners, endcaps, and resiliently mounted internal components. The effect of a circumferential discontinuity, such as a keel, was not studied.

The shells used in the study were designed by Conti and Dyer [10] to have properties that are representative of full-scale ship structures. The shell thickness to radius ratio is 0.0096, the shell length to diameter ratio is 7.75, the compressional plate wavespeed is 5270 m/s, and the shear wave speed is 3100 m/s. Measurements were taken over frequencies $2 < ka < 12$, where k is the acoustic wavenumber in water and a is the shell radius. This frequency range corresponds to approximately ½ to 3 times the ring frequency of the shell.

The influence of membrane shear and compressional waves was seen in the scattered pressure field for angles of incidence within +/- 30 degrees of beam aspect (normal to the axis of the cylinder). Within this range of angles, the trace wavenumber of the incident acoustic wave along the axis of the cylinder can match the axial wavenumber of a membrane wave. The excitation of the membrane wave and subsequent re-radiation by this wave was found to be the dominant source of back-scattered energy from the shell for this range of angles.

2.1.3 Steel cylinder experiments in air

Bondaryk and others conducted experiments at MIT on a steel test shell in air. The steel shell was 12 inches in diameter and 0.1 inches thick, giving it a thickness to radius ratio of 1.7%. The steel shell was 17 feet long with conical endcaps welded onto each end. The shell was constructed with a welded axial cusp seam running down the length. Unlike earlier underwater measurements using shells designed by Conti and Dyer, the welds were not ground smooth to eliminate the effects of surface discontinuities. Data measured on the steel shell with mode 0 input showed response in compressional mode 0 and all flexural modes [11].

Possible explanations for the high response of the flexural modes include 1) errors in the excitation so that higher order modes were excited, 2) mode coupling at the endcaps, and 3) mode coupling at the welded axial seam. Measurements made by the author (later repeated and reported by Bondaryk [11]) on a plastic shell suggest that there were no errors in the excitation. Thus, the expected explanation is mode coupling at the shell discontinuities. Because the steel shell has very low damping, even weak coupling could result in significant transfer of energy. The energy ratio between the coupled

higher order flexural waves and the mode 0 compressional wave can be expected to follow the ratio of an appropriately defined coupling to damping factor. Equal wave energy is expected when this ratio is large [12].

2.1.4 Plastic cylinder experiments

Work performed by Lin [13] at MIT (during the course of research for this thesis) focussed on determining the pressure exerted by piezoelectric rings embedded in a cylindrical shell. A mathematical model was developed and confirmed by comparing predictions with data obtained on plastic PVC and aluminum plates. This model was then used to predict both the near-field and far-field vibration response of a steel and PVC cylindrical shell. Predictions were in good agreement with measured data thereby validating the calculation of the pressure exerted by the piezoelectric rings.

2.2 Previous analytical work

Ricks [14] developed a Direct Global Matrix (DGM) numerical formulation to model layered cylindrical shells. This formulation can be used to model any combination of solid, fluid, and vacuum layers. The excitations used in the formulation include time-harmonic ring forces for any circumferential order. Thus, the model can be used to study the propagation of membrane and bending waves in layered shells. Shells with visco-elastic constrained damping layers can be studied.

The modeling techniques developed by Ricks could extend the usefulness of the research presented in this thesis. The plastic shell used for the experimental work of this thesis had fairly high damping. Thus, it was not necessary to add a damping treatment to control the response of the coupled membrane and flexural waves. Also, since measurements were carried out in air, it was not necessary to include fluid loaded effects. Use of a keel to provide wave coupling in a steel shell in water will require techniques to dissipate the energy transmitted from the membrane waves to the flexural waves. The DGM formulation of Ricks could be used to develop visco-elastic damping layers to dissipate the flexural wave energy.

In a series of papers, Guo [15-19] presents numerical studies of a number of cylindrical shell configurations. In each case he shows that structures internal to the shell create discontinuities that scatter non-radiating waves into radiating waves. This scattering mechanism has a dominant effect on the sound scattering of incident acoustic waves on the shell.

In ref. [19], Guo presents a numerical analysis of acoustic scattering from a cylindrical shell with an elastic plate attached along the shell's axial direction. This study is relevant to the experimental study presented in this thesis. The importance of the plate as a circumferential discontinuity is shown by the numerical results. Flexural waves, which contribute little to the scattered field of the empty shell, are strongly present in the scattered field when the elastic plate is added. Guo uses a damping loss factor of 0.01, but states that a more realistic factor for underwater vehicles of 0.1 is expected to suppress the flexural wave signature in the scattered field. Although in-plane motion of the plate is included in the analysis, the coupling of the membrane shell waves with the plate in-plane waves is not discussed by Guo. His numerical results focus on the acoustic field, and do not address the introduction of a "keel" wave as seen in the measured data collected for the work in this thesis.

Hayner [20] has used a state-vector formulation to develop a Wave-based Finite Element Method (WFEM) for cylindrical shells. Two numerical formulations are presented: one for an axial wave formulation and one for a circumferential wave formulation. Both formulations are based on the Herrmann-Mirsky theory for thick 2D shells. Three different numerical models are developed using these formulations. The first is used to analyze a finite length cylindrical shell with one or more axial discontinuities, such as a ring frame or bulkhead. The second is used to analyze and infinitely long cylindrical shell with one or more circumferential discontinuities, such as a deck or keel. The third is used to analyze the through-thickness discontinuities introduced by shell layering.

The models developed by Hayner show promise for developing a numerical model of the cylindrical shell studied in this thesis. The WFEM is suitable to analyze either a shell with a complete homogeneous cross-section and a finite axial extent or a shell with a partial cross-section and an infinite axial length. Thus, further development would be

needed to accurately model a shell with a finite length keel. Further development would also be needed to model the wave coupling between an axial wave and higher-order circumferential waves.

3. SCATTERING AND RADIATION MECHANISMS ON CYLINDRICAL SHELLS

Scattering occurs when acoustic waves impinge on an object that has a different impedance than the acoustic media. The change in the incident acoustic field is represented by the scattered field, which can be described by an acoustic disturbance emanating from the scattering object. When pulses are used for the incident acoustic field, the scattered field takes the form of an echo. The time history of the echo contains information about the object that can be used not only to determine the range and direction of the object but to determine additional characteristics about the object that allow it to be identified. Echo ranging is used by bats in air and by dolphins in water to detect, locate, and identify objects. It is also commonly used in water by sonar systems to detect, locate, and identify submarines, ships, and fish. Echo ranging also forms the basis of ultrasonic devices that allow babies to be seen before they are born or to identify cracks and other flaws in elastic solids.

Scattering in air is easily understood. In air, the impedance of the scattering object is typically much larger than that of the air so that the object can be modeled as rigid. Scattering is then determined by the shape and orientation of the object relative to the incident acoustic field. In this case the scattering is often called geometric scattering.

In water, scattering is determined by the dynamic response of the object as well as its geometry. Because of the higher impedance of the water, scattering objects cannot be modeled as rigid surfaces. In this case the excitation, response, and radiation by vibration waves in the object has a major effect on the scattered field. For example, membrane shear waves in cylindrical shells have been found to have a major effect on the scattering by cylindrical shells representative of ship hulls in water.

An illustration of the wave scattering process is shown in Figure 3-1 taken from Corrado [9]. Scattering first occurs when the wave front reaches the front termination of the shell. A geometric scattered field is generated that depends on the impedance and shape of the front structure. The incident wave front continues to travel along the shell and excites vibration waves in the shell that have axial wavenumbers

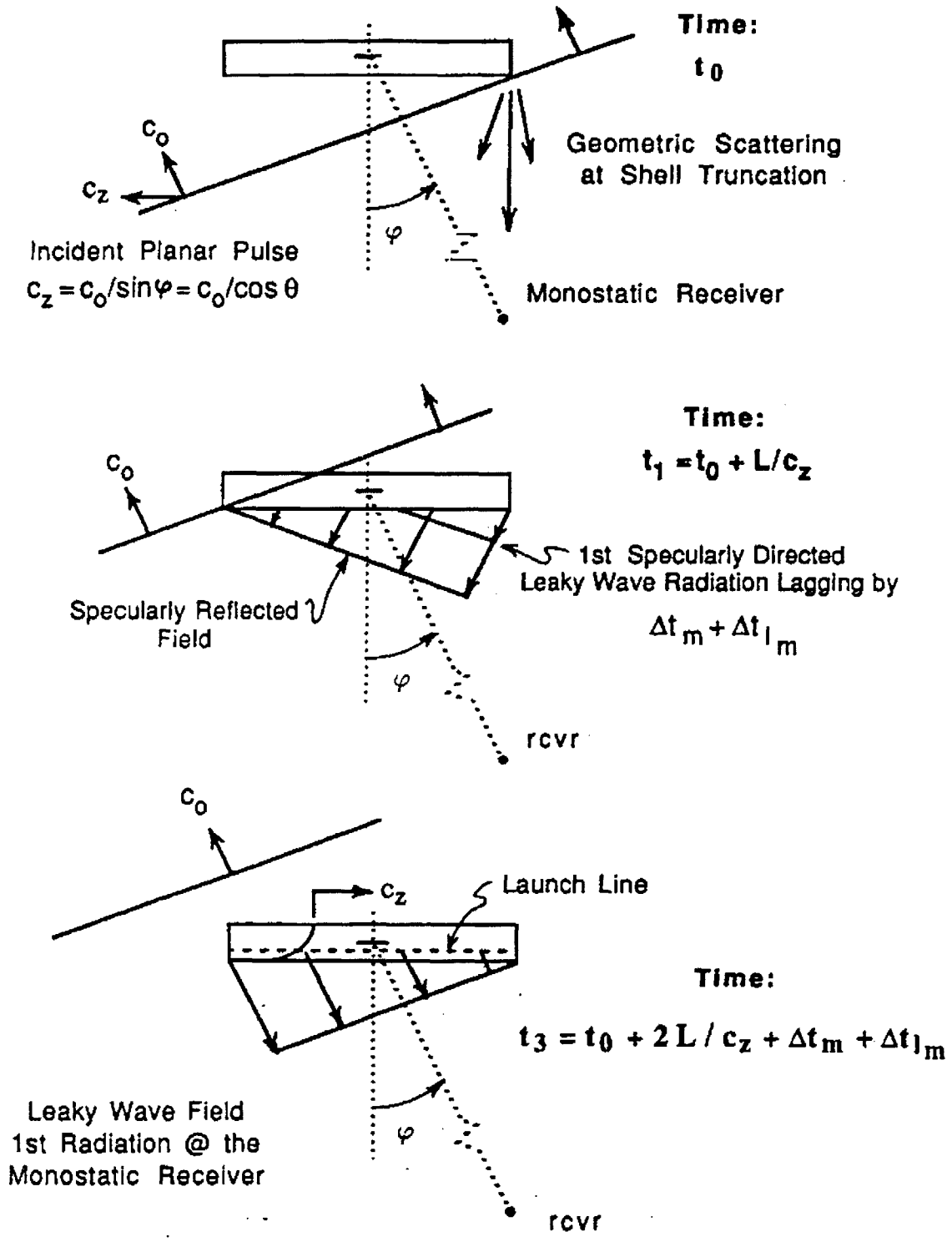

Figure 3-1: (Corrado Figure 1-5) Scattering processes for plane wave insonification of a finite shell with perfectly reflecting truncations and monostatic observation

matching the trace wavelength of the incident wave. Trace matching can occur for both membrane and flexural waves. However, the excitation of flexural waves is quite weak due to their short wavelength in the circumferential direction. Trace matching for membrane compressional or shear waves can also occur. Excitation of these membrane waves by the incident acoustic field will be quite strong due to the long wavelength in the circumferential direction. The radiation from the excited structural waves forms the specularly reflected field. When the incident wave front reaches the back termination of the shell, the structural waves are reflected from the termination and travel back toward the front of the shell. Radiation from these reflected waves travel back toward the monostatic receiver position and becomes the dominant source of back-scattered energy at this position.

3.1 Out-of-plane versus in-plane motion

Vibration waves in a flat structure can be divided into two groups – bending waves and in-plane waves. For structures with homogeneous cross-sections, the deformation of the bending waves is out-of plane normal to the surface of the plate. The deformation of the in-plane waves is primarily in the plane of the plate. For these in-plane waves a small out-of-plane deformation occurs due to Poisson coupling.

Structural radiation results only from the out-of-plane vibrations of the structure. In-plane vibrations result in very little radiation, since the acoustic medium is free to slide across the structure restrained only by the viscosity of the acoustic medium.

Bending waves are generally the most significant radiating waves due to their out-of-plane vibration. The radiation from in-plane extensional and shear waves is often ignored due to the small out-of-plane deformation. However, further consideration must be given since the phase speed of the bending and in-plane waves is significantly different. At frequencies below the critical frequency, the bending wave speed is subsonic while the wave speeds of in-plane extensional and shear waves are typically supersonic. Thus, the in-plane waves may radiate more than the bending waves, even though the out-of-plane deformation of these waves is significantly less than that of the bending waves.

In curved structures, the in-plane and bending deformations are coupled. For thin-walled structures, however, the waves can be still be divided into bending and in-plane extensional and shear waves. For a cylindrical shell, bending waves have deformations that are primarily out-of-plane, i.e. radial, with small in-plane axial and tangential deformations. In-plane, or membrane, waves have deformations that are primarily in-plane, with a small out-of-plane component. For the steel cylindrical shells typically used to model ships, the bending waves are generally subsonic in water, although the curvature may increase the wave speeds for some bending waves so that they are supersonic. The in-plane membrane waves in these structures are generally supersonic in water.

The increased out-of-plane deformation of the in-plane waves in the cylindrical shell result in greater radiation than would occur for the equivalent flat structure. Thus, the membrane waves become the most significant wave type for radiation and scattering of acoustic energy.

3.2 Subsonic versus supersonic waves

The radiation from structural vibration waves is strongly dependent on the phase speed of the wave. Strong radiation occurs when the phase speed of the wave exceeds the acoustic speed of sound in the surrounding media. Waves satisfying this condition on wavespeed are frequently called supersonic, while waves with phase velocities less the acoustic speed of sound are called subsonic. Supersonic waves are also called acoustically-fast waves, while subsonic waves are called acoustically-slow.

Subsonic waves radiate significantly less energy than supersonic waves. For example, a subsonic wave on a flat, infinite plate does not radiate any energy to the acoustic media, although a non-propagating pressure fluctuation may extend some distance away from the structure into the acoustic media.

The power radiated per unit area from an infinite plate can be expressed in terms of the velocity normal to the plane of the plate and the ratio of wavespeeds,

$$W_{rad} = \frac{\rho_a c_a}{\sqrt{1 - \frac{c_a}{c_b}}} \langle v^2 \rangle \qquad \text{for } c_a > c_b \quad \text{(subsonic)} \qquad \text{Eq. 3-1}$$

$$W_{rad} = 0 \qquad \text{for } c_a < c_b \quad \text{(supersonic)} \qquad \text{Eq. 3-2}$$

where w_{rad} is the radiated power, c_a is the speed of sound in the acoustic media, ρ_a is the density of the acoustic material, c_b is the phase speed of the structural wave, and v is the velocity amplitude of the wave. For a finite plate the singularity at the critical frequency ($c_a = c_b$) does not exist, but a peak in the radiated power occurs.

The phase speed for bending waves depends on frequency, increasing with the square-root of frequency. Since the bending wave speed increases with frequency while the acoustic speed of sound is constant, a frequency can be found at which the bending wave speed is equal to the speed of sound in the acoustic media. This frequency is called the critical or coincidence frequency. Above the critical frequency, the bending waves are supersonic and radiate a significant amount of energy. Below the critical frequency, the bending waves are subsonic and therefore radiate significantly less energy.

On a curved structure, such as a cylindrical shell, subsonic waves radiate a small amount of energy due to the curvature of the wave even though the phase speed of the wave is less than the speed of sound in the acoustic media. Although the radiation of the subsonic waves is significantly less than that from supersonic waves, it is not zero. The power radiated by waves on a cylindrical structure can be generally written in terms of the radiation impedance,

$$W_{rad} = \mathrm{Re}\{z_{rad}\} < v^2 > \qquad \text{Eq. 3-3}$$

where $\mathrm{Re}\{z_{rad}\}$ is the real part of the radiation impedance. The real and imaginary parts of the radiation impedance have been determined by Junger for the general cylindrical shell. Although curvature has some influence on the radiation impedance, its dependence on the ratio of acoustic wave speed to structural wave speed continues to be strong with subsonic waves radiating significantly less than supersonic waves.

Curvature of the structure may also cause the phase speed of the vibration waves to increase due to the stiffening effect of the curvature. The effect is most pronounced at and near the ring frequency.

Subsonic waves on a finite structure radiate a small amount of energy due to edge effects at the boundaries of the structure. The amount of radiation depends on the boundary conditions, with the greatest amount of radiation resulting from blocked (clamped) boundaries and the least amount of radiation resulting from free boundaries. Radiation from simply-supported boundaries fall between these two extremes.

Radiation from subsonic waves also occurs due to scattering of the waves by discontinuities within the structure. Typical discontinuities include stiffeners, ring frames, and bulkheads. Components mounted on the structure also represent discontinuities that cause the subsonic waves to radiate.

The power radiated by waves on a finite structure with edge conditions and discontinuities can be generally written in terms of a radiation efficiency,

$$w_{rad} = \rho_a c_a \sigma_{rad} \langle v^2 \rangle \qquad \text{Eq. 3-4}$$

where σ_{rad} is the radiation efficiency. Radiation efficiencies are typically less than one, although values greater than one are possible.

Structural discontinuities and edge effects can also result in coupling of the subsonic and supersonic waves. A fraction of the energy in a subsonic wave incident on a discontinuity may be reflected and/or transmitted into a supersonic wave, which radiates significant energy to the surrounding media. In this case, the structural discontinuity greatly increases the radiation by the subsonic wave. Reciprocally, energy in the supersonic wave may be reflected and/or transmitted into the subsonic wave. In this case the radiation from the supersonic wave is reduced, since the subsonic waves radiate significantly less energy. The net effect of adding a discontinuity that results in coupling between subsonic and super sonic waves is to increase the radiation by energy in the subsonic waves and decrease the radiation by energy in the supersonic waves.

3.3 Adding a discontinuity may increase radiation and target strength

It is not immediately clear that adding a keel is a good idea. Eliminating discontinuities is a traditionally successful strategy in the effort to reduce radiation and target strength. Machinery noise (point sources) excites the short wavelength flexural waves. A keel may serve to couple these flexural waves into radiating compressional waves.

The addition of a keel may also increase the acoustic scattering and target strength by coupling the subsonic flexural waves to the acoustic field. Although it may be possible to dampen the energy in these flexural waves, their response and re-radiation increases the scattered field.

The axial keel wave introduced by adding a keel to the shell may be supersonic and may create a strong scattered field at angles where axial trace matching occurs between the keel wave and the incident acoustic wave. The response and re-radiation by the keel wave may also increase the scattering and target strength.

3.4 Axial discontinuities increase radiation and target strength

The addition of ring stiffeners and other axial discontinuities provides added scattering mechanisms. In addition, the membrane waves excited by the incident acoustic field are partially reflected at each discontinuity. These reflected membrane waves radiate back toward the monostatic position providing increased target strength. The effect is illustrated in Figure 3-2, taken from Corrado [9].

Corrado's research shows that the addition of ring stiffeners has the detrimental effect of increasing target strength. Thus, although it may be argued that axial discontinuities provide mechanisms for converting the membrane wave energy into poorly radiating flexural wave energy, thereby reducing the back-scattered energy, these discontinuities also provide mechanisms for reflecting the membrane wave energy and increasing the back-scattered energy. The measured data presented by Corrado suggest that the detrimental effect is stronger, so that the target strength is increased by the axial discontinuities.

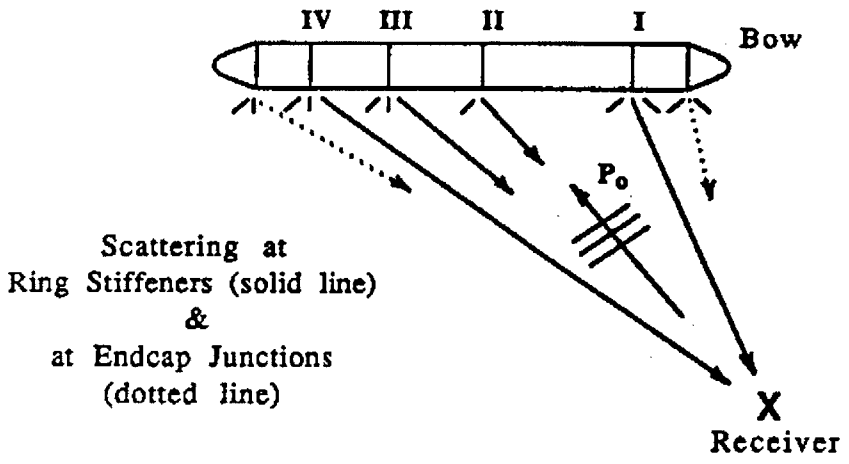

Figure 3-2: (Corrado figure 5.17) Illustration of propagation paths of the first incidence of scattering from the ring stiffeners and endcaps of the shell models

3.5 Reducing target strength and radiation by adding a keel

The addition of an axial keel, which is being studied in this thesis, is advantageous because it is a circumferential discontinuity rather than an axial discontinuity. Axial discontinuities have been shown to reflect membrane waves, reversing their axial propagation direction, and thus increasing the target strength. If it extends the entire length of the shell, the keel does not provide an axial discontinuity.

Furthermore, the keel provides a mechanism to convert energy from the membrane waves into poorly radiating, subsonic flexural waves. The membrane compressional and shear waves are supersonic. This condition can be written in terms of the wavenumbers as

$$k_x^2 + k_\theta^2 < k_a^2 \quad \text{for supersonic waves}$$

$$k_x^2 + k_\theta^2 > k_a^2 \quad \text{for subsonic waves}$$

where k_x is the axial wavenumber, k_θ is the circumferential wavenumber, and k_a is the acoustic wavenumber.

Membrane waves observed on cylindrical shells have low axial and circumferential wavenumbers and therefore are supersonic. The addition of a keel causes the membrane waves to be coupled to trace-matched flexural waves. Coupling occurs when the axial wavenumbers of the membrane wave and the coupled flexural wave match. However, the circumferential wavenumber of the coupled flexural waves will be large, so that the helical wavespeed is subsonic. These subsonic flexural waves are poor radiators. Thus, any transfer of energy from the supersonic membrane waves to the subsonic flexural waves should help to reduce scattering.

The conversion of energy from membrane waves into flexural waves would reduce the radiation by the membrane waves, particularly to the monostatic position. If the conversion mechanism could be made strong enough so that all membrane energy could be converted to flexural energy in the time it takes for the membrane wave to propagate from the front to back of the shell, the observed field at the monostatic position would be greatly reduced and would result only from the geometric scattering when the incident wave passes the front and back termination of the shell.

4. DESIGN OF EXPERIMENTS

4.1 Plastic test shell

The goal of this research was to investigate wave coupling on a cylindrical shell with a keel. Before studying this complex structure, experiments were performed on a plain cylindrical shell in order to verify the test setup and data processing techniques. A testing system was needed which could excite and measure various waves on a cylindrical shell. The test system previously used at MIT for steel shell measurements was used as a starting point. In order to determine whether the test system was functioning as desired, a relatively simple, well-understood test shell was needed. The physics of ideal circular cylindrical shells are well-known, making these 'plain' shells a good proving ground for the test system. The measurements on the plain shell would also serve as comparison data for planned keel studies.

In order to ease the comparison of measured data with theoretical predictions, a test shell was chosen to best meet the following criteria:

1) To best model an infinite shell, the test shell should have minimal reflections at the ends;

2) To best model an ideal homogeneous circular cylindrical shell, the test shell should be seamless, without end structures such as endcaps, and stiff enough to maintain its circular shape and a straight longitudinal axis when suspended at a limited number of points in the lab.

Additional practical criteria for the test shell were:

1) To maximize the number of measurable modes, the diameter should be as large as possible;

2) To avoid the complications of thick shells, the thickness to radius ratio should be as small as possible;

3) To be maneuverable, the shell should fit into the existing laboratory and should be lightweight enough to be lifted and positioned without a crane;

4) To be affordable, the shell should be available off-the-shelf.

With the goal of eliminating any coupling due to an axial seam, a seamless shell was desired. Previous studies were carried out on a steel test shell, but a steel seamless shell with a large diameter and small thickness to radius ratio could not be found off-the-shelf. Fabrication of a seamless steel shell was investigated by Joe Bondaryk and found to be prohibitively expensive.

The use of a plastic shell was suggested and investigated by the author. A plastic, seamless test shell was found which met the above criteria and had additional benefits. A large diameter, seamless, thin PVC Type I (poly-vinyl-chloride) duct pipe was purchased off-the-shelf. Since plastic is relatively lightweight, a large diameter test shell could be handled easily by 2 people in the existing laboratory. The plastic shell was 16 inches in diameter with a nominal thickness of 3/16 inches, giving it a thickness to radius ratio of 2.3%. The wavespeed of quasi-longitudinal (or compressional) waves, $c_{LII} = \sqrt{(E/\rho)}$, is 1580 meters per second for the PVC cylinder, around 1/3 that of steel. The lower compressional wavespeed combined with the larger diameter gave a lower ring frequency and allowed measurement of many more modes. In theory, up to 5 compressional, 10 shear and 30 flexural modes could be measured on the plastic shell below 8 kHz. In addition, the plastic shell had much higher damping than the steel shell. The plastic shell was 20 feet long, and because of the high damping, wave amplitudes decayed significantly before hitting the ends of the shell and returning. The total number of measurable reflections (round trips) was very small. This had the effect of reducing any wave or mode coupling at the ends of the shell. It also made it possible to measure direct and reflected wave amplitudes.

4.2 Discussion of coupling vs. damping

It is important to understand the relationship between coupling and damping effects. High damping can mean that weak coupling factors do not have enough time to make a

measurable change in wave energies. Conversely, low damping can give even weak coupling factors ample time to equalize the coupled wave energies.

The steel shell used in previous research at MIT had very low damping, so that waves traveled back and forth along the shell many times before they died out. Even very small coupling between modes could have resulted in significant transfer of energy due to the high number of reflections and long travel path. Coupling effects at the endcaps or along the axial seam could have built up after many round trips of the modal waves, so that at steady state, the measured modal energy was equal in all the coupled modes. The presence of higher order modes in the steel shell response might be explained by this phenomenon.

On the plastic shell, the damping is relatively high. Coupling mechanisms have to be relatively strong to result in transfer of significant (i.e. measurable) amounts of energy between the coupled waves. It will be shown in this thesis that a keel with reasonable dimensions can provide measurable coupling between mode 0 compressional waves and trace-matched higher order flexural waves on a plastic shell.

4.3 Keel

A keel was attached to the outside of the plastic shell along an axial line. The keel was attached to the outside so that the bond could be carefully inspected. The keel was the same material (PVC) and the same thickness (0.2 inches) as the cylinder. It was 5 feet long (152 centimeters), and it was attached at one end of the cylinder as shown in Figure 4-1. The keel was set with epoxy into a ¼" groove cut into the outer wall of the cylinder using a router. The properties of the epoxy 'joint' between the cylinder and the keel were not studied in this thesis.

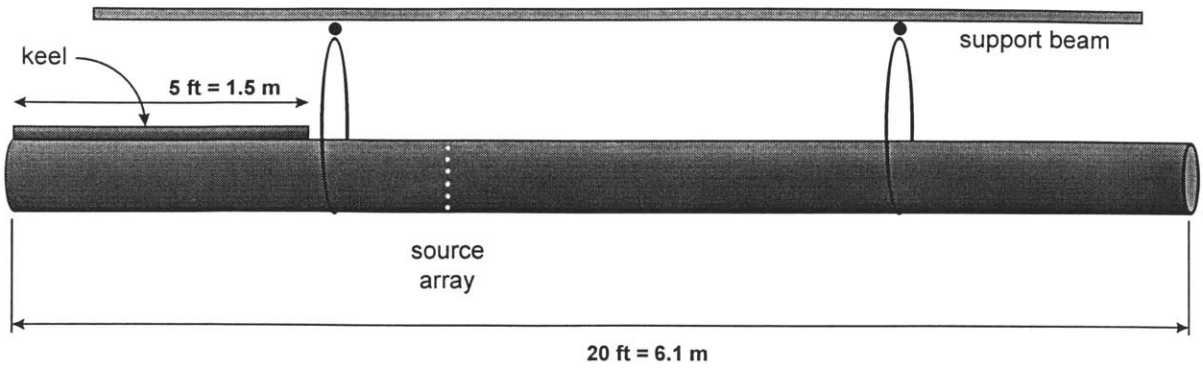

Figure 4-1: Position of keel

4.4 Source array

The input system was designed to generate a ring of shaped motion around the circumference of the cylinder. An array of twelve piezo-ceramic sources was used to enable shaping of single modes 0 - 6. A commercial frequency analyzer was used to generate the source signal, a broadband white noise signal. The source signal was passed through a series of filters and amplifiers to the piezo-ceramic source array. A transformer was used to provide a high voltage, low current input to the piezo-ceramic sources. Shaping the input signal to set up $n > 0$ modes required twelve individual power amplifiers and transformers. Concerns about phase accuracy and difficulty in achieving high enough excitation voltage made it necessary to consider only excitation of the $n = 0$ mode in this thesis.

4.4.1 Aliasing of input mode

The input was generated by an array of twelve piezo-ceramic sources, spaced evenly around the circumference of the shell. According to Nyquist theory on aliasing, at least two sources are required per wavelength to set up a given modal shape. Thus, the twelve sources could generate mode shapes 0 - 6, with aliasing into higher order modes. Mode 0 was excited by sending an identical signal to all twelve sources. This input theoretically excites mode 0 waves, in which all points around the circumference move in unison, but it also excites modes 12, 24, 36, etc. The excitation of mode 12 is shown in Figure 4-2.

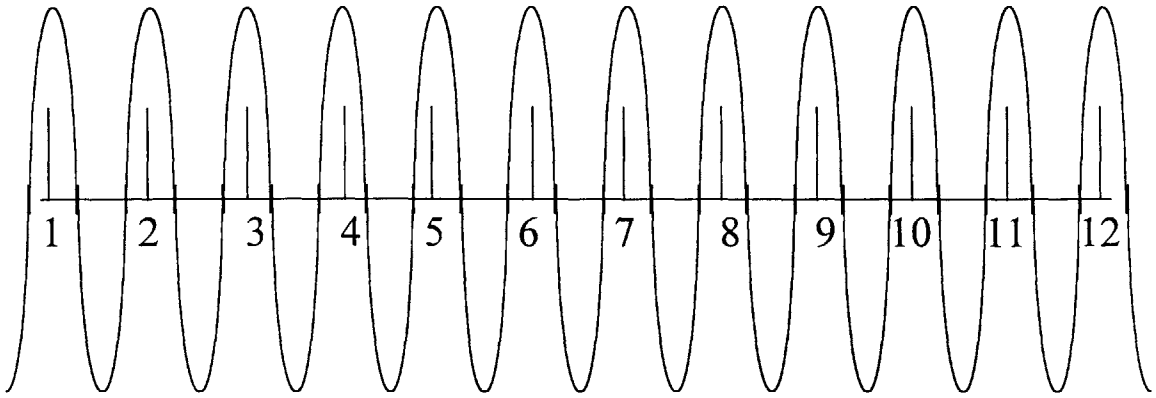

Figure 4-2: Mode 0 input, equal at all sources, excites modes 0 and 12

Input shaped to excite modes 1 through 6 also aliases into higher order modes. This effect was seen in the accelerometer data collected at the beginning of this research before the laser system was set up.

Although mode 0 waves can be excited with fewer transducers, a source array with twelve individual transducers was chosen in order to facilitate separation of waves in the wavenumber-frequency plots. The dispersion relations of flexural waves with modal order 0 to 10 are very closely spaced in the wavenumber-frequency domain. It is difficult to distinguish them from one another. A twelve element source array allowed separate measurement of both the fundamental excitation mode 0 and the higher order mode 12 excited through aliasing.

4.4.2 Piezo-ceramic transducers

The sources were piezo-ceramic hollow cylinders, embedded orthogonally into the wall of the test shell so that their radial expansion imparted a force in the 'plane' of the shell. (Figure 4-3) They were made of piezo-ceramic material 5700 (lead zirconate titanate) from Channel Industries (Navy Type IV). They had an outer diameter of 0.313 inches, were 0.027 inches thick and 0.312 inches long. The radial and longitudinal natural frequencies of the sources were above 126 kHz, well out of the measured frequency range. When a voltage was applied across the sources, they responded by expanding

radially and longitudinally with respect to the source axis. The pressure exerted on the shell by each transducer was calculated by Lin. [13]

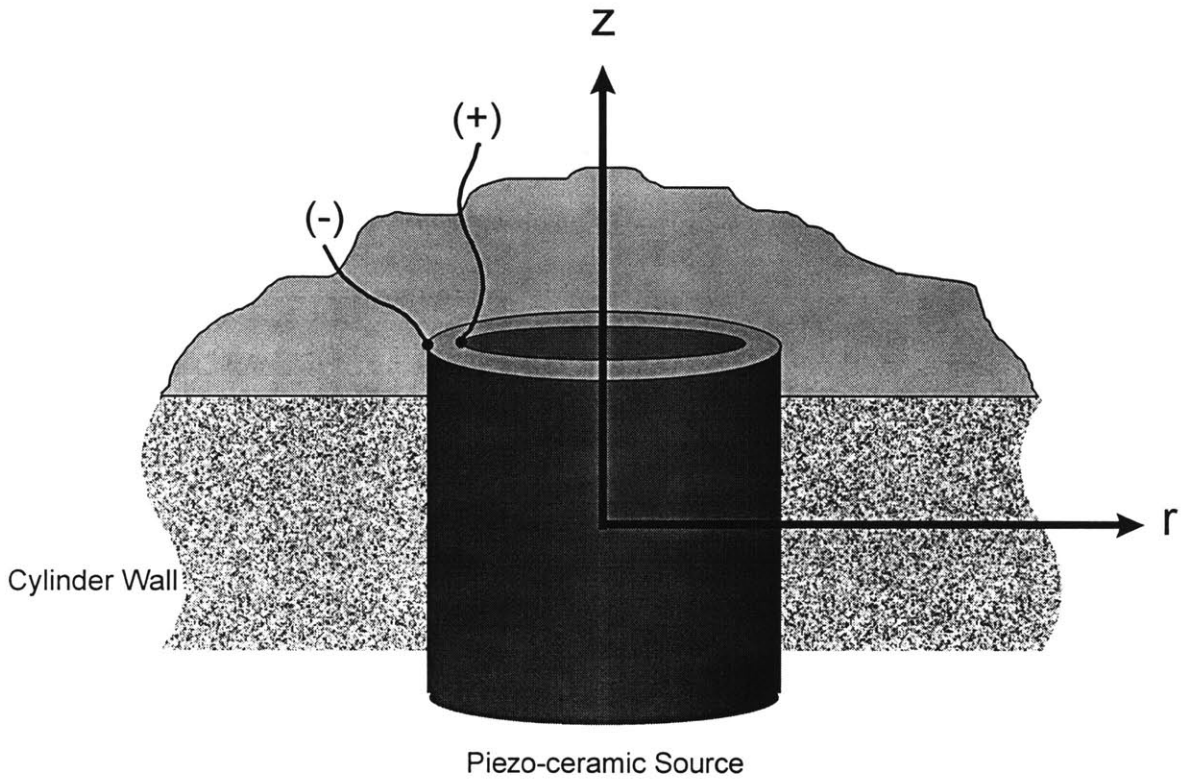

Figure 4-3: Source installation

Because of the high damping in the plastic shell, and because of the desired distance between the source array and the measurement locations, the source signal needed amplification. The approximate maximum voltage that could be applied to the piezo-ceramic sources without failure was calculated. In order to prevent failure due to overload, the total power into the sources was limited. The frequency range of the input was bandwidth-limited using filters so that the voltage levels could be boosted without increasing the power too much. In this way, the signal-to-noise ratio was increased enough to separate the data from the noise.

4.5 Receiver arrays

The vibratory response of the shell was measured at an array of locations. The measured time series was Fourier transformed to get a frequency spectrum for each point in the array. The individual frequency spectra show peaks at the excited frequencies, but do not differentiate between the different wave types or circumferential mode numbers. Measuring at an array of locations enables spatial Fourier transformation across the array, providing wavenumber spectra for each frequency. The combination of frequency and wavenumber information allows differentiation among various wave types and between circumferential mode numbers.

The receiver arrays were designed with the same principles used when collecting time data for future Fourier transforms into the frequency domain. Spatial variable, x, replaces time variable, t, and spatial frequency or wavenumber, k, replaces temporal frequency, ω.

Temporal transform		Spatial transform	
Time	t	distance	x
Frequency	ω	wavenumber	k
Time sample spacing	Δt	array spacing	Δx
Sampling time	T	array length	L
Frequency spacing	$\Delta\omega = 2\pi/T$	wavenumber spacing	$\Delta k = 2\pi/L$
Sampling frequency	$\omega_s = 2\pi/\Delta t$	sampling wavenumber	$k_s = 2\pi/\Delta x$
Nyquist frequency	$\omega_s/2 = \pi/\Delta t$	Nyquist wavenumber	$k_s/2 = \pi/\Delta x$

4.5.1 Array spacing

The longitudinal array spacing was determined based on the smallest longitudinal wavelength desired to be measured. According to Nyquist theory, at least two points per wavelength are required. Since wavelength and wavenumber are inversely proportional, the wave with the smallest wavelength has the largest wavenumber. The theoretical dispersion curves plotted in Figure A-1 indicate that the largest longitudinal wavenumber to be measured is that of the mode 0 flexural wave at 8 kHz. (See Appendix A for theory.) Figure 4-4 shows the theoretical dispersion curves for mode 0 flexural, compressional and shear modes. The figure shows that the normalized longitudinal wavenumber of the mode 0 flexural wave, $k_x a_{flex0}$, is 30 @ 8 kHz. The corresponding longitudinal wavelength can be calculated to be 4.3 centimeters.

$\lambda_{x,flex0}$ @ 8 kHz = $2 \pi a / k_x a_{flex0}$ = 1.7 in or 4.3 cm

where radius, a = 8 inches.

This is the smallest longitudinal wavelength to be measured, and the longitudinal measurement array spacing was chosen to avoid aliasing of these small wavelengths. In accordance with the Nyquist criterion, spacing should be closer than 2.15 centimeters. A longitudinal array spacing of 1 centimeter was chosen to provide ample oversampling at 8 kHz. Oversampling provides better rejection of noise and insures that higher wavenumbers will not be aliased into the region of interest. The wavelengths for mode 0 flexural, compressional and shear waves are shown in Figure 4-5. Wavelengths at 8 kHz are listed below.

λ_{flex} @ 8 kHz = $2 \pi a / 30$ = 1.7 in or 4.3 cm

λ_{shear} @ 8 kHz = $2 \pi a / 10$ = 5.0 in or 12 cm

λ_{comp} @ 8 kHz = $2 \pi a / 5.6$ = 9.0 in or 22 cm

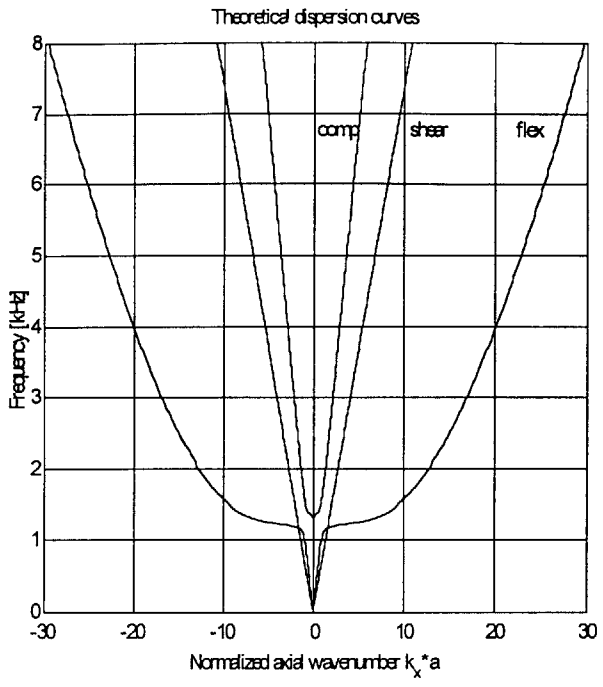

Figure 4-4: Theoretical dispersion curves for mode 0 waves

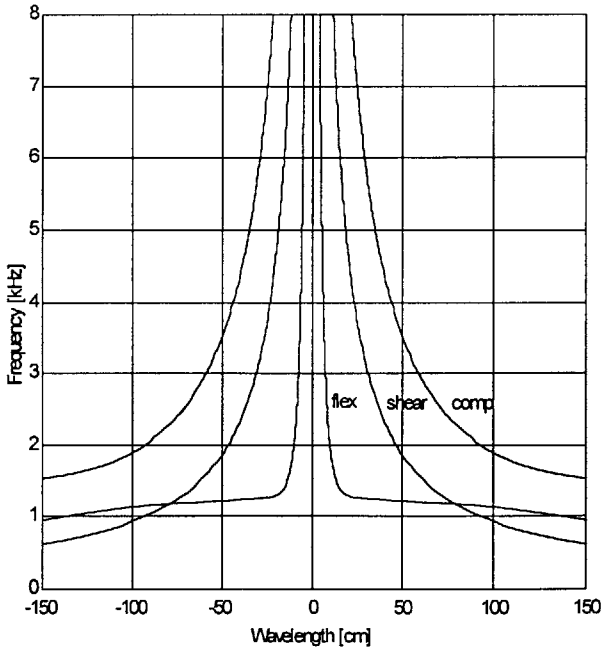

Figure 4-5: Theoretical wavelengths for mode 0 waves

The circumferential array spacing was also chosen based on the Nyquist criterion for avoiding aliasing. According to plain cylinder theory, the highest circumferential mode with a cut-on frequency below 8 kHz is flexural mode 30. (Figure A-1) In order to measure circumferential mode 30, Nyquist theory suggests sampling at least 60 points around the circumference. A circumferential array spacing of 1 cm corresponds to 125 points around the circumference, which amply oversamples the circumferential modes. In addition, using the same spacing for both the longitudinal and circumferential arrays facilitated processing and interpretation of the data.

4.5.2 Array length

The length of the longitudinal array was chosen to allow adequate resolution of wavenumbers. The longitudinal laser array was 120 points, or 119 cm long, giving a normalized longitudinal wavenumber resolution, $\Delta k_x a$, of $2\pi a/L$ or 1.07. The circumferential array extended all the way around the cylinder. It was 125 points, or 124 cm long, giving a normalized circumferential wavenumber resolution of $\Delta k_\theta a = 1.03$.

4.5.3 Longitudinal array determines wave type via dispersion relation

When the equations of motion for an infinite cylindrical shell are written, they are separated into modes in the circumferential direction and waves in the longitudinal direction. Thus we can talk about mode 0 waves travelling longitudinally down the shell. The separated equations of motion can be written in the form of longitudinal dispersion relations, relating the frequency to the axial (longitudinal) wavenumber for each modal order and for each wave type. The longitudinal wavenumber can be measured experimentally using a longitudinal array. Data from the longitudinal array can be spatially transformed to obtain a measurement of the dispersion curves. Information on the modal order of the waves is not contained in the longitudinal data, although some knowledge can be gained by comparison with theory.

4.5.4 Circumferential array determines modal order

Spatial transforms of the data from a circumferential array give information on the circumferential wavenumber of the measured waves. The circumferential wavenumber

corresponds directly to the circumferential modal order of the waves. Circumferential modes of a circular cylinder can be expressed in terms of sin and cosine mode shapes, $\sin(n\theta)$ and $\cos(n\theta)$, where θ is the circumferential angle from 0 - 2π radians and n is the mode number. The mode shapes can also be written in terms of the circumferential distance, $y = a*\theta$, and the circumferential wavenumber, k_θ, as $\sin(k_\theta a*\theta)$ and $\cos(k_\theta a*\theta)$. It follows that the mode number and circumferential wavenumber are related, $n = k_\theta*a$.

4.6 Data processing

4.6.1 Spatial variations of the transfer functions

In this research, transfer functions were collected at an array of locations on the shell. For example, Figure 4-6 shows the magnitude of the transfer function versus position for the 2 kHz and 4 kHz frequency lines. Based on theoretical studies of the shell we expect to see waves corresponding to different circumferential mode numbers propagating axially along the shell. For each mode number, n, five waves types are possible corresponding to the five degrees of freedom: translation in the radial, circumferential, and axial direction and rotation of the shell cross-section about an axial line and about a circumferential line. The latter two degrees of freedom are added when a thick shell theory is used to account for the effects of transverse shear deformations and rotary inertia. The curvature of the shell and the Poisson effect cause the motion in the different directions to be coupled for each mode. However, we can continue to refer to modes as flexural, compressional, and shear based on the largest component of the modal displacement, i.e compressional modes have the greatest amplitude in the axial direction, shear modes have the greatest amplitude in the circumferential direction, and flexural modes have the greatest amplitude in the radial direction. However, care must be used when following the dispersion curve for a particular wave type, since the wave may change its character. For example, the n=0 flexural modes at high frequency become n=0 compressional modes at low frequencies below the ring frequency. Thus, the naming convention is somewhat arbitrary.

The uniform excitation of the twelve source transducers is expected to excite n=0, n=12, and higher multiples of 12. Based on theory, both n=0 compressional and flexural

modes should be observed over the frequency range of interest for this thesis. The n=12 flexural modes should also be observed. The shear modes are not excited and should not be observed. The n=12 and higher order compressional waves do not exist in the frequency range of these experiments. The n=24 flexural mode was expected in the data but was not seen.

Figure 4-6 shows the longitudinal array data for the plain end of the shell at 2 kHz and 4 kHz. The interference pattern in the data suggests multiple waves. At 2 kHz the interference pattern suggests two dominant waves. However, it is difficult to visually determine the wavenumbers of these waves. At 4 kHz the interference pattern is even more complicated, suggesting multiple waves. A Fourier transform with respect to the spatial variable (position) can be used to extract all of the wavenumbers present in the data.

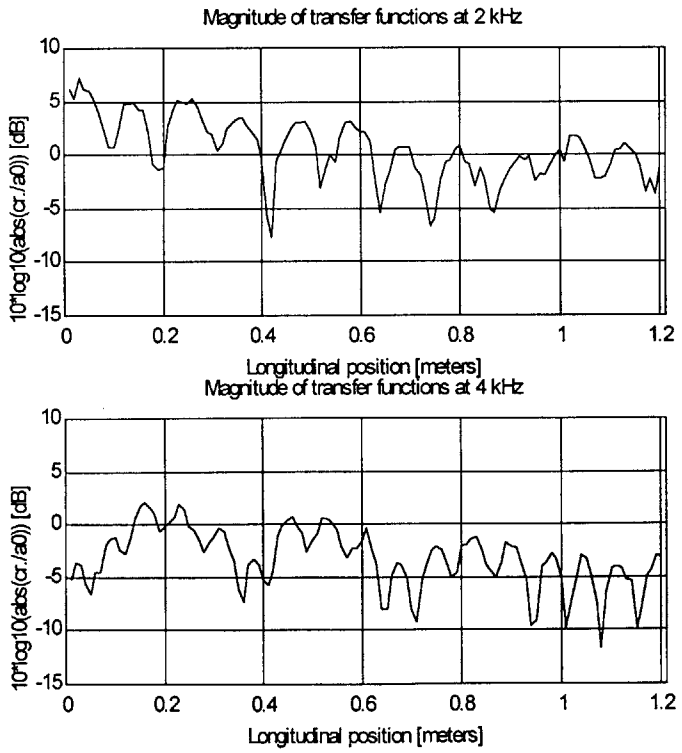

Figure 4-6: Longitudinal array data, plain end, at 2 kHz (top) and 4 kHz (bottom)

The raw data can be visualized in a three-dimensional plot showing the magnitude of the transfer function versus frequency and position. Figure 4-7 shows the unprocessed longitudinal array data collected on the plain end of the shell. A wave pattern can be seen in this figure, with generally longer wavelengths at lower frequencies and shorter wavelengths at higher frequencies. The wave pattern shows fluctuations in the magnitude of the transfer function, suggesting interference between two or more waves. The presence of more than one wavetype travelling at any given frequency makes the plot difficult to interpret without further processing.

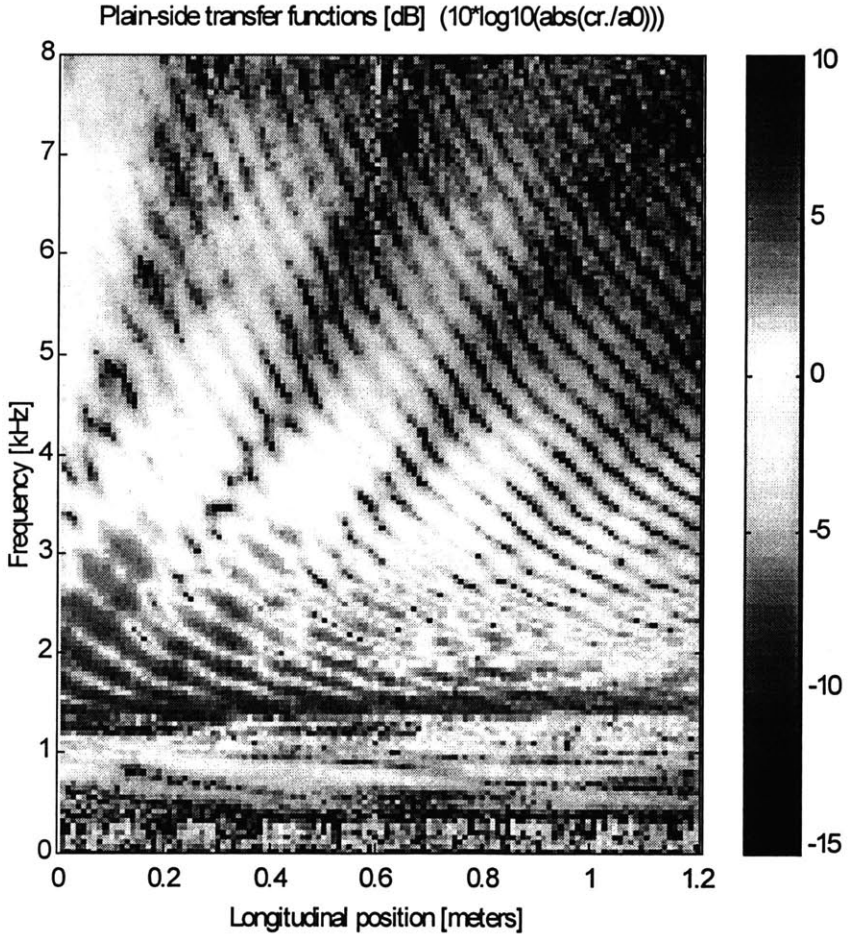

Figure 4-7: Longitudinal array data, plain end

4.6.2 Wavenumber-frequency transforms

Wavenumber-frequency transforms can be used to separate waves via their dispersion relations. Compressional waves and flexural waves may propagate at the same frequencies, but with different wavenumbers (or at the same wavenumber but different frequencies). A two-dimensional (time and space) array of measured wave velocity data can be transformed both temporally (for frequency) and spatially (for wavenumber), giving a three dimensional surface on which the wavenumbers associated with each frequency component are shown. The dispersion relations of the waves are thus clearly seen and easily separated.

A Fourier transform with respect to position can be used to determine the various wavenumbers present at each frequency based on the variations in the magnitude and phase of the transfer functions. Figure 4-8 shows the Fourier transform of the data in Figure 4-6. It shows that other wavelengths are also strongly present in the data. Three dominant peaks occur in the wavenumber spectrum which correspond to the three excited waves on the shell: mode 0 compressional, mode 0 flexural and mode 12 flexural.

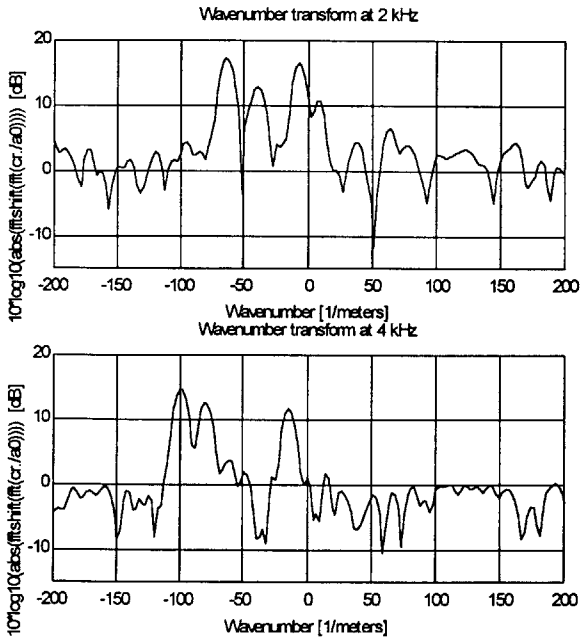

Figure 4-8: Wavenumber transform at 2 kHz (top) and 4 kHz (bottom)

Assembling the wavenumber transforms for each frequency into one three-dimensional matrix gives even more information. This matrix, called the frequency-wavenumber transform, shows the changing relationship between the frequency and wavenumber of each wave present in the data. In other words, the frequency-wavenumber transform makes visible the dispersion relations for each wave. Figure 4-9 shows the frequency-wavenumber transform of the data shown in Figure 4-7. Four distinct curves can be easily distinguished, three with negative wavenumber and one with positive wavenumber. Each of these curves represents the dispersion relation of a particular wave. Two of the curves are straight, indicating non-dispersive waves such as compressional or shear waves. The other two waves have curved dispersion relations, like those of flexural waves.

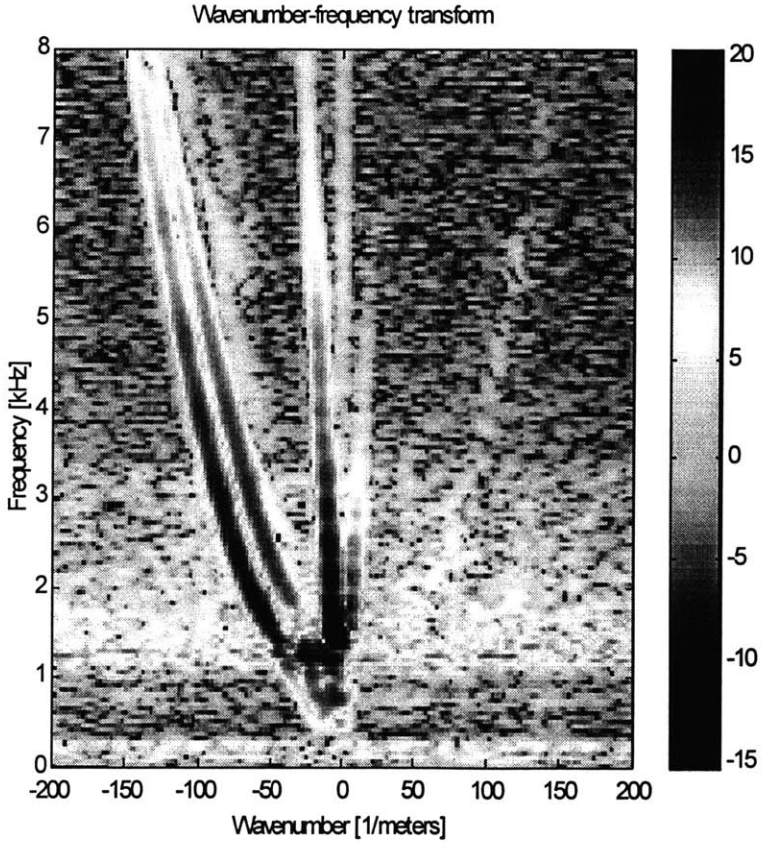

Figure 4-9: Frequency-wavenumber transform of the longitudinal array data collected on the plain end of the cylinder

4.7 Support of Shell

The shell was suspended by ropes at two locations along its length as shown in Figure 4-10. There were a few concerns with this method of suspension. The first concern was that the ropes would act as a discontinuity and reflect waves. In order to check this hypothesis, the radial velocity was measured at a single location on the shell while the ropes were moved to various positions. Data was collected with the ropes 1) between the source array and the measurement location, and 2) on the other end of the source array, as shown in Figure 4-11. There was no noticeable change in the data due to the position of the ropes.

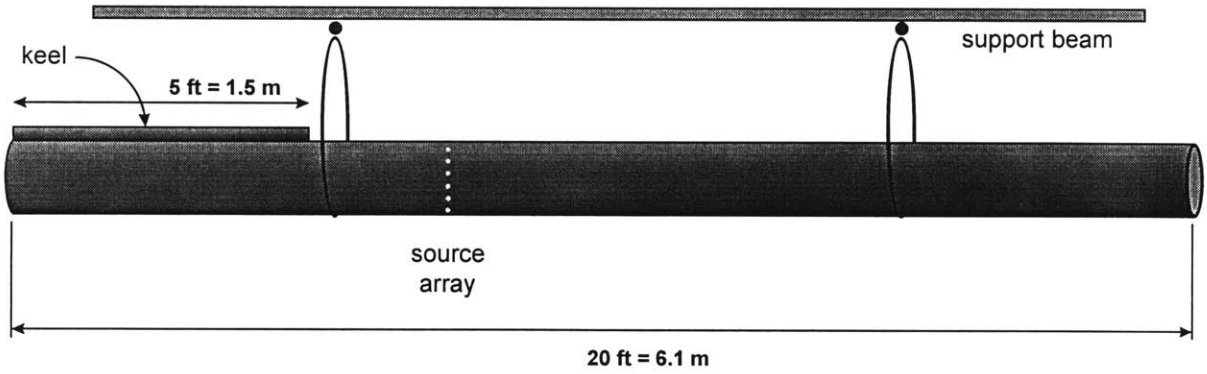

Figure 4-10: Support of Shell

The second concern was that rotation of the shell would change the shell and/or support system properties so that measurements would not be repeatable. To address this concern, laser measurements were taken at the same location on the shell before and after a large rotation. The 'before' and 'after' measurements were identical within the accuracy of this type of measurement, as shown in Figure 4-12.

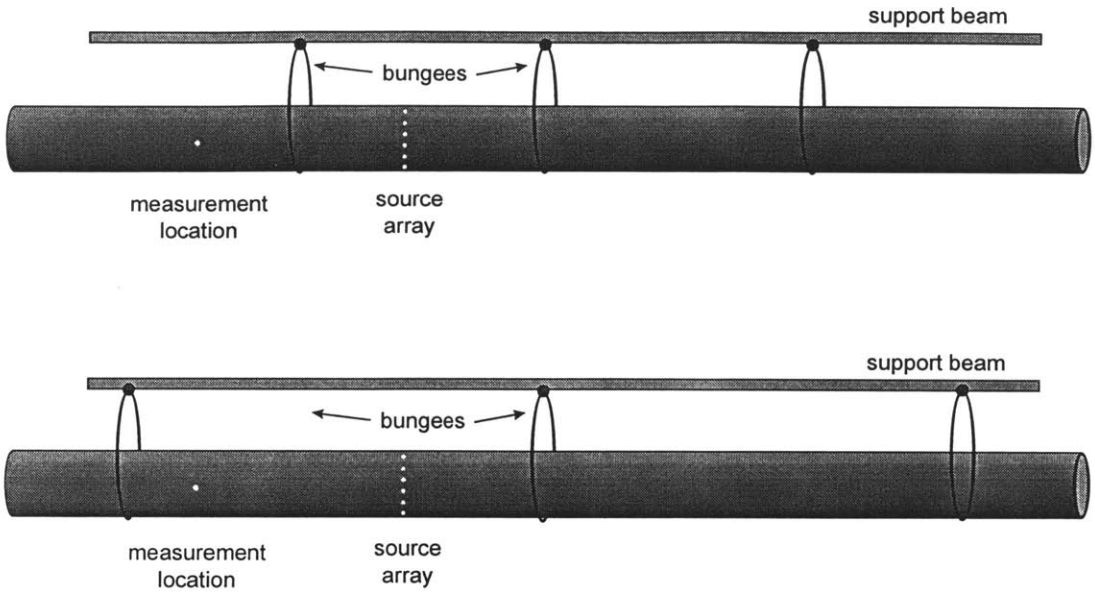

Figure 4-11: Location of bungee cords in various tests

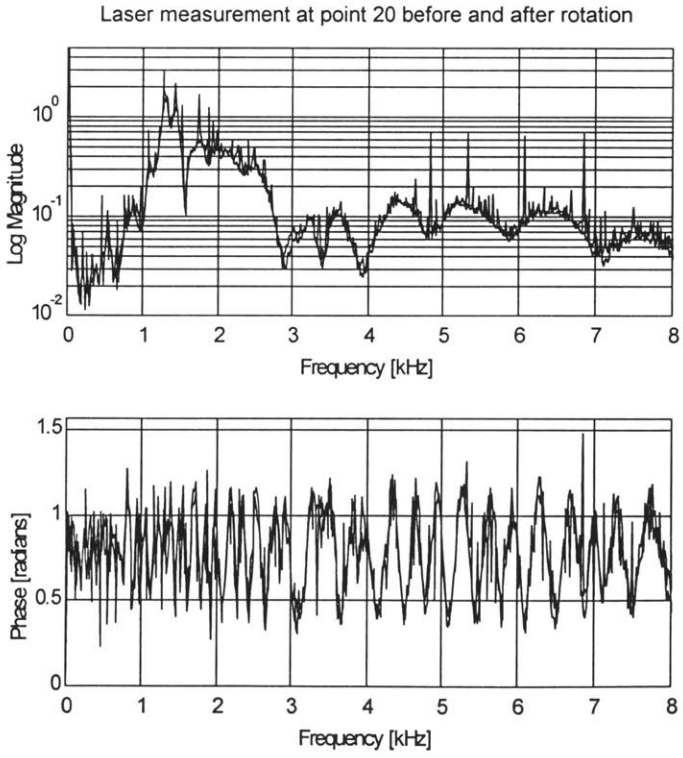

Figure 4-12: Measurement repeatability

The third concern was that the rope would anchor the mode shapes. For the circumferential tests, the laser was stationary and the shell was rotated to each measurement location. Each support rope was a continuous loop which ran around the shell and through a pulley which was suspended from the wooden frame support. The shell rolled along with the loops of rope, so that the rope was always in contact with the bottom half of the shell.

Due to the axial symmetry of a cylindrical shell, the circumferential mode shapes can theoretically be oriented in any rotational direction. In a real cylindrical shell, small deformities in material or shape tend to determine the preferential orientation of the mode shapes. The concern was that the ropes would anchor the mode shapes such that they were oriented in a specific direction relative to the ropes. Since the measurement location was also fixed relative to the ropes, the measured data would always be at the same position in the mode shape. In other words, the mode shape would remain fixed relative to the measurement location, rather than rotating with the shell, making it impossible to measure the mode shape using the described experimental technique.

To check this concern, data was collected simultaneously with an accelerometer mounted at a permanent location and the laser directed at a varying location. Twelve points were marked around the circumference of the shell, one centimeter apart. An accelerometer was mounted on the shell at the same circumferential position as point 1, approximately 1 centimeter down the shell, longitudinally. The input was white noise, similar to the input used in the circumferential array tests. Transfer functions between the input and the response were collected using the SRS analyzer.

First, data was collected with both the laser and the accelerometer at the reference position (the permanent position of the accelerometer). This data was compared and found to agree. (Figure 4-13) Noise baseline data was also collected with both the accelerometer and the laser. This data shows good signal-to-noise ratios for both transducers. (Figure 4-14) Next the shell was rotated 1 centimeter to the next marked position. Laser data was collected at the new location and accelerometer data was collected at the reference position. This process was repeated for all twelve marked points around the circumference. The laser data varies with rotation, as expected.

(Figure 4-15) The accelerometer data is identical at each rotated position, showing that the shell response remains constant with rotation. (Figure 4-16) This data eliminates the concern of mode shape anchoring by showing that the mode shapes are not affected by the rope supports.

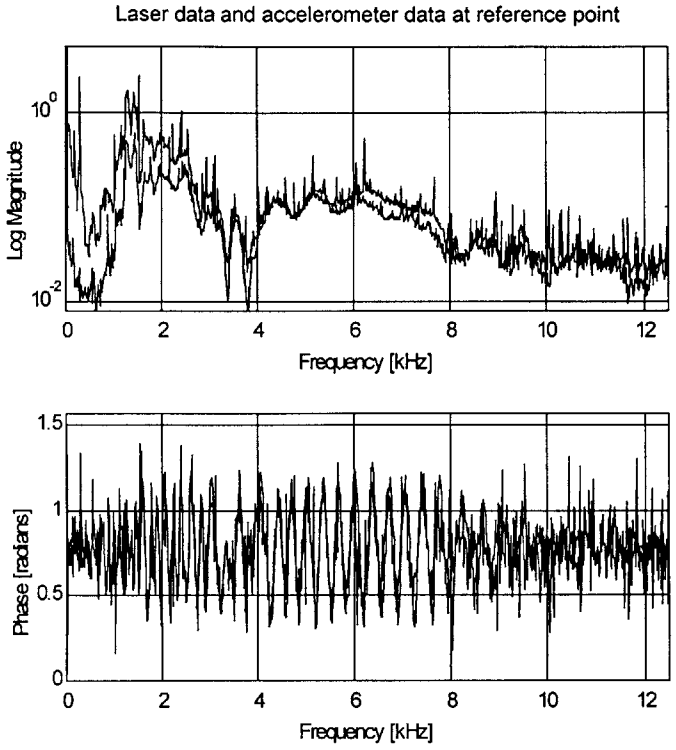

Figure 4-13: Accelerometer vs. laser data at reference point

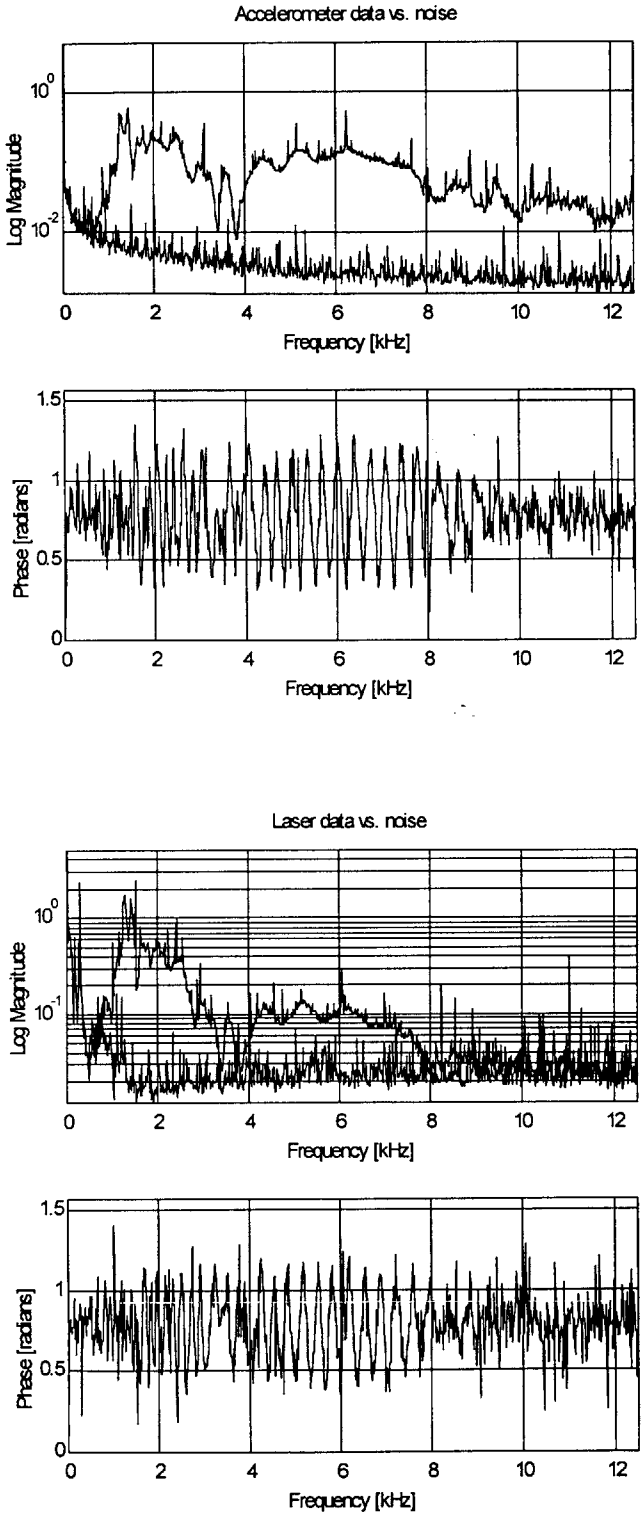

Figure 4-14: Magnitude of the signal vs. magnitude of the noise (upper) and phase of the signal (lower) for the accelerometer (top) and laser (bottom)

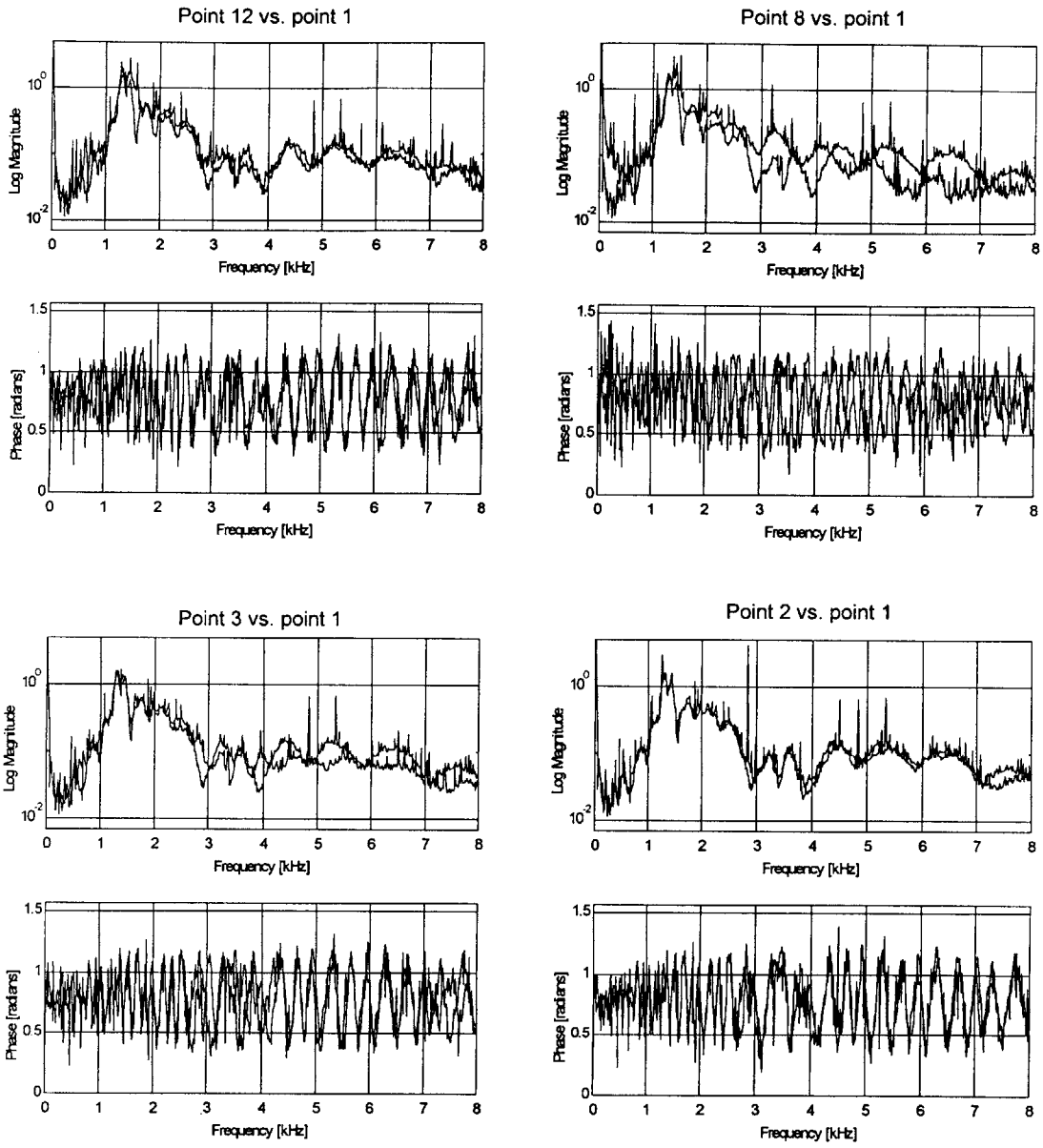

Figure 4-15: Rotation tests - laser data

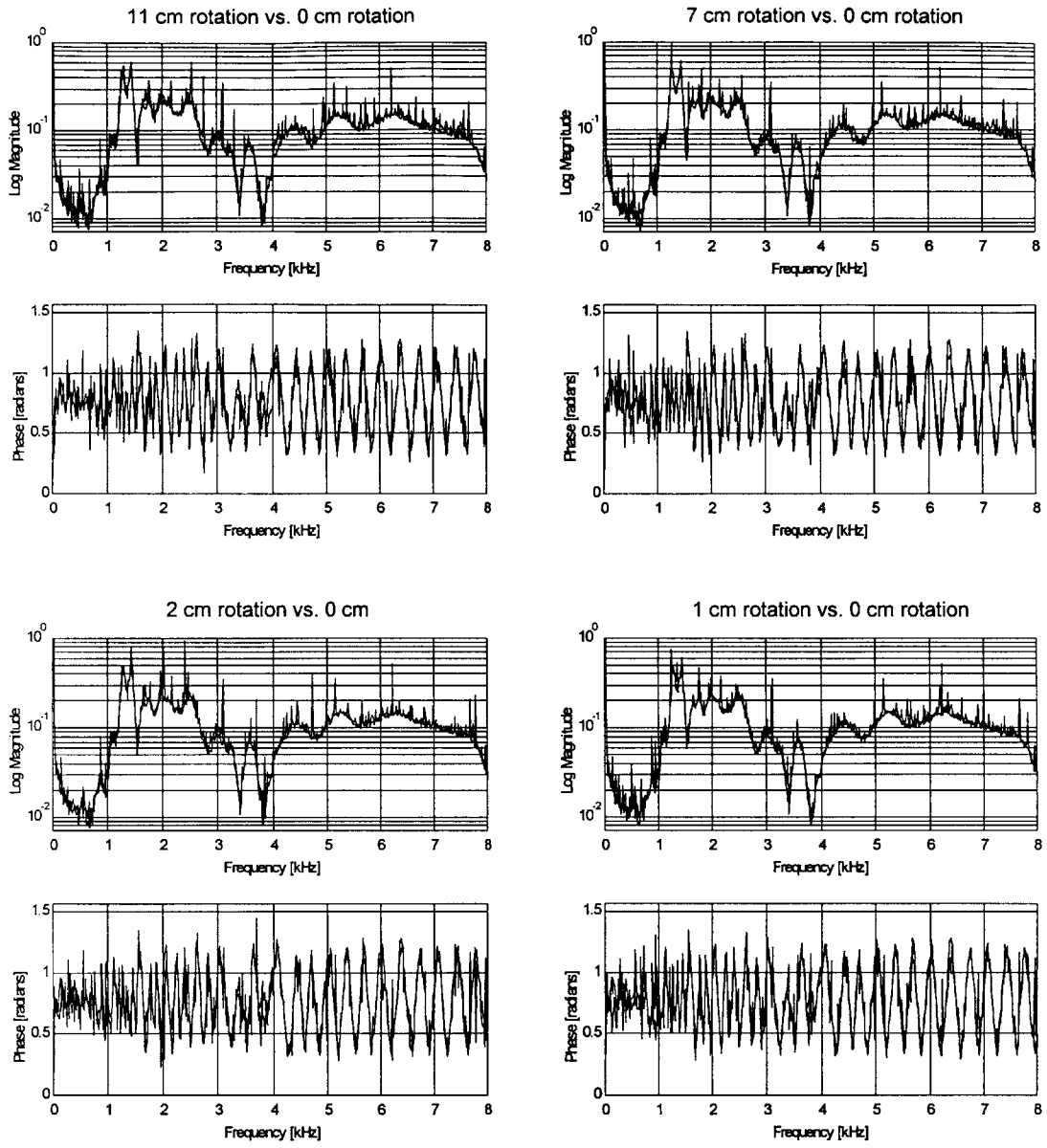

Figure 4-16: Rotation tests - accelerometer data

5. LONGITUDINAL ARRAY MEASUREMENTS

5.1 Test Procedure

The test shell was suspended horizontally from two ropes which ran through pulleys attached to a wooden frame. Transfer functions were measured between the radial velocity of the outer surface of the shell and the broad-band random input signal.

5.1.1 Input to the source array

For the longitudinal tests, the broad-band white noise input signal of 5 Volts rms was low-pass filtered with a cut-off frequency of 25 kHz and a gain of 12 dB. A high-pass 500 Hz filter with unity gain was also applied. The signal was amplified by a power amplifier with a gain of 13 and an impedance transformer with a gain of 5. The longitudinal tests' source signal was thus band-limited to 500 Hz - 25 kHz with a total gain of about 48 dB. The input signal was split twelve ways and sent to the twelve transducers in the source array.

5.1.2 Data Collection

The longitudinal array data was collected using a system created by Joseph E. Bondaryk, a Research Engineer at MIT. Bondaryk's 'ldv' program controlled the laser positioning table and collected the data. The input signal and the laser output signal were digitized using a 12-bit A/D board, anti-alias filtered at 25 kHz, and sampled at 50 kHz. The input autospectrum, output autospectrum and cross-spectrum were calculated over 30 ensembles for 512 linearly-spaced frequencies in the range 0 - 25 kHz. The data was then saved into a MATLAB file.

Data was collected at 120 points, spaced 1 centimeter apart. At each point, the radial velocity of the outer surface of the shell was measured with the laser. The sensitivity of the laser was set to 1 millimeter per second per Volt, the most sensitive setting. The laser lens was 17 inches from the measurement point on the shell, and reflective tape was mounted at the measurement point to improve reflection of the laser beam. The

laser was mounted on a linear positioning table which was controlled by the ldv program. After collecting data at one point, the ldv program moved the laser to the next point in the array and repeated the process.

5.1.3 Calibrations

The input to the sources for the longitudinal array tests was measured via a transfer function between the SRS analyzer's source signal and the output of the Wilcoxon impedance matching network, which is split twelve ways and fed into the twelve piezo-ceramic sources. The calibration was performed with a reduced voltage input of 0.2 volts. The transfer function shows the cumulative effect of the filters and amplifiers used to shape the signal before sending it to the sources. At the high frequency end, the signal is flat up to 20 kHz, then drops off. It is 3 dB down at 25 kHz. In the low frequency range, the signal is flat above about 700 Hertz and 3 dB down at 100 Hertz. The total linear gain in the flat region is 285 (49 dB).

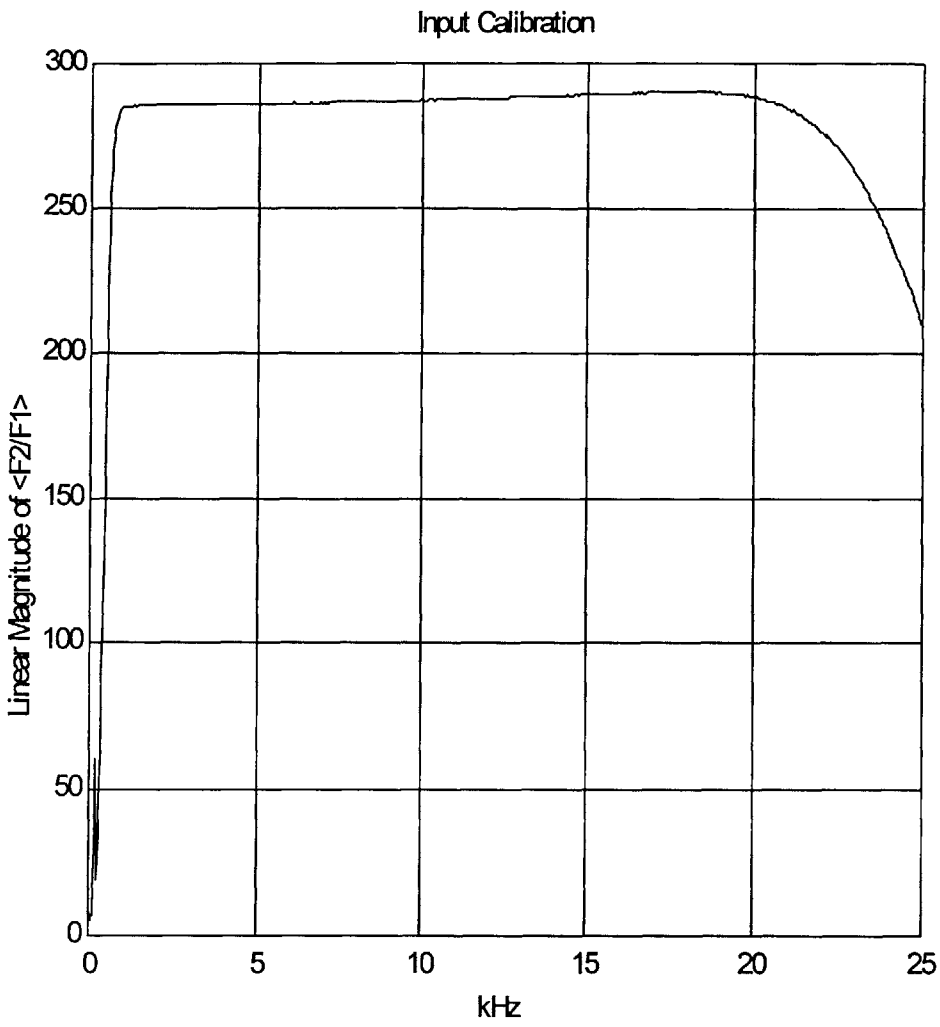

Figure 5-1: Input Transfer Function for the Longitudinal Array Tests

The output from the laser velocimeter was passed through various filters and amplifiers before going into the frequency analyzer for collection and processing. The cumulative effect of these filters and amplifiers is shown in the 'output transfer function' in Figure 5-2. The 'input' for this calibration transfer function was a broad band white noise signal generated by the SRS frequency analyzer, which was used in place of an actual velocity signal from the laser. The output transfer function is basically flat between 200 Hz and 20 kHz with drop-offs to 3 dB down at 100 Hz and 25 kHz respectively. The total linear gain in the flat region is 93 (40 dB).

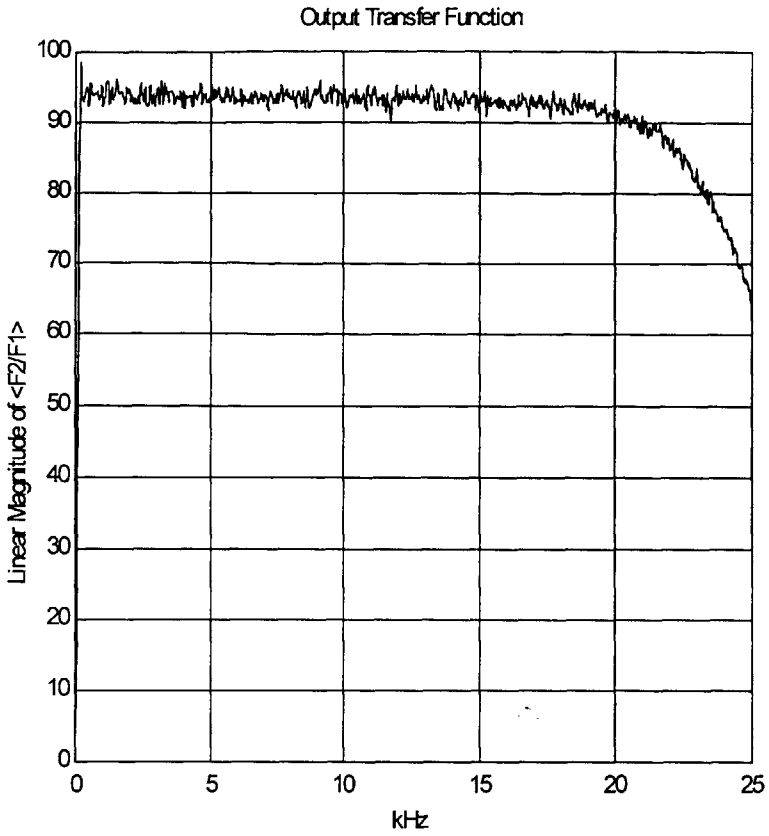

Figure 5-2: Output Transfer Function for the Longitudinal Array Tests

5.2 Plain end results

Figure 5-3 shows the wavenumber-frequency transform of the plain end longitudinal array data. Wavenumber-frequency processing and three-dimensional imaging provide an excellent means to identify the wave dispersion relations. Four dispersion curves are clearly evident. The two less steeply sloped curves show the dispersive relationship between frequency and wavenumber associated with flexural waves. They both have negative wavenumbers, indicating travel in the outgoing direction (away from the source array) on the plain end of the shell.

The two steeply sloped lines with very low wavenumbers are symmetric about $k_xa = 0$, one travelling in the outgoing direction ($-k_xa$) and one travelling in the incoming direction ($+k_xa$). They are straight, indicating non-dispersive membrane waves. Their slope

corresponds to the wavespeed of compressional waves, and they only exist above the ring frequency, indicating that these lines represent mode 0 compressional waves travelling in the plus and minus directions on the shell. The direct wave ($-k_x a$) amplitude is significantly larger than the returning wave amplitude, indicating a high decay rate. A beating pattern of magnitude fluctuations can be seen on the compressional wave lines which is due to interference between the direct wave and a wave reflected off the other end of the shell, as explained in Section 5.2.3.

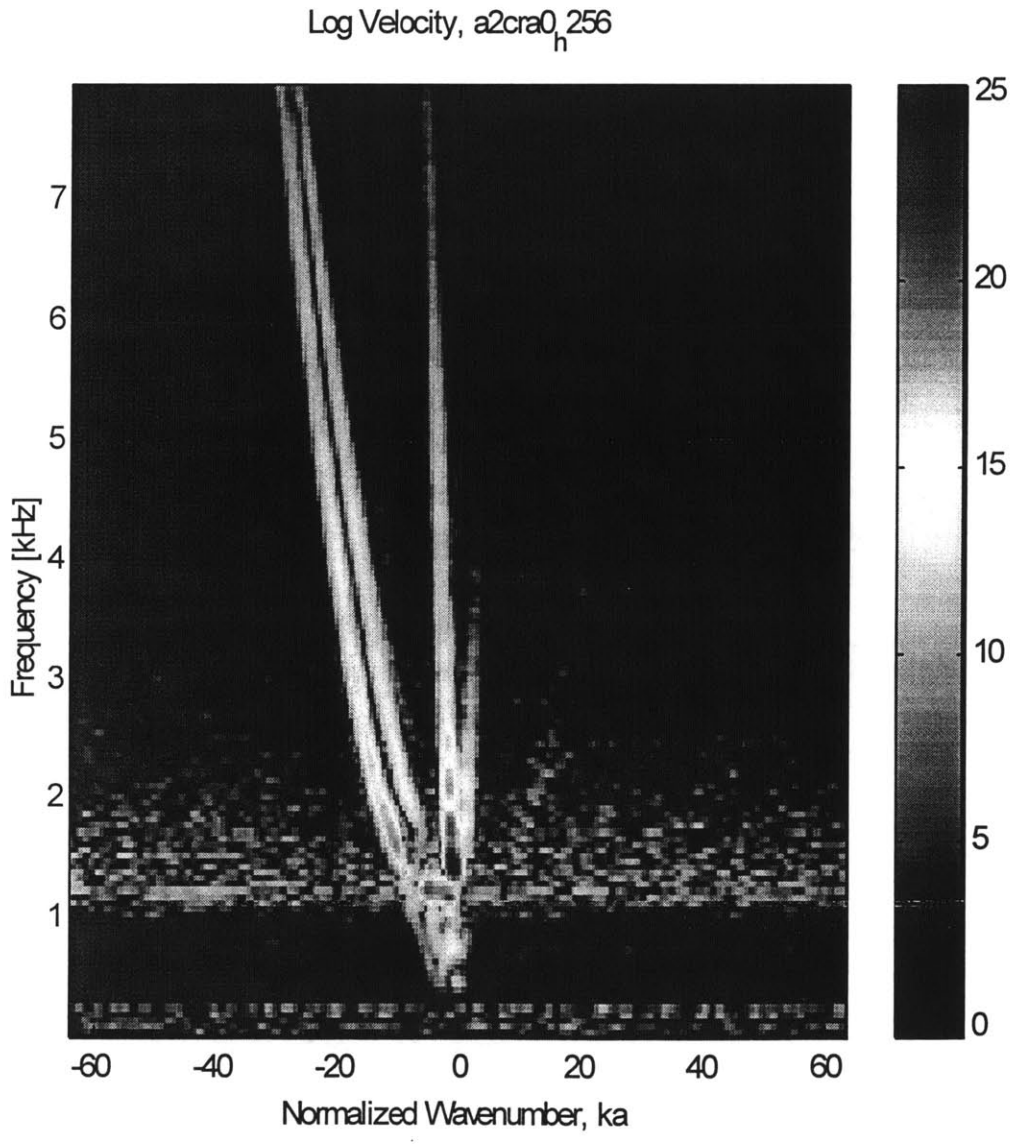

Figure 5-3: Plain end longitudinal array data

5.2.1 Comparison of plain end longitudinal array results with theory

Theoretical dispersion curves for the test shell were calculated using the state space equations presented by Borgiotti and Rosen [22]. These equations represent a theory similar to that of Herrmann-Mirsky, including the effects of rotary inertia and shear deformations. The thick shell theory was required to match the data at high wavenumbers. Since the material properties of PVC were not known, they were selected (within an appropriate range) to best fit the experimental data. The material properties and shell parameters used in this thesis are listed in Table 5-1. The values for the radius and thickness of the cylinder were measured. The shell thickness was found to be slightly larger than the manufacturer's stated nominal thickness. The values for Poisson's ratio and compressional wave speed were tuned to best fit the data. Hayner [20] used a 'plate speed' (c_{LI}) of 1700 m/s to match data collected by Lin [13]. This thesis uses a shell compressional wavespeed ($c_{LII} = \sqrt{(E/\rho)}$) of 1580 m/s and Poisson's ratio equal to 0.42. The corresponding theoretical plate wavespeed ($c_{LI} = \sqrt{(E/\rho(1-\nu^2))}$) is 1741 m/s. These values produces a good match between theoretical dispersion curves and the experimental data.

Radius, a	8 in
Thickness, t	0.2 in
Poisson's ratio, ν	0.42
Compressional wavespeed, c_{LII}	1580 m/s

Table 5-1: Shell parameters used for theoretical modeling

The theoretical dispersion equations formulated by Borgiotti and Rosen [22] were programmed in MATLAB by Mark Hayner. Hayner's program sorts the roots of the eigenvalue matrix formulated by Borgiotti into wave types: flexural, compressional, shear, evanescent, and through-thickness. The flexural, compressional and shear roots sorted by Hayner's programs include complex values below the cut-off frequencies. The complex values were removed from the theoretical curves and the remaining real-valued flexural, compressional and shear dispersion curves were constructed. A plot of

the normalized axial wavenumber as a function of frequency for mode 0 flexural, compressional and shear waves is shown in Figure 4-4. The flexural wave has a curved dispersion relation, indicating its' dispersive nature. The non-dispersive compressional and shear membrane waves have linear dispersion relationships. The compressional wave cuts-off at the ring frequency of the shell, which is the frequency at which the compressional wavelength equals the circumference of the shell. A more detailed discussion of the dispersion curves for cylindrical shells can be found in Reference 7, pages 176-188.

Figure 5-4 shows the longitudinal array data collected on the plain end of the shell overlaid with the theoretical dispersion curves for mode 0 and 12 flexural waves and mode 0 compressional waves. The strongest lines of data line up with the outgoing (negative wavenumber) mode 0 and 12 flexural and mode 0 compressional dispersion curves. A slightly lower level of response occurs along the incoming (positive wavenumber) mode 0 compressional curve. Other features of the data are less clear. There is a faint indication of response along the incoming mode 0 flexural dispersion curve. There are also faint regions of response inside the mode 12 flexural curve, which line up with higher order flexural waves with orders 14 - 20. These regions could be due to small phase errors in the source array.

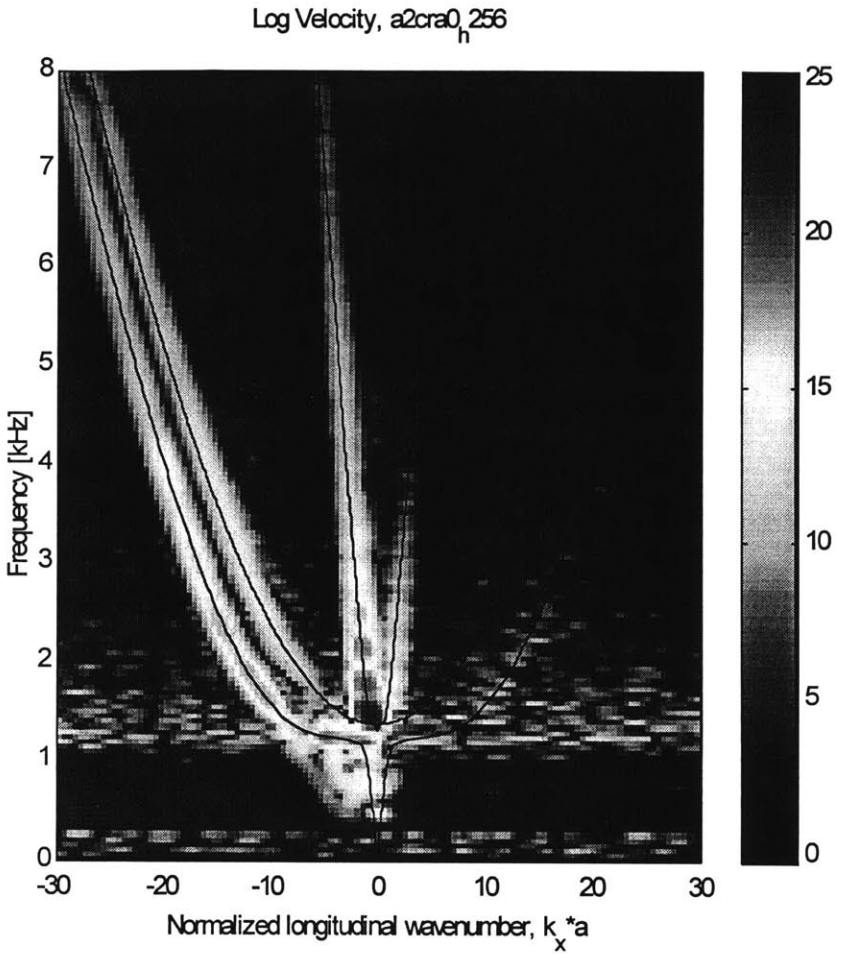

Figure 5-4: Theoretical dispersion curves for mode 0 compressional, mode 0 flexural and mode 12 flexural overlaid on the plain end longitudinal array data

5.2.2 Extraction of the wave amplitudes

The amplitude of each wave shown in the wavenumber-frequency transform was extracted along the theoretical dispersion curves. First, the theoretical dispersion curves were digitized to match the resolution of the wavenumber-frequency transform data. The $k_x a$ resolution is approximately 0.5, while the frequency resolution is approximately 16 Hertz. The mode 0 compressional wave has a steep slope, with $k_x a$ values ranging from 0 to 6 over the 0-8 kHz frequency range. Figure 5-5 shows the wave amplitude extraction points (small circles) for the mode 0 compressional wave. One extraction point was calculated for each frequency in the data. There are many frequency values associated with each $k_x a$ value due to the steep slope. Only the plus-$k_x a$ extraction

points are shown, corresponding to a plus-going mode 0 compressional wave. The extraction points for the minus-going wave are symmetrically located on the minus-$k_x a$ end of the transform.

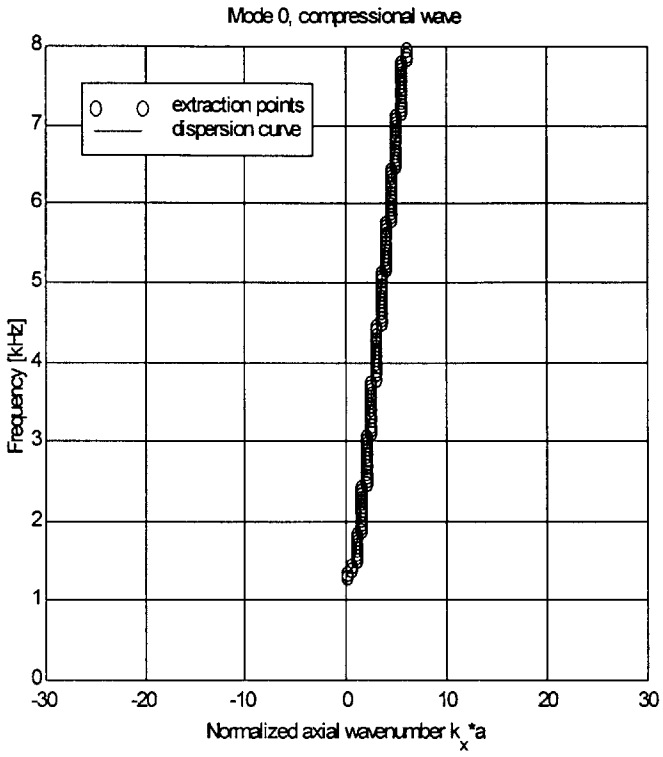

Figure 5-5: Mode 0 compressional wave amplitude extraction points

The flexural waves, modes 0 and 12, were digitized to have one point for each $k_x a$ value in the data due to their almost horizontal slope at $k_x a$ values around 10. This results in rather sparse spacing at very low wavenumbers for the mode 0 flexural wave due to its steep slope. This spacing could be improved if it becomes important for future research. Figures 5-6 and 5-7 show the wave amplitude extraction points for the mode 0 and mode 12 flexural waves.

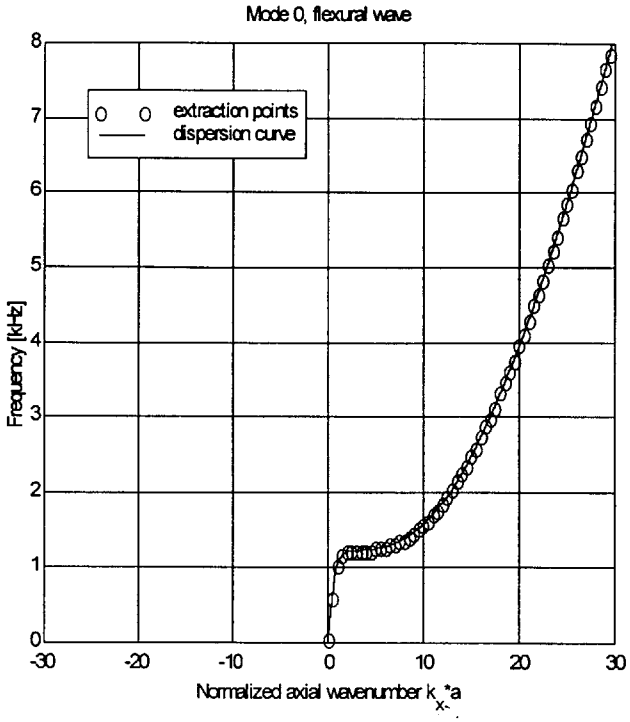

Figure 5-6: Mode 0 flexural wave amplitude extraction points

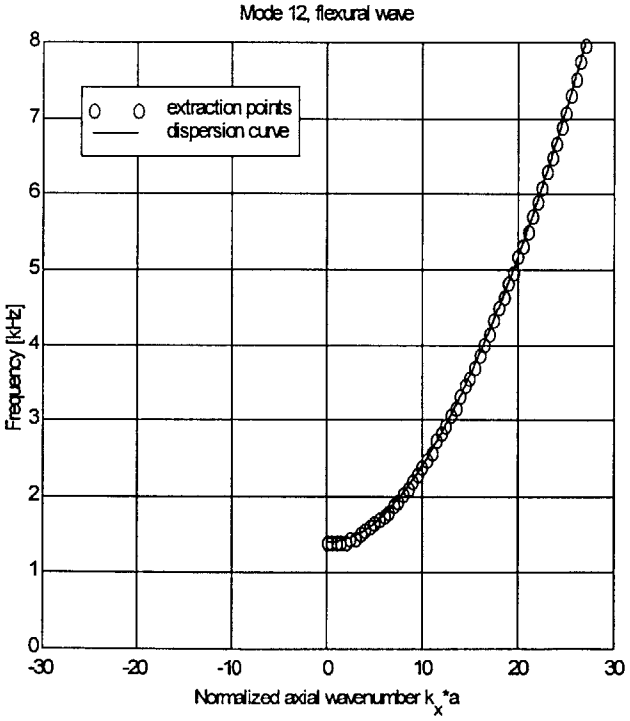

Figure 5-7: Mode 12 flexural wave amplitude extraction points

The magnitude of the wavenumber-frequency transform at each of the extraction points is a measure of the radial component of the wave amplitude of the corresponding wave. The wave amplitudes were extracted for plus-going and minus-going waves of all three present wave types: mode 0 compressional, mode 0 flexural and mode 12 flexural. The wave amplitudes are a measure of the radial particle velocity of the surface of the shell. It is important to remember that the radial amplitude of the flexural waves cannot be directly compared to the radial amplitude of the compressional waves. The particle velocity of flexural waves is primarily in the radial direction, but compressional waves have primarily in-plane particle velocities. The measured (radial) compressional wave amplitude is therefore a small fraction of the total compressional wave amplitude.

In order to clearly identify the different waves travelling on the shell and the wave amplitudes measured by the longitudinal arrays, the following terminology is used. 'Plus-k' and 'minus-k' waves are measured waves with positive and negative wavenumbers, respectively. Waves travelling away from the source array will be called 'outgoing waves', and waves travelling toward the source array will be called 'incoming waves'. Note that on the plain end of the shell, due to the orientation of the longitudinal array, waves travelling away from the source array have negative wavenumbers. These outgoing waves are measured as minus-k waves. Conversely, on the keel end of the shell, waves travelling away from the source array have positive wavenumbers. They are also outgoing waves, but they are measured as plus-k waves. Finally, waves which come directly from the source (before any reflections) are called 'direct waves'. Waves which are travelling toward the source array after reflecting or scattering at discontinuities are called 'reflected' or 'returning' waves.

By tracing the path of each wave as it travels away from the source we can determine which waves will be present in the extracted plus-k and minus-k wave amplitudes on each end of the cylinder. Figure 5-8 shows a diagram of the wave paths. On the plain end of the cylinder, the three waves generated by the source array (the direct waves) propagate freely until they hit the end of the cylinder, where they are reflected with minimal loss of energy. Some wave conversion between membrane and flexural waves is expected when the waves impinge on the free end of the shell. The waves then freely propagate back along the cylinder, passing the plain end longitudinal array a second

time, in the opposite direction. The reflected waves continue to propagate, passing the source array and the keel end longitudinal array, but by this point they have lost a great deal of energy and are assumed to have very small amplitude.

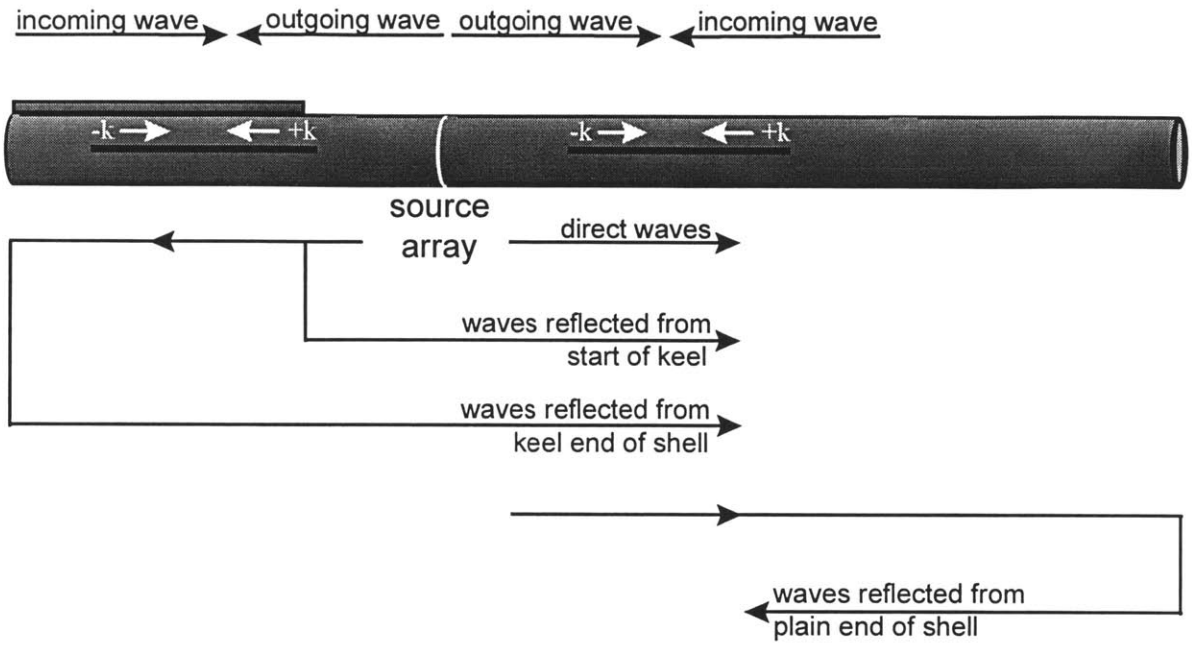

Figure 5-8: Tracing the wave paths to track the plus-k and minus-k waves measured by the longitudinal array on the plain end of the shell

On the keel end of the cylinder, the three waves generated by the source array (the direct waves) first hit the start of the keel. The discontinuity at the start of the keel reflects a small amount of wave energy into the three incident wave types. These reflected waves decay as they propagate toward the plain end of the cylinder, so that they are assumed to be negligible by the time the reach the plain end longitudinal array. The discontinuity at the start of the keel also scatters some of the wave energy into waves with different modes or wave types, some of which continue to propagate along the keel. (The wave coupling at the keel is discussed in more detail in Chapter 6.) The direct waves also propagate along the keel, which transfers additional energy into other waves. The waves pass the keel end longitudinal array and are reflected at the end of the cylinder to propagate past the keel end longitudinal array a second time, in the opposite direction. By the time they reach the plain end longitudinal array the reflected

waves have lost much of their energy due to dissipation through material damping and scattering into other waves.

By tracing the wave paths, the outgoing (minus-k) waves measured by the plain end longitudinal array have been shown to be a combination of 1) the direct waves from the source, 2) waves reflected off the start of the keel, and 3) waves reflected off the keel end of the shell. The incoming (plus-k) waves are the waves reflected from the plain end of the shell. The outgoing and incoming wave amplitudes measured on each end of the shell are discussed below.

The wave amplitude for the mode 0 compressional wave was determined at the extraction points shown above in Figure 5-5. The extraction points are overlaid on the data for the plain end of the shell in Figure 5-9. The extracted radial wave amplitude and phase for the outgoing compressional mode 0 wave are shown in Figure 5-10. The wave amplitude decreases as the frequency increases. The wave amplitude is approximately 25 dB at the ring frequency and approximately 20 dB lower at 8 kHz. The interference or beating pattern seen in the wave amplitude indicates the presence of more than one wave. The beating pattern will be analyzed in Section 5.2.3.

The amplitude of the incoming wave decreases more quickly with frequency than the outgoing wave amplitude. The extraction points and the extracted radial wave amplitude and phase for the incoming compressional mode 0 wave on the plain end of the shell are shown in Figures 5-11 and 5-12. The peak at the ring frequency is probably the sum of the incoming wave amplitude and smeared amplitude from the outgoing wave (due to the Hanning window). If the initial peak is ignored, the amplitude decreases from about 15 dB at 2 kHz to 0 dB at 5 kHz. This steeper drop-off is explained by a frequency dependent wave decay rate, as discussed in Section 5.2.3. The beating pattern seen in the outgoing wave amplitude is also seen in the incoming wave amplitude. This will be discussed in Section 5.2.3.

The extraction points and the extracted radial wave amplitude of the outgoing and incoming mode 0 flexural waves on the plain end of the shell are shown in Figures 5-13, 5-14, 5-15 and 5-16. The amplitude of the outgoing flexural mode 0 wave is similar to that of the outgoing mode 0 compressional wave. The data extraction algorithm takes

the data with the highest amplitude within a range around the extraction point. The extracted incoming wave amplitude shown in Figure 5-16, which essentially follows the peaks in the noise amplitude, is contaminated by noise.

The extraction points and the radial wave amplitudes of the outgoing and incoming mode 12 flexural waves on the plain end of the shell are shown in Figures 5-17, 5-18, 5-19 and 5-20. The amplitude of the outgoing mode 12 flexural wave is approximately 5 dB lower than the amplitude of the outgoing mode 0 compressional wave. The incoming mode 12 flexural wave amplitude shown in Figure 5-20, which essentially follows the peaks of the noise amplitude, is contaminated by noise. The high amplitudes near the ring frequency are probably due to spreading of the mode 0 compressional waves, rather than any presence of the incoming mode 12 flexural wave.

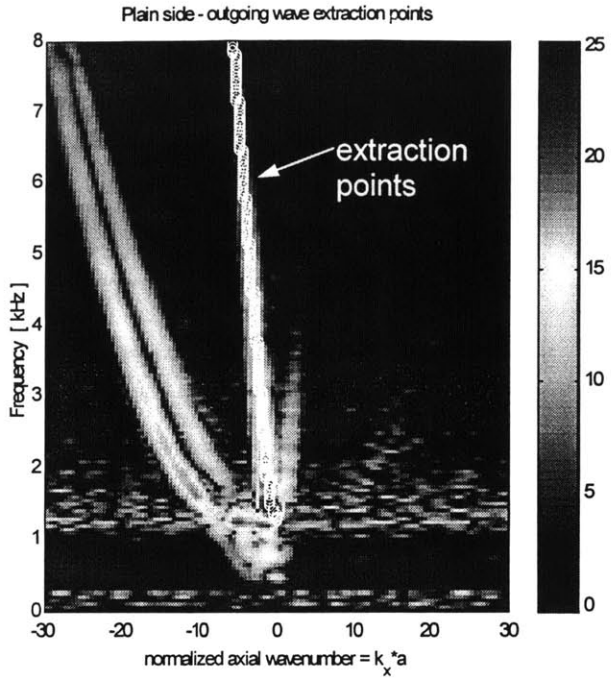

Figure 5-9: Extraction points for the OUTGOING mode 0 compressional wave measured on the plain end of the shell (small circles)

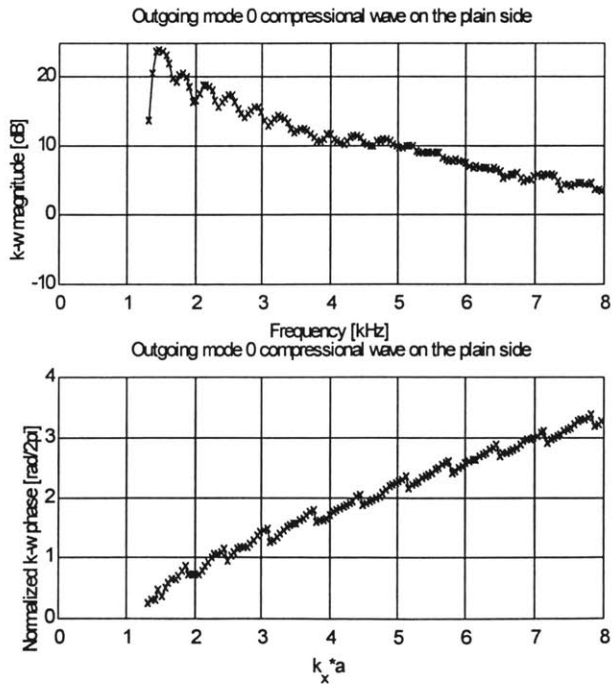

Figure 5-10: Extracted radial wave amplitude and phase of the OUTGOING mode 0 compressional wave measured on the plain end of the shell

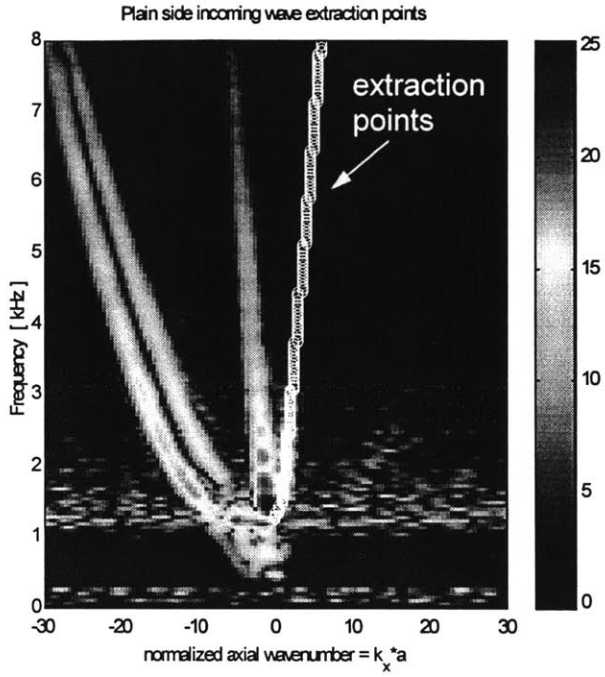

Figure 5-11: Extraction points for the INCOMING mode 0 compressional waves on the plain end of the shell (small circles)

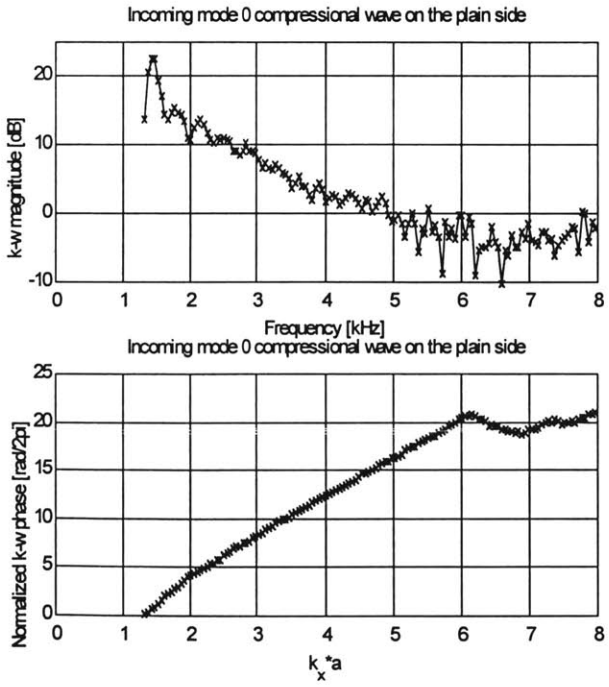

Figure 5-12: Extracted radial wave amplitude and phase of the INCOMING mode 0 compressional waves on the plain end of the shell

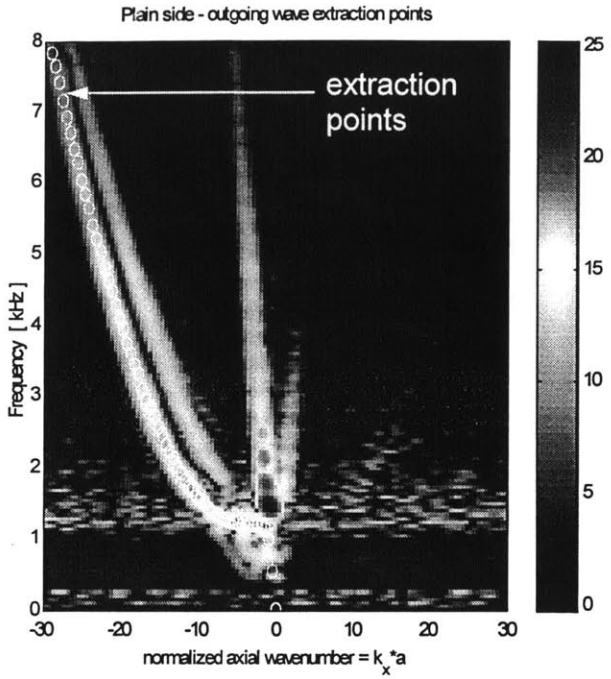

Figure 5-13: Extraction points for the OUTGOING mode 0 flexural waves on the plain end of the shell (small circles)

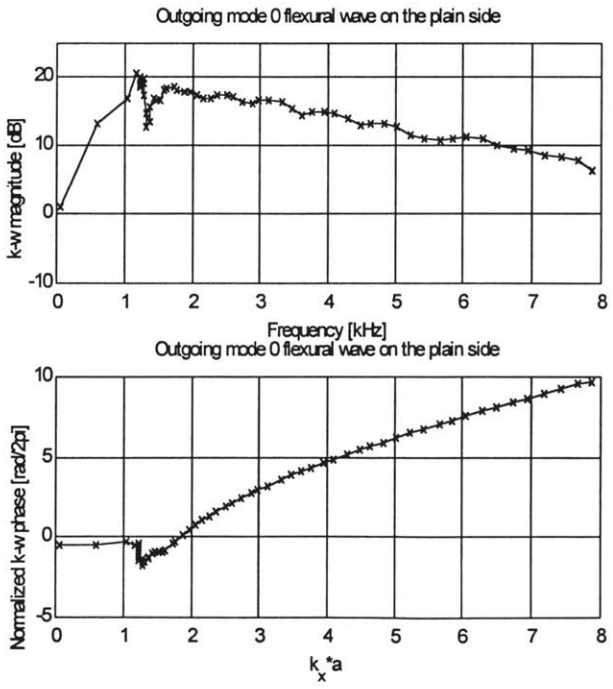

Figure 5-14: Extracted radial wave amplitude and phase of the OUTGOING mode 0 flexural waves on the plain end of the shell

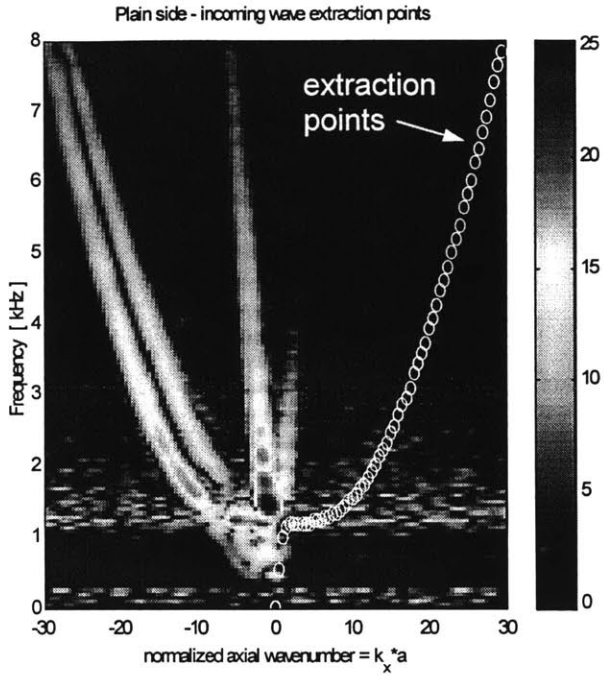

Figure 5-15: Extraction points for the INCOMING mode 0 flexural waves on the plain end of the shell (small circles)

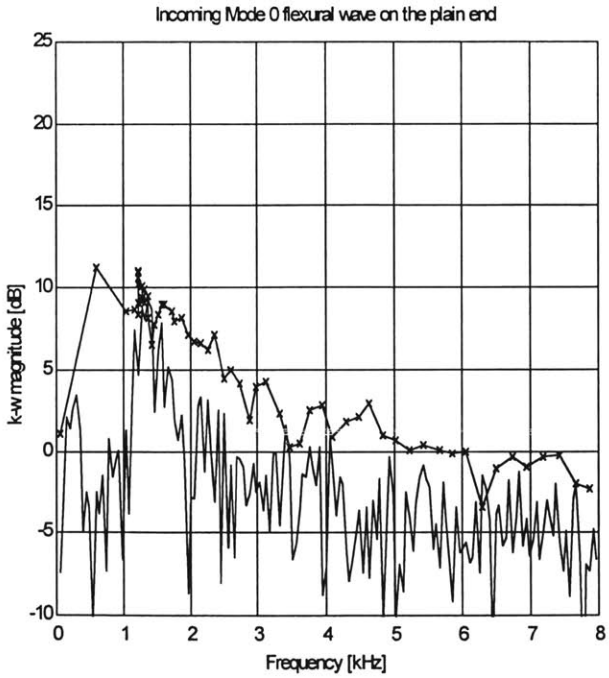

Figure 5-16: Extracted radial wave amplitude of the INCOMING mode 0 flexural waves on the plain end of the shell (-x-), and noise amplitude(- -)

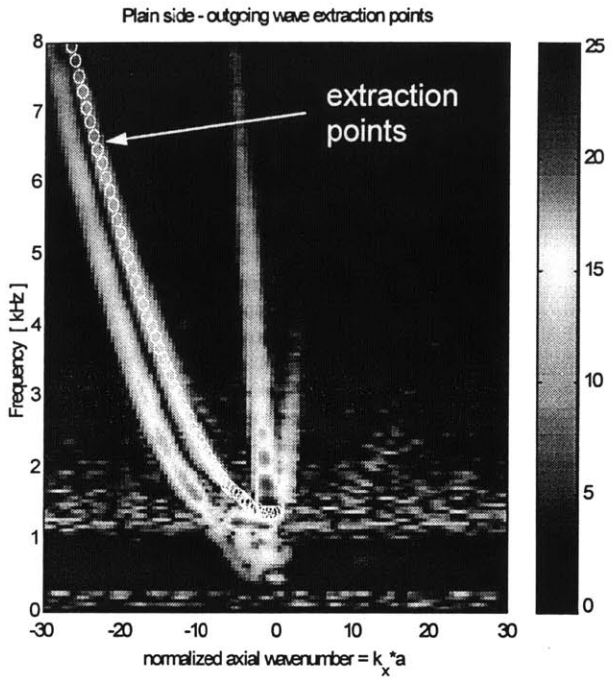

Figure 5-17: Extraction points for the OUTGOING mode 12 flexural waves on the plain end of the shell (small circles)

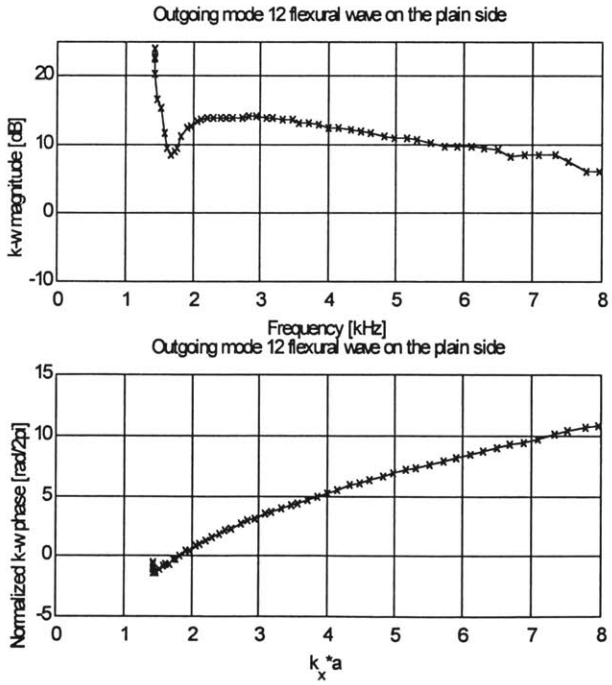

Figure 5-18: Extracted radial wave amplitude and phase of the OUTGOING mode 12 flexural waves on the plain end of the shell

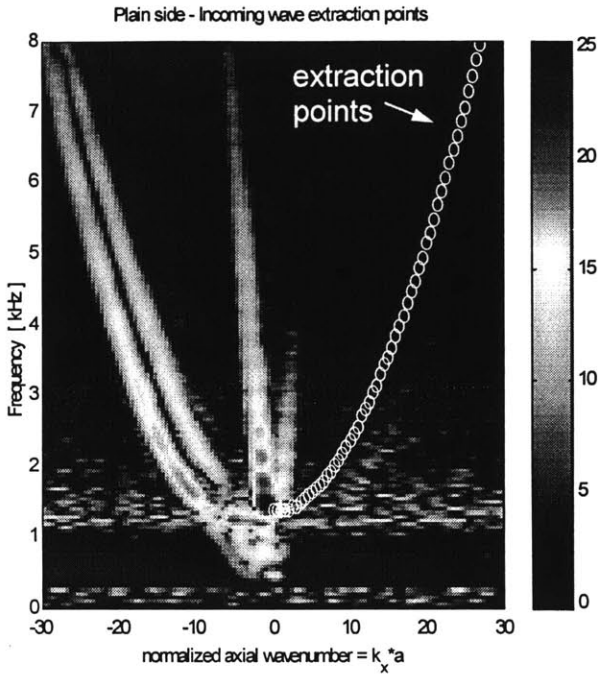

Figure 5-19: Extraction points for the INCOMING mode 12 flexural waves on the plain end of the shell (small circles)

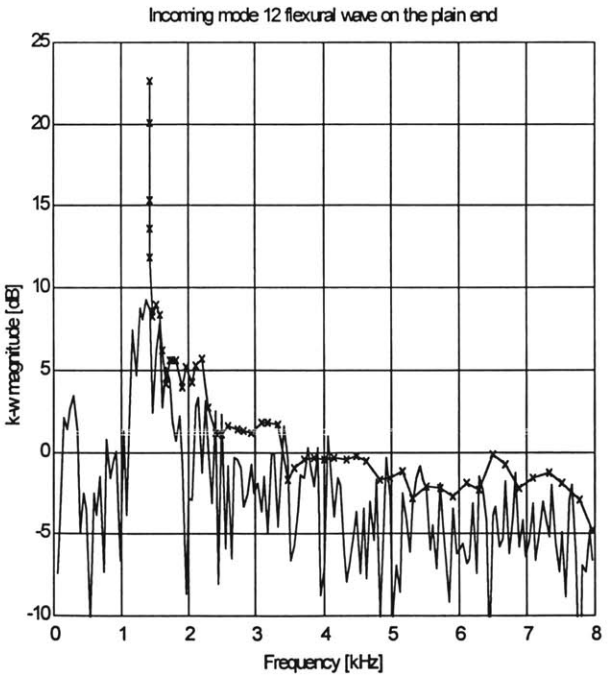

Figure 5-20: Extracted radial wave amplitude of the INCOMING mode 12 flexural waves on the plain end of the shell (-x-), and noise amplitude (- -)

5.2.3 Compressional wave amplitudes and decay rates

The interference or beating pattern observed in outgoing and incoming compressional mode 0 wave amplitudes on the plain end of the cylinder indicates the presence of more than one wave. In section 5.2.2 the paths of the waves were traced as they traveled along the shell. The outgoing waves measured by the plain end longitudinal array were shown to be a combination of 1) the direct waves from the source, 2) waves reflected off the start of the keel, and 3) waves reflected off the keel end of the shell. Assuming that the amplitudes of the waves reflected off the start of the keel are negligible by the time they reach the plain end longitudinal array, the measured outgoing wave amplitude can be decomposed into its two wave components: the direct waves and the waves reflected off the keel end of the shell.

This hypothesis can be supported by calculating the distance between the peaks in the beating pattern based on the phases of the two component waves.

The amplitude ratio of the two component waves can be determined from the peak-to-valley ratio of the beats. Each peak in measured amplitude equals the sum of the two component wave amplitudes, while each valley equals the difference. Expressing the measured peak and valley amplitudes as A_p and A_v and expressing the amplitudes of the two component waves as A_d (direct wave) and A_r (reflected wave), the amplitude ratio can be expressed as follows.

$$A_p = A_d + A_r$$

$$A_v = A_d - A_r$$

$$A_r/A_d = (A_p/A_v - 1) / (A_p/A_v + 1)$$

From Figure 5-21 the amplitudes of the peak and valley are seen to differ by about 3dB at 2.5 kHz, which corresponds to a ratio of A_p/A_v equal to 2. Thus the predicted amplitude ratio of the two component waves, A_r/A_d, is 1/3 at 2.5 kHz. Logically, the smaller of the two component waves would be the compressional wave reflected off the keel end of the shell.

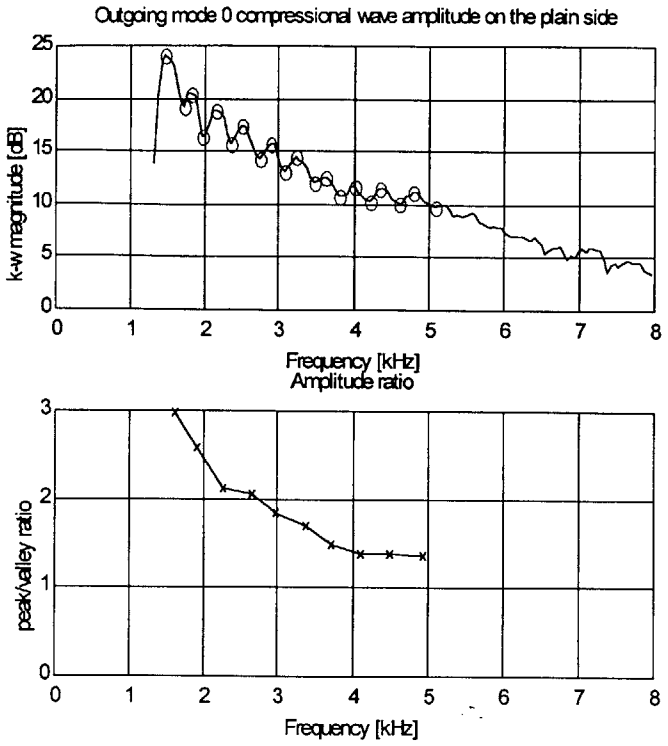

Figure 5-21: Ratio of peak amplitudes to valley amplitudes for the outgoing compressional wave on the plain end of the shell

The decay associated with this decrease in wave amplitude can be calculated by assuming the following form for the wave amplitudes:

$$A_r = A_d e^{-\alpha k(x_r - x_d)}$$

where α is the decay coefficient, k is the frequency-dependent wavenumber of the wave, x_d is the distance traveled by the direct wave and x_r is the distance traveled by the wave reflected off the keel end of the shell. The direct wave has traveled 100.7 cm, and the reflected wave has traveled 554.1 cm. Thus the reflected wave has traveled 453.4 cm farther than the direct wave. At 2.5 kHz, the wavenumber of the mode 0 compressional wave is approximately 10 m^{-1}. Using these values, the decay at 2.5 kHz can be estimated to be:

$$\alpha_{beating}\ (2.5\ kHz) = -\ln(A_r/A_d)/k*(x_r-x_d) = -\ln(0.33) / (10\ m^{-1})*(4.5m) = 0.025$$

Figure 5-22 shows more exact calculations for the decay coefficient, which agree with the above estimate. The average decay coefficient is 0.0267 for frequencies between one and three-and-a-half times the ring frequency (1.4 kHz - 5 kHz).

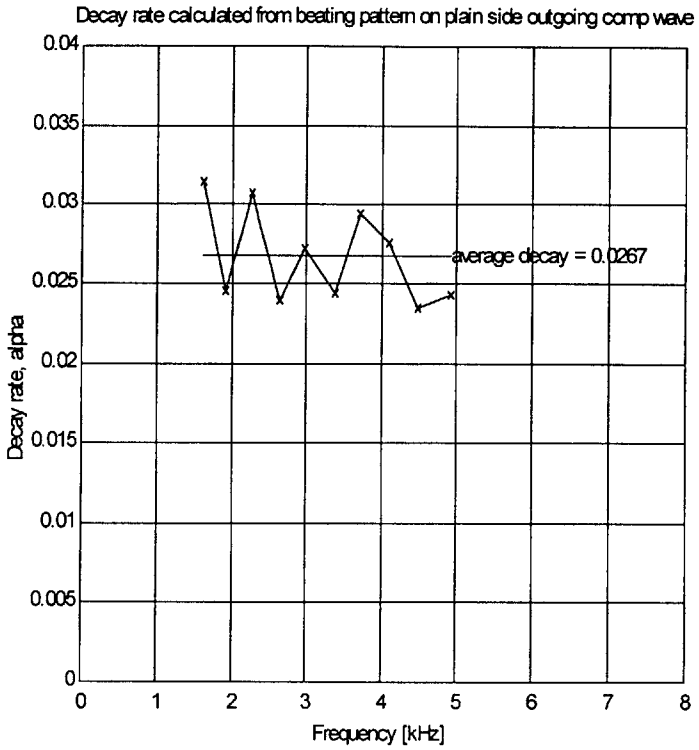

Figure 5-22: Decay coefficient for the mode 0 compressional wave calculated using the beating pattern on the outgoing plain end longitudinal array data

Another measure of the decay rate of the compressional wave can be calculated using the ratio between the amplitudes of the incoming and outgoing waves on the plain end of the shell. The measured amplitude of the incoming waves on the plain end of the shell is compared to the amplitude of the outgoing waves in Figure 5-23. The ratio between the wave amplitudes can be approximated to be 0.26 at 2.5 kHz. Figure 5-8 shows that the distance from the center of the plain end longitudinal array to the plain end of the shell is 282.2 cm. Thus the incoming compressional wave has traveled 564.4 cm farther than the outgoing wave.

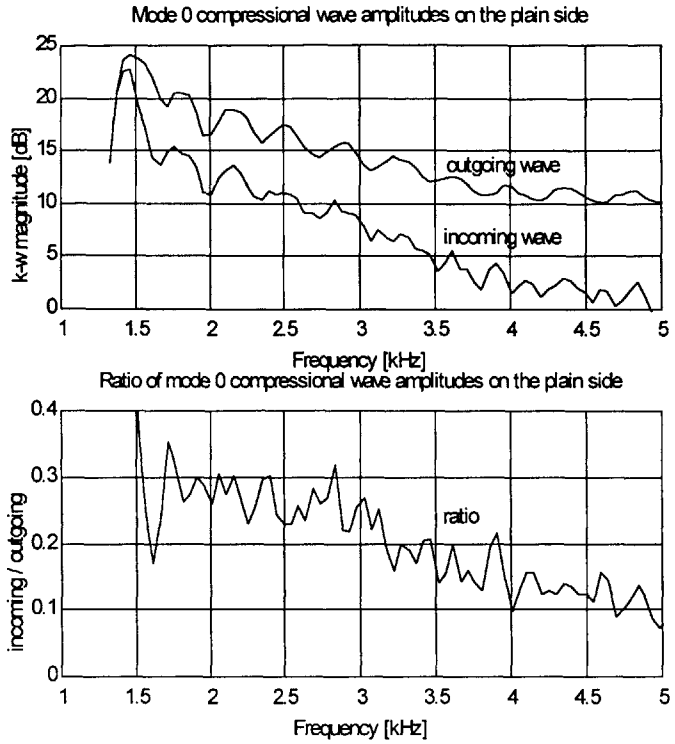

Figure 5-23: Outgoing and incoming wave amplitudes measured by the longitudinal array on the plain end of the shell.

The decay associated with the decrease in amplitude between the outgoing and incoming waves is calculated below at 2.5 kHz. The amplitude of the outgoing wave is A_o, the amplitude of the incoming wave is A_i, and the distances traveled by the two waves are x_i and x_o respectively. The wavenumber of the compressional wave at 2.5 kHz is taken from the wavenumber-frequency data to be 10 m^{-1}.

$\alpha_{incoming}$ (2.5 kHz) = $-\ln(A_i/A_o)/k(x_i-x_o) = -\ln(0.26) / (10\ m^{-1})*(5.6\ m) = 0.024$

This estimate is supported by the more exact calculations shown in Figure 5-24, which shows an average decay coefficient of 0.0240 for frequencies between 2.6 kHz and 5 kHz.

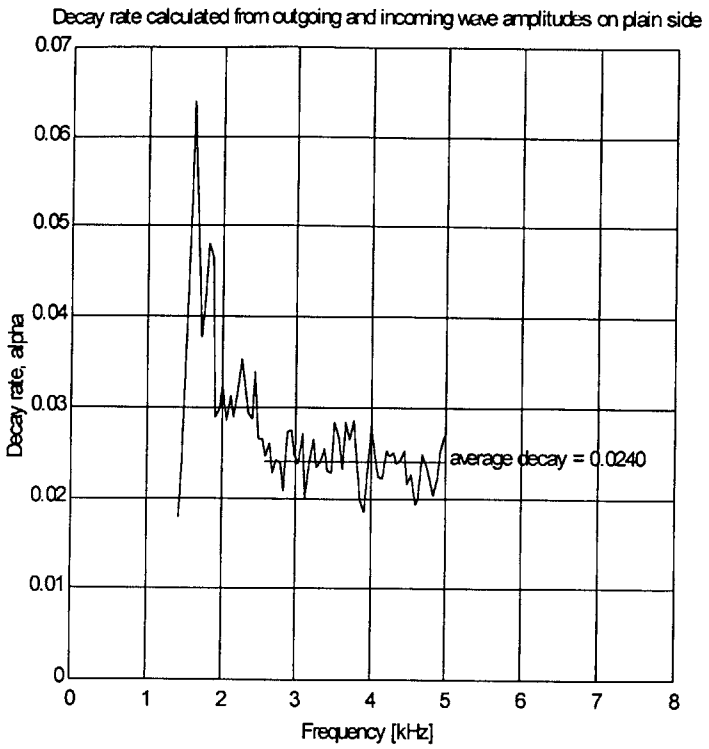

Figure 5-24: Decay rate for the mode 0 compressional wave calculated using the outgoing and incoming wave amplitudes from the plain end longitudinal array data

The two methods for calculating the decay give slightly different results. The decay coefficient calculated from the beating pattern in the outgoing wave on the plain end of the shell is 0.0267. This decay coefficient is a measure of the energy lost by the wave reflected off the keel end of the shell, as shown in Figure 5-8. This wave travels along the keel for 3 meters on its way from the source array to the keel end of the shell and back to the plain end measurement array. Thus, in addition to material damping, the decay measures losses into other wave types due to coupling at the keel and at the end of the shell.

The decay rate calculated from the ratio between the outgoing and incoming wave amplitudes measured by the plain end longitudinal array is 0.0240. This decay is based on travel along the plain end of the shell. Thus the decay measures loss due to material damping and loss into other wave types due to coupling at the end of the shell.

The difference in the two calculated decay coefficients is 0.0027. This difference is due to wave coupling at the keel. The decay rate calculated from the beating pattern is based on a travel path of 453.4 centimeters, of which 304.8 centimeters is along the keel. More direct evidence of the wave coupling at the keel is shown in the data from the keel end array.

5.3 Results for the end of the shell with a keel

Figure 5-25 shows the wavenumber-frequency transform measured by the longitudinal array on the end of the shell with the keel. Outgoing waves measured by the keel end array have positive wavenumbers due to the placement of the array relative to the source array. The four dispersion curves seen in the plain end data are also seen on the keel end. The two less steeply sloped curves show the dispersive relationship between frequency and wavenumber associated with flexural waves. They both have positive wavenumbers, indicating travel in the outgoing direction (away from the source array). The two steeply sloped lines with very low wavenumbers are symmetric about $k_x a = 0$, one travelling in the outgoing direction ($+k_x a$) and one travelling in the incoming direction ($+k_x a$). They are straight, indicating non-dispersive membrane waves. Their slope corresponds to the wavespeed of compressional waves, and they begin above the ring frequency, suggesting that these lines represent mode 0 compressional waves travelling in the plus and minus directions on the shell.

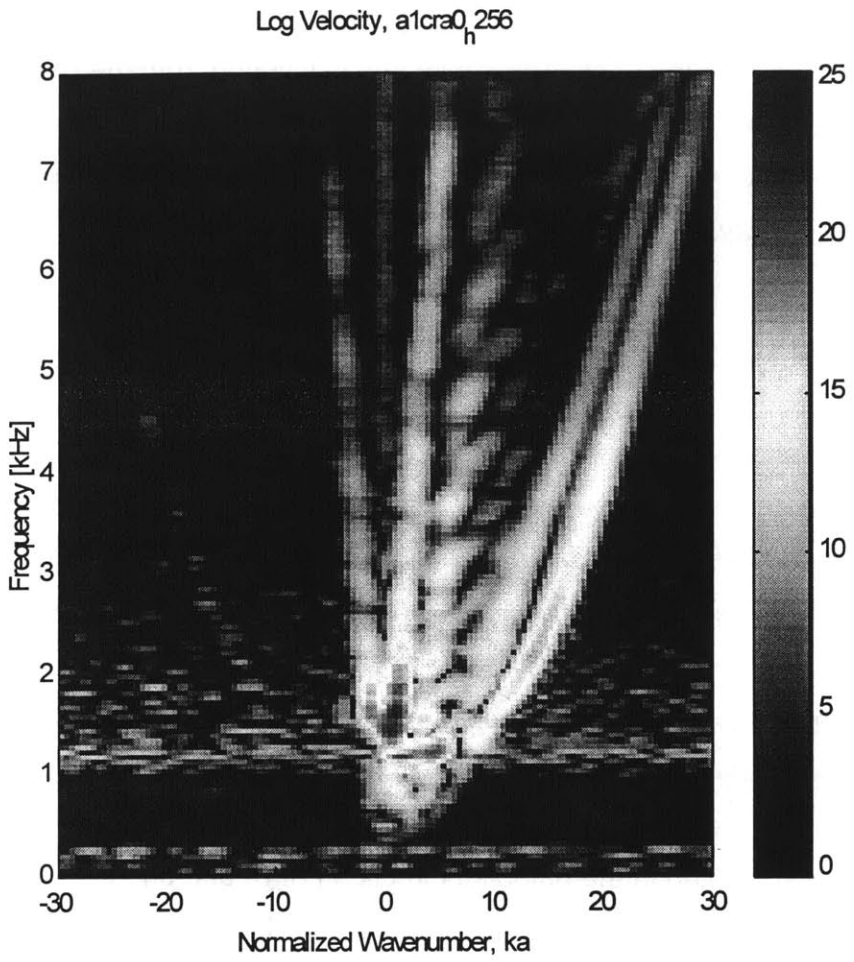

Figure 5-25: Keel-end longitudinal array data

The interesting feature of the keel end data is the new response which lies between the compressional and flexural dispersion curves on the positive end of the wavenumber axis. Rather than a solid line of response, the data shows points of higher response that fall roughly along a line. This line lies in the vicinity of the mode 0 shear wave, but there is no excitation of the shear wave. Comparison with theoretical dispersion curves shows that the new response falls outside the shear line. The axial wavenumbers of the new response are slower than the membrane waves on the shell, and faster than the bending waves.

5.3.1 Comparison with theory

Figure 5-26 shows the theoretical dispersion curves for a homogeneous cylinder (without a keel) overlaid on the keel end data. The two outer curves are the mode 0 and mode 12 flexural waves. The inner two v-shaped curves are the mode 0 shear (outer) and compressional (inner) waves. The wavenumbers of the mode 0 compressional wave and the mode 12 flexural wave go to zero close to the ring frequency of the shell. Within the wavenumber resolution of the data, the addition of the keel has very little effect on the dispersion relations for the n=0 compressional and flexural waves and the n-12 flexural wave. A small difference is observed for the flexural waves at high wavenumbers, where the slope has slightly increased.

A new line of response is seen in the data which lies between the shear wave and the mode 12 flexural wave. This wave will be discussed in more detail in Chapter 6.

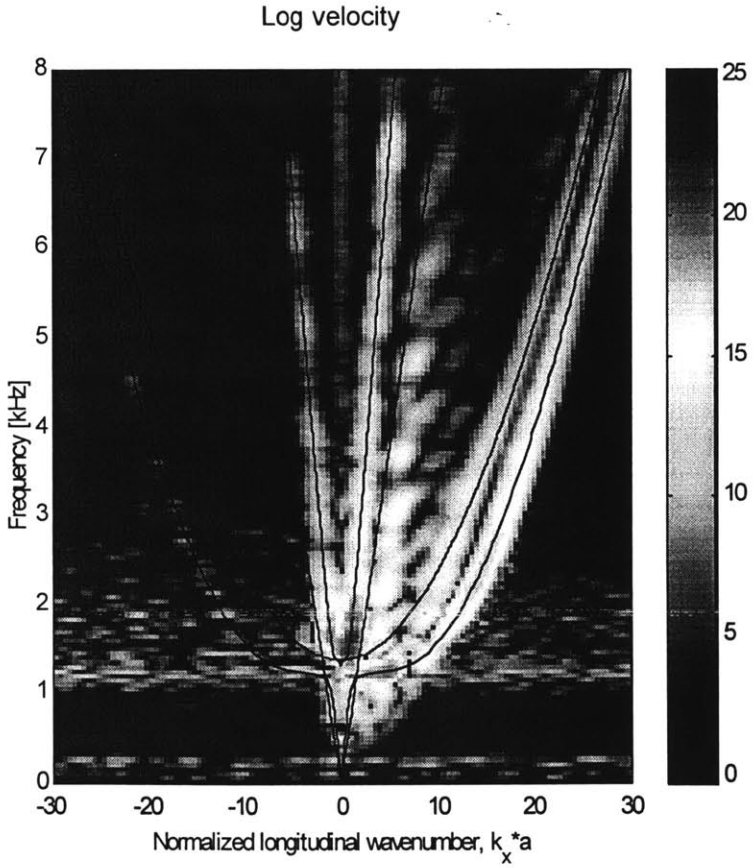

Figure 5-26: Theoretical dispersion curves overlaid on the keel end data

6. MODELING THE ADDITION OF A KEEL

6.1 Wave coupling due to the keel

New wave types are expected in the shell response due to addition of the keel. These result from two effects. First, the keel acts as a discontinuity restraining the motion of the shell and causing the shell waves to be coupled. Shell waves not directly excited by the source array will appear in the shell response due to coupling at the keel discontinuity. Second, since the keel is a wave-bearing system, new wave types will be introduced into the shell response.

The keel and the shell are both wave-bearing systems. Thus, coupling these two systems will result in multiply-branched dispersion curves. [6] The total number of branches is governed by the total number of degrees of freedom of the coupled system. Addition of the keel adds degrees of freedom corresponding to flexural, longitudinal, and torsional motion of the keel.

For lightly coupled systems, the dispersion curves for the different wave types in the coupled system follow the dispersion curves for the uncoupled systems. Although small amounts of coupling cause the motions of the two systems to be coupled, it is still possible to identify waves for which the dominant response is in one of the coupled systems. Higher coupling causes significant shifts in the dispersion curves. It is no longer possible to associate a wave of the coupled system with one of the uncoupled dispersion curves.

Based on the above discussion, the dispersion curves for the test shell should change due to the addition of a keel, but the extent of the change will depend on the strength of the coupling between the shell and the keel. The changes in wavenumber may be smaller than the resolution of the axial array measurements and therefore may not be observed in the data. The new waves associated with the coupled system may be evanescent or they may not have enough energy to show up in the measurements. In addition, waves whose principal motion is in the keel may not be observed by

measurements taken at the longitudinal array which is approximately 90 degrees from the keel.

The measured data show no significant change in the dispersion curves corresponding to the n=0 compressional and flexural waves and the n=12 flexural wave. However, a new dispersion curve is observed. This curve corresponds to a coupled wave in the keel and shell.

6.2 Keel wave excitation and response

Since the keel and the shell are made from the same material, the n=0 compressional wave in the uncoupled shell and the longitudinal wave in the keel will have similar dispersion curves. Due to differences in the Poisson effect, the membrane compressional waves in the shell travel slightly faster than longitudinal wave in the keel. However, the difference between the wavespeeds is so small that changes in the dispersion curves for these waves are expected to be smaller than the wavenumber resolution of the measurements. Thus, even though the n=0 compressional wave is coupled to the longitudinal keel wave, the dispersion relation for the coupled system is not significantly changed from that for the n=0 compressional wave in the homogeneous shell.

The n=0 compressional wave will also be coupled to bending waves in the keel, since the attachment between the shell and the keel is off the neutral axis of the keel. Extension of the shell in the axial direction results in bending of the keel in the stiff direction. The dispersion relation for uncoupled keel bending was developed using a theoretical model for beam bending which includes the effects of shear deformations but assumes that the effects of rotary inertia are negligible. The wavenumber of uncoupled keel bending waves, k_b, was predicted from the following dispersion relation:

$$EIk_b^4 = \rho A\omega^2 + \frac{\rho\kappa^2 AE}{k'G}\omega^2 k_b^2$$

where ρ is the density, A is the cross-sectional area, κ is the radius of gyration of the cross-sectional area, E is Young's modulus, k' is a shear correction factor which

depends on the cross-sectional shape, G is the shear modulus, and ω is the frequency. The shear correction factor, k', is set to 0.833 as suggested for a rectangular beam by Timoshenko [30]. The radius of gyration for uncoupled keel bending is $H/2\sqrt{3}$, where H is the height of the keel (3 inches).

Figure 6-1 shows a comparison of the measured dispersion relations from the keel-end array with the theoretical dispersion relation for bending of the uncoupled keel. The new dispersion curve observed in the data does not line up with the dispersion curve for the uncoupled keel. However, due to the coupling between the keel and the shell, the keel bending wave in the coupled system can be expected to be different than that for the uncoupled system.

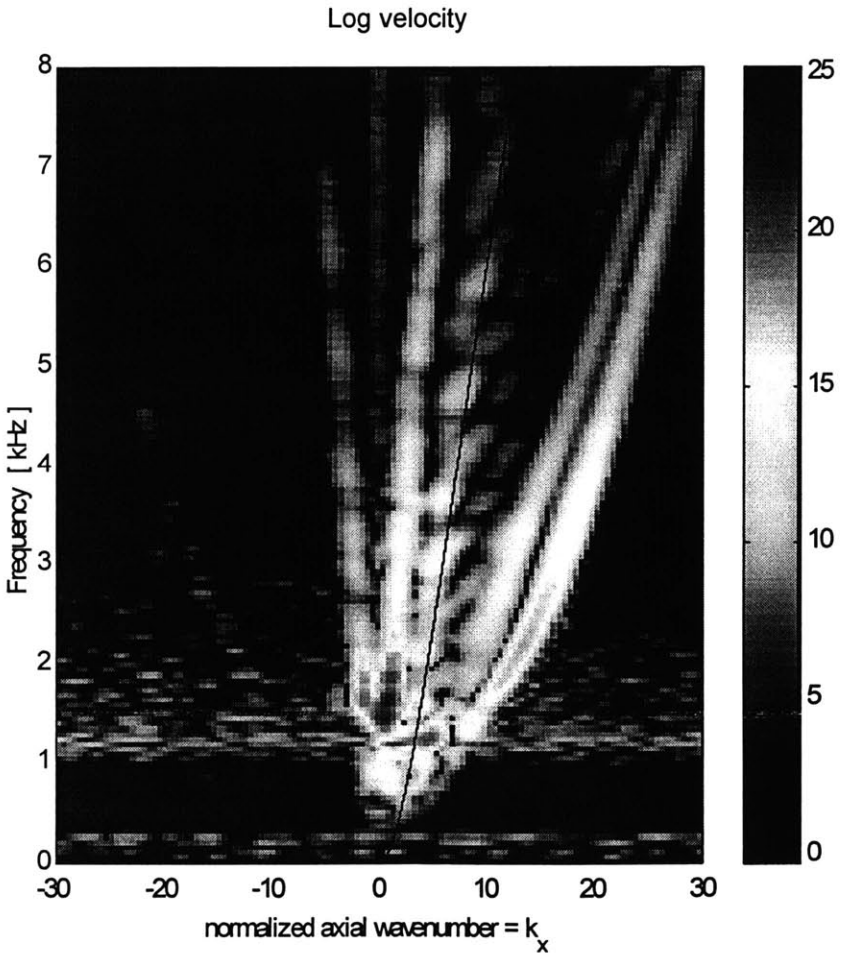

Figure 6-1: Dispersion curve for uncoupled keel bending overlaid on the wavenumber frequency transform measured on the end of the shell with a keel

A theoretical model for bending waves of the coupled keel-shell system which involve primarily bending of the keel in the stiff direction can be developed. Although an exact theoretical development is beyond the scope of the work in this thesis, an approximate theory was derived.

The addition of the shell to one edge of the keel causes the neutral axis for bending of the keel to shift away from the center of the keel. The extent of the shift depends on the extensional stiffness of the shell. For low extensional stiffness, the shift in the neutral axis will be small. However, for high stiffness the neutral axis will shift to a location near the edge of the keel.

The bending radius of gyration is expected to be in the range

$$\frac{H}{2\sqrt{3}} \leq \kappa \leq \frac{H}{\sqrt{3}}$$

For an approximate theory the bending radius of gyration was adjusted to best fit the observed dispersion curve. The best fit was found using a value of $\kappa = H/1.4\sqrt{3}$.

Figure 6-2 shows the theoretical estimate of the dispersion curve for the coupled keel bending wave overlaid on the measured wavenumber-frequency data.

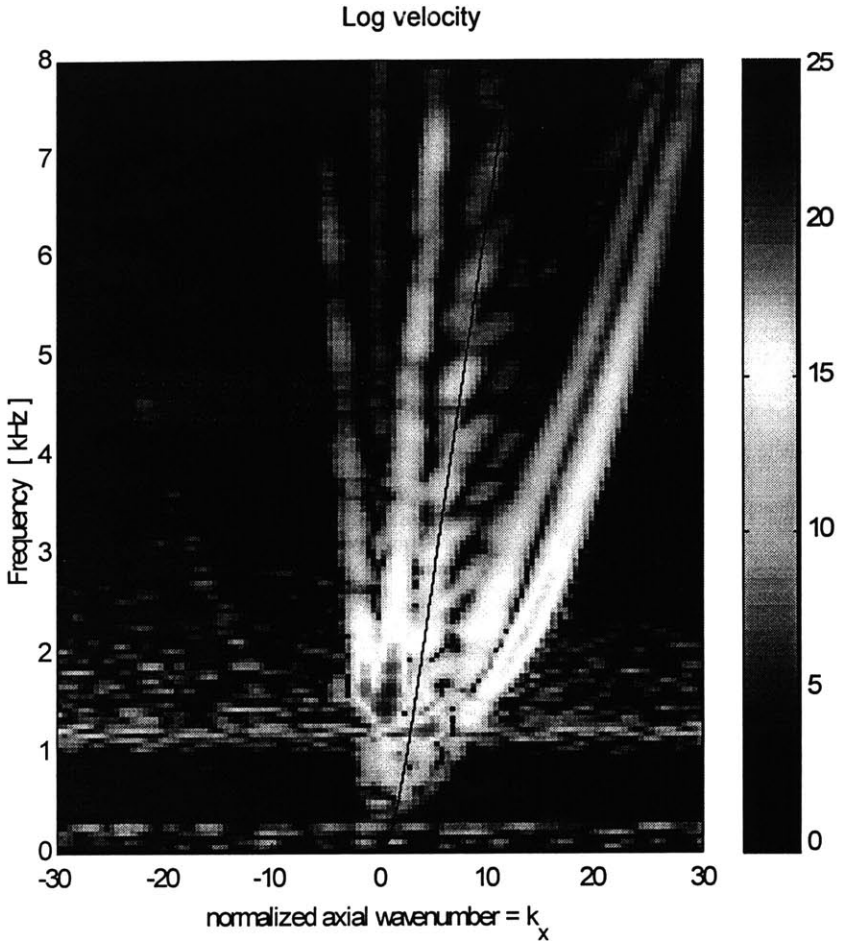

Figure 6-2: Dispersion curve of the keel wave overlaid on the wavenumber frequency transform measured on the end of the shell with a keel.

6.2.1 Excitation of the keel wave

The keel is not present at the source array. Thus, the keel wave is not directly excited by the sources. Excitation of the keel wave occurs primarily at the start of the keel, where the addition of the keel creates an axial discontinuity. Wave scattering at this discontinuity provides excitation of the keel wave. Figure 6-3 shows the scattering of the incident waves at the start of the keel.

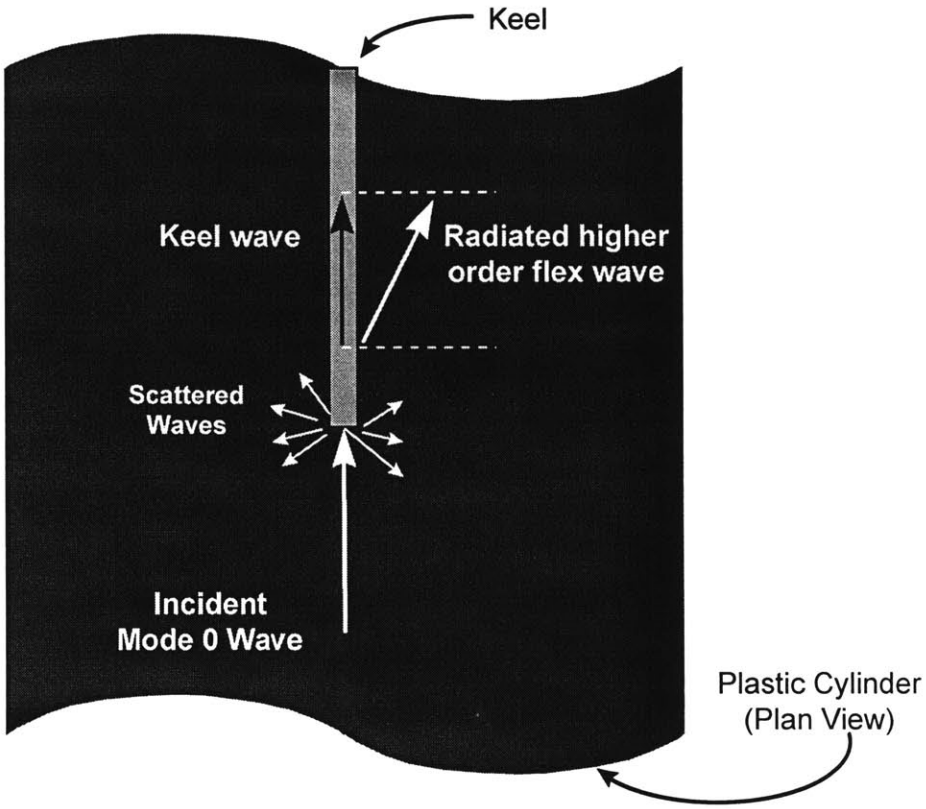

Figure 6-3: Wave scattering at the keel

The dispersion relation for the keel wave shows that the axial wavenumbers of the keel wave do not match those of the n=0 compressional wave in the coupled system. Thus, coupling of these two wave types along the keel is not expected.

The axial wavenumbers for the n=0 and n=12 flexural waves do not match the axial wavenumber of the keel wave over most of the frequency range. However, at selected frequencies axial wavenumber matching does occur. At these frequencies, the keel wave will be excited by both wave scattering at the start of the keel and by coupling to the shell flexural waves along the entire length of the keel.

Excitation of the keel wave by wave scattering at the start of the keel could have been eliminated by extending the keel. However, the keel wave would then have been directly excited by the source array.

6.2.2 Coupling between the keel wave and higher order flexural waves

The keel wave will be coupled to higher order flexural waves in the shell when the axial wavenumber of these waves (the trace wavenumber) matches the axial wavenumber of the keel wave. Figure 6-4 shows the dispersion curves for the higher order flexural waves in the shell and the keel wave. The figure plots the axial trace wavenumber of each wave versus frequency. Coupling is expected at the frequencies where these wavenumbers match. The coupling points are indicated by small circles in Figure 6-4.

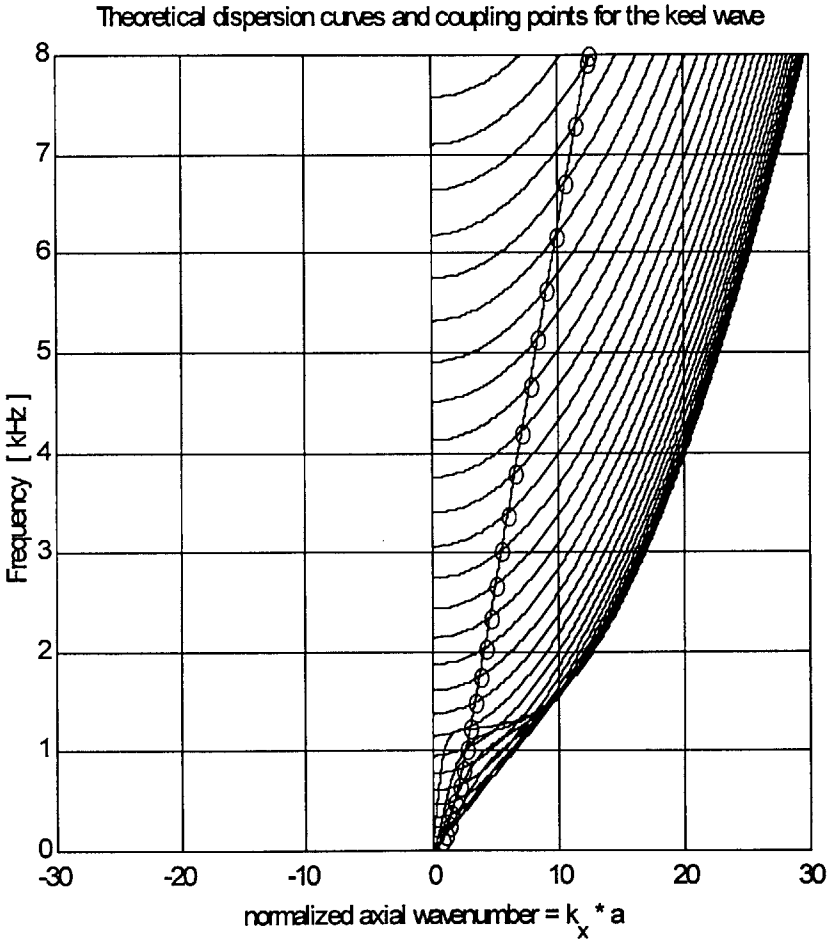

Figure 6-4: Coupling points for the keel wave

The axial array data on the keel end was measured along an axial line 90 degrees away from the keel. Thus, motion of the keel (ie the keel wave) is not directly measured. Rather, the response of higher order flexural waves in the shell which are trace-matched to the keel wave are measured. Fluctuation in the amplitude of the array data along the

keel wave dispersion curve is expected from this effect. High response amplitudes are expected at frequencies where matching between the keel wavenumber and the trace wavenumber of a shell flexural wave occurs. Low amplitudes are expected at frequencies where no match occurs.

Figure 6-5 shows an overlay of the trace matching points with the measured data. High response amplitudes are observed at these points, which supports the above hypothesis.

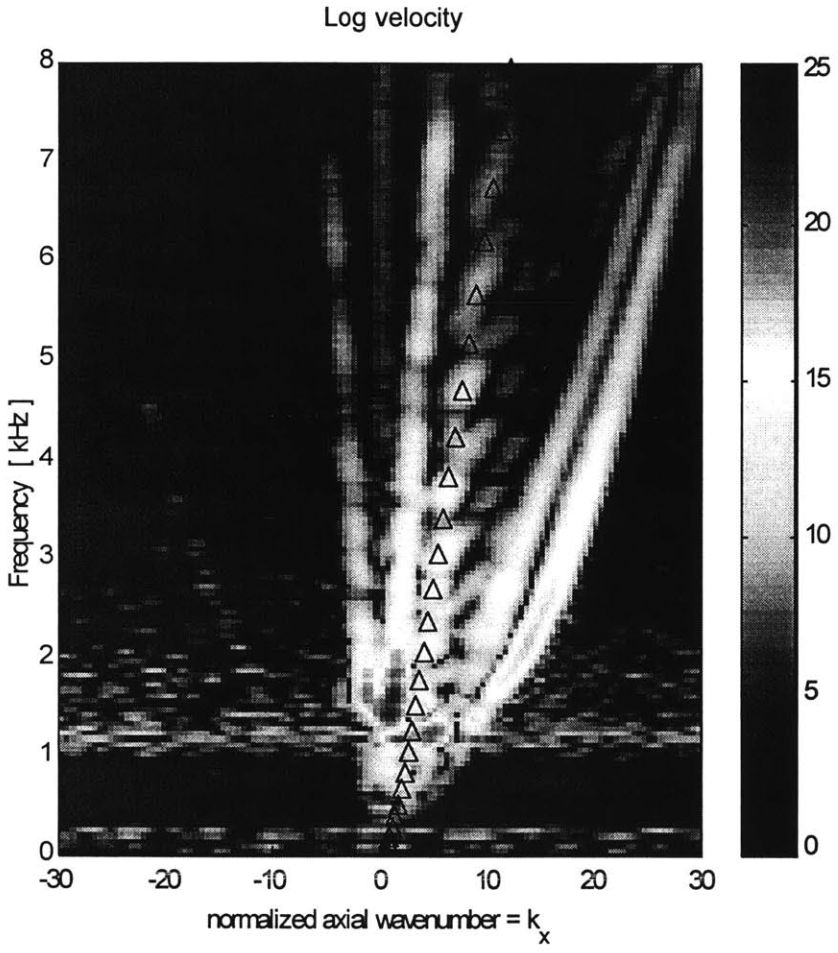

Figure 6-5: Keel wave coupling points overlaid on the keel end longitudinal array data

6.3 Coupling of shell membrane waves to flexural waves

Addition of the keel introduces a circumferential discontinuity which causes the shell waves to be coupled. Coupling occurs along the length of the keel when the trace axial wavenumbers are matched. Coupling also occurs at the ends of the keel where wave scattering occurs. These two mechanisms are illustrated in Figure 6-3. Coupling at the ends of the keel causes energy to be transferred from the incident membrane compressional and flexural waves to other wave types.

Since the start of the keel presents a point discontinuity to the incident waves, all circumferential wave types will be excited. However, only some of the waves will propagate down the shell. Waves whose wavenumber goes to zero at a frequency above the frequency of excitation will be evanescent and will decay exponentially with distance away from the start of the keel.

Coupling along the length of the keel causes energy to be transferred from the incident compressional and flexural waves to higher order flexural waves. However, only flexural waves with trace wavenumbers in the axial direction that match the axial wavenumber of the incident waves will be excited. This trace matching only occurs at selected frequencies which will be determined in the section below.

6.3.1 Determination of the coupling frequencies

The points at which the mode 0 compressional wave couples to higher order flexural waves were calculated using the theoretical dispersion relations formulated by Borgiotti and Rosen and programmed into a MATLAB program, 'skbar2.m' by Hayner. Waves travelling down the axis of the shell can only couple to other waves with the same axial wavenumber and frequency. Although the coupling by the keel is expected to shift the shell dispersion curves, the measured longitudinal array data shows that this effect is small. Thus, the frequencies at which coupling can occur can be approximated from the frequencies at which the dispersion curves for any two waves in the homogeneous shell cross. Figure 6-6 shows the theoretical dispersion curves for the mode 0 compressional wave and the modes 0-29 flexural waves. Flexural modes n=12 and n=28 are labeled. The intersections between the sharp v-shape of the mode 0 compressional wave and

the u-shaped flexural modes are the coupling points. They are marked by small circles. The lower order flexural waves do not couple to the mode 0 compressional wave since there is no point at which their dispersion curves cross. The mode 0 compressional wave begins to propagate at approximately 1400 Hertz. The mode 12 flexural wave begins to propagate at a slightly higher frequency. The mode 12 flexural wave is the lowest flexural wave which couples to the mode 0 compressional wave. All flexural waves with modal order higher than 12 also couple to the mode 0 compressional wave.

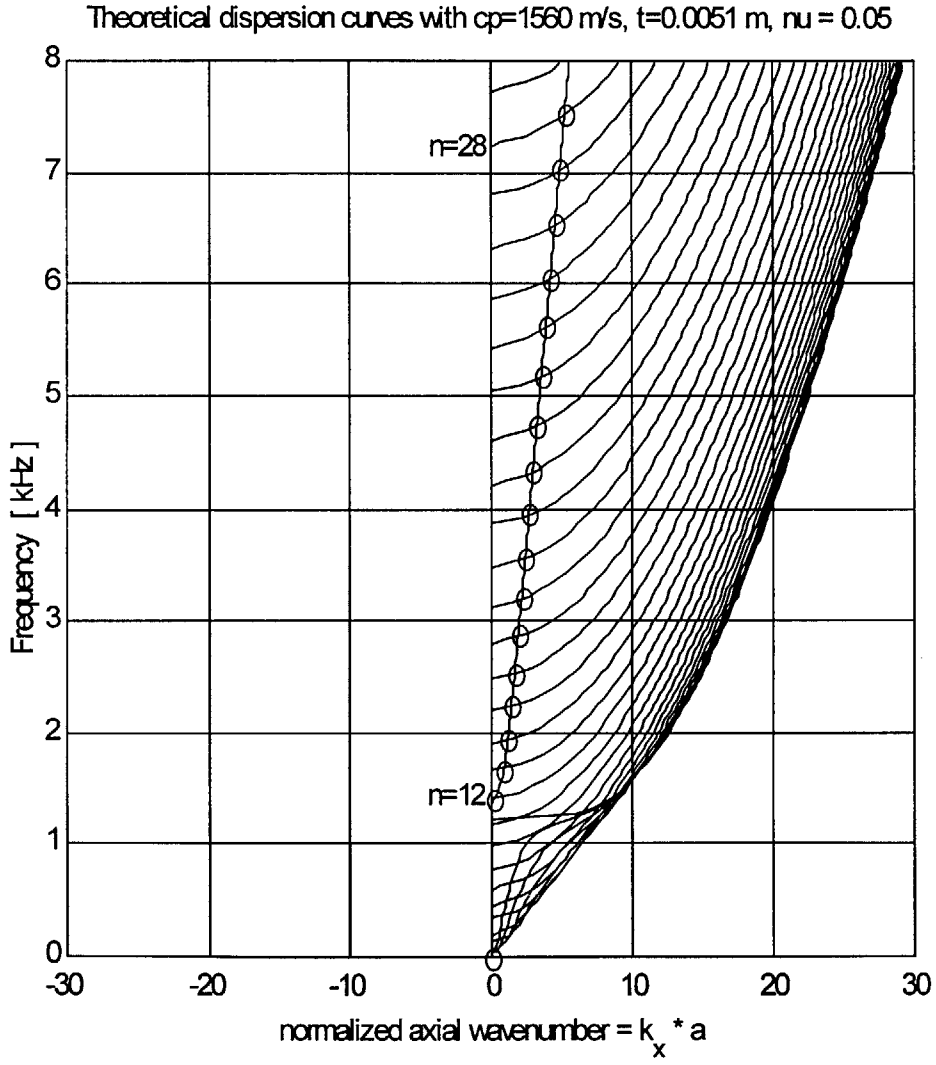

Figure 6-6: Theoretical dispersion curves and wave coupling points

Hayner's program, 'skbar2.m', calculates the theoretical value of the normalized axial wavenumber, $k_x a$, at a user-specified set of frequencies. In order to facilitate the comparison between theory and experimental data, $k_x a$ was calculated at each multiple of 10 Hertz up to 8000 Hertz. Figure 6-7 shows the points at which the theoretical values were calculated. Because of the difference in slopes, the points defining the dispersion curve of the compressional wave are much more closely spaced than the points defining the flexural curves. This effect is particularly noticeable at low wavenumbers.

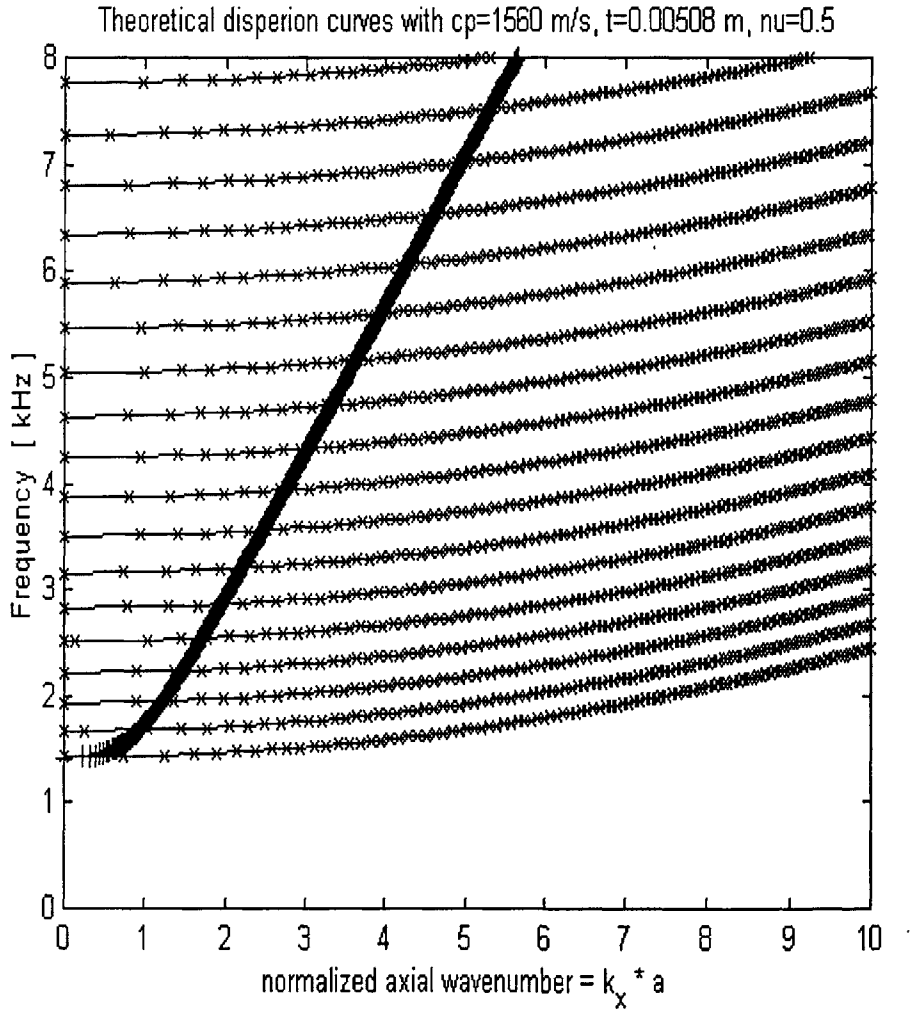

Figure 6-7: Calculation points for the theoretical dispersion curves.

The coupling points between the mode 0 compressional curve and each flexural curve were calculated by finding the least-squared difference between the $k_x a$ values for the

two curves at each frequency. For each flexural curve, modes 12 through 28, a coupling frequency was identified at which the flexural curve crossed the mode 0 compressional curve. Associated with that coupling frequency is the $k_x a$ value of the crossing. Since the compressional wave is more finely defined along the frequency axis than the flexural wave, the coupling $k_x a$ value was defined as the $k_x a$ value of the compressional wave at the coupling frequency.

Each coupling point is thus defined by three parameters: frequency, normalized axial wavenumber, $k_x a$, and the modal order of the flexural wave. The modal order of the waves is directly related to their normalized circumferential wavenumber, $k_\theta a$. Figure 6-8 shows the coupling points plotted as frequency versus modal order, $n = k_\theta a$. The coupling point between mode 0 compressional and mode 12 flexural occurs near 1400 Hertz. Higher order flexural modes couple to the mode 0 compressional wave at higher frequencies.

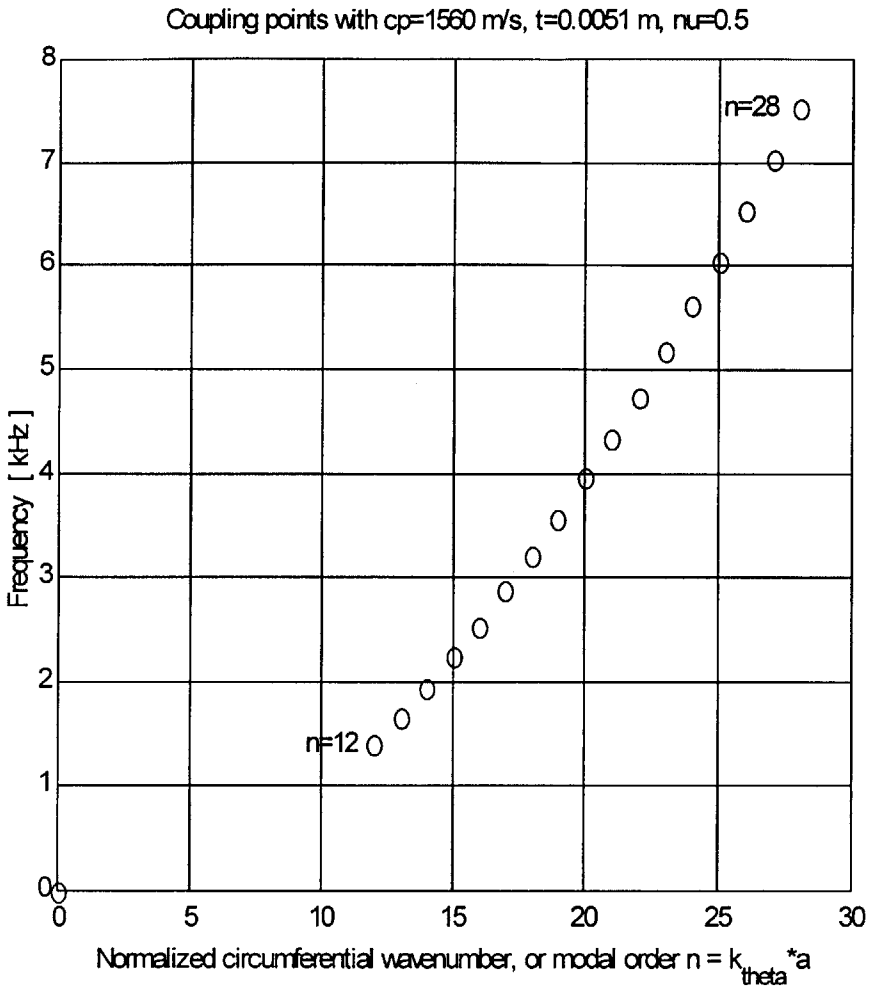

Figure 6-8: Coupling points plotted versus normalized circumferential wavenumber.

The coupling points are accurate only to within the frequency and wavenumber resolutions of the calculation process. The frequency resolution of the theoretical dispersion curves was defined to be $\Delta f = 10$ Hertz. A coupling point was calculated for each modal order (or normalized circumferential wavenumber), $n = k_\theta a$, so of course, $\Delta n = 1$. The resolution along the longitudinal wavenumber axis, $\Delta k_x a$, is not constant. It is a function of the $k_x a$ spacing between points on the theoretical dispersion curve for the mode 0 compressional wave. Near the ring frequency (where the mode 0 compressional wave begins to propagate), the resolution is a maximum of $\Delta k_x a_{max} = 0.0944$, but it decreases with increasing frequency to a minimum of $\Delta k_x a_{min} = 0.0071$.

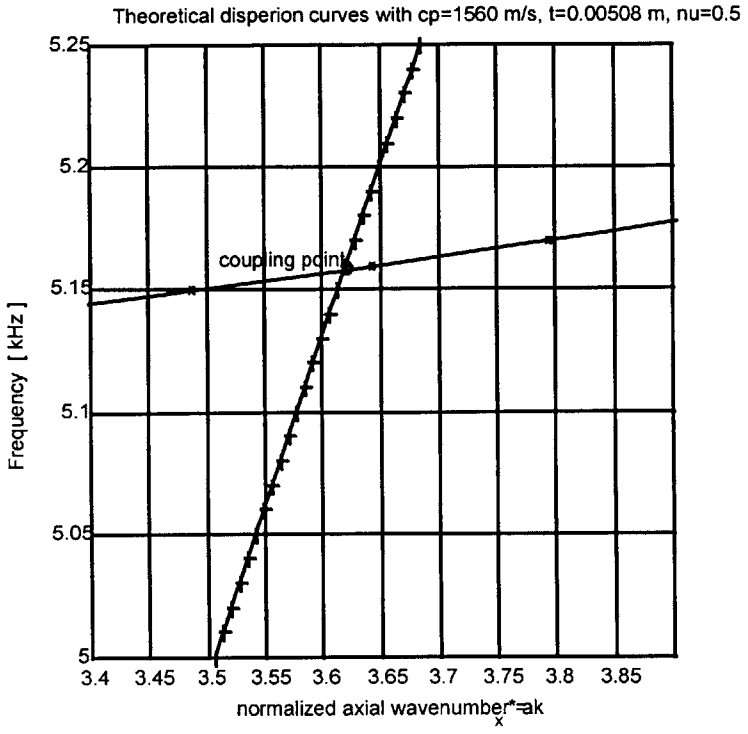

Figure 6-9: Frequency and wavenumber accuracy of the coupling points

The points at which the mode 0 flexural wave couples to higher order flexural waves and the points at which the keel wave couples to higher order flexural waves were calculated in the same way. The coupling points for the mode 0 flexural wave are shown in Figures 6-10 and 6-11, and the coupling points for the keel wave are shown in Figures 6-12 and 6-13.

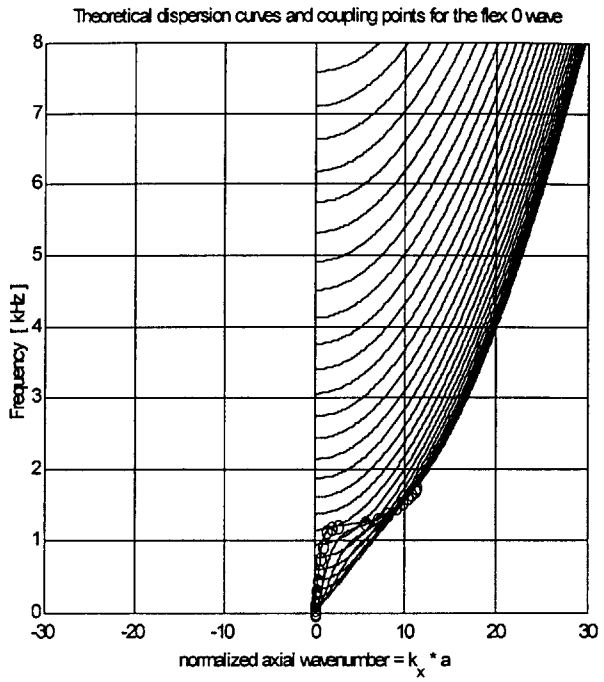

Figure 6-10: Axial wavenumber versus frequency for the coupling points between the mode 0 flexural wave and higher order flexural waves

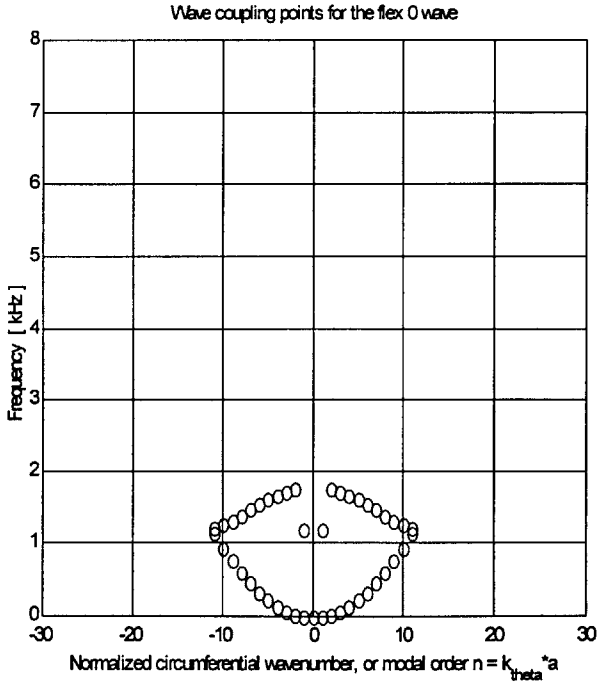

Figure 6-11: Circumferential wavenumber versus frequency for the coupling points between the mode 0 flexural wave and higher order flexural waves

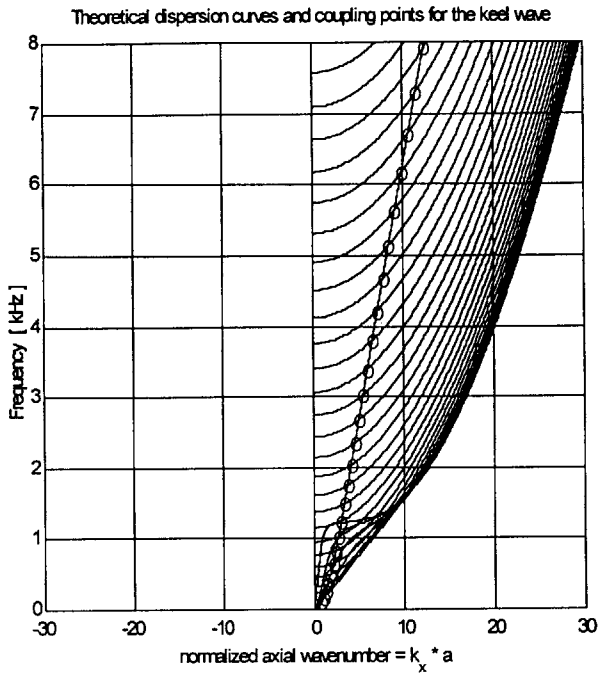

Figure 6-12: Axial wavenumber versus frequency for the coupling points between the keel wave and higher order flexural waves

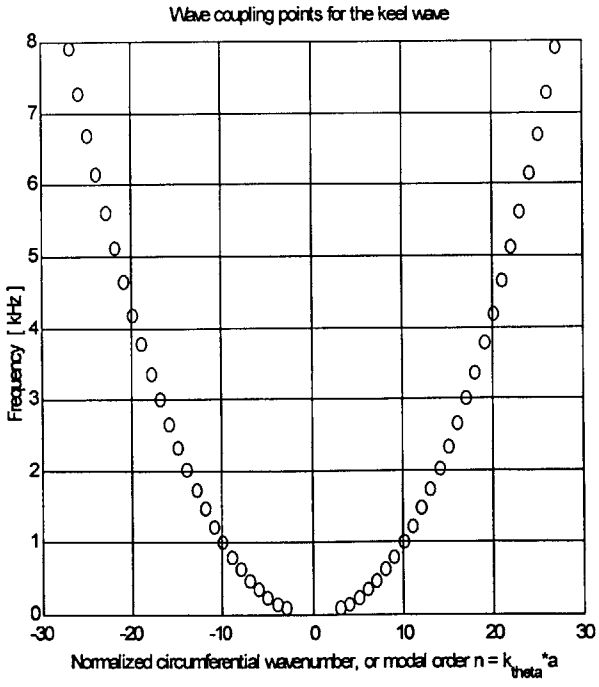

Figure 6-13: Circumferential wavenumber versus frequency for the coupling points between the keel wave and higher order flexural waves

7. CIRCUMFERENTIAL ARRAY MEASUREMENTS

When the equations of motion for an infinite cylindrical shell are written, they are separated into modes in the circumferential direction and waves in the longitudinal direction. Thus we can talk about mode 0 waves travelling longitudinally down the shell. The separated equations of motion can be written in the form of longitudinal dispersion relations, relating the frequency to the axial (longitudinal) wavenumber for each modal order and for each wave type. The longitudinal wavenumber can be measured experimentally using a longitudinal array. Data from the longitudinal array can be spatially transformed to obtain a measurement of the dispersion curves. Information on the modal order of the waves, however, is not contained in the longitudinal data.

Circumferential array measurements provide information on the circumferential wavenumber of the measured waves. The circumferential wavenumber corresponds directly to the circumferential modal order of the waves. This information is necessary for identifying the modal order of the waves traveling on the shell.

7.1 Test procedure for the circumferential array measurements

The test shell was suspended horizontally from two ropes which ran through pulleys attached to a wooden frame. Transfer functions were measured between the radial velocity of the outer surface of the shell and the broad-band random input signal.

7.1.1 Input to the source array

For the plain end circumferential tests, a broad-band white noise input signal of 5 Volts rms was passed through a Frequency Devices filter which applied a low-pass 8 pole Butterworth filter with a cut-off frequency of 8 kHz and a gain of 6 dB. Since the source signal power was concentrated in the lower frequencies, and since the response of the shell below the ring frequency was not of interest, a 500 Hz high-pass filter with a gain of 10 dB was also applied to the input signal. The signal was then amplified by a Wilcoxon PA7D power amplifier with a gain of 13 and a Wilcoxon N9 impedance

transformer with a gain of 5. The source signal for the plain end circumferential array measurements was thus band-limited to 500 Hz - 8 kHz with a total gain of about 52 dB. The input signal was split twelve ways and fed to the twelve transducers in the source array. Figure 7-1 shows typical laser data overlaying system noise data. The signal is clearly above the noise level over the entire input frequency range of 500 Hz and 8 kHz.

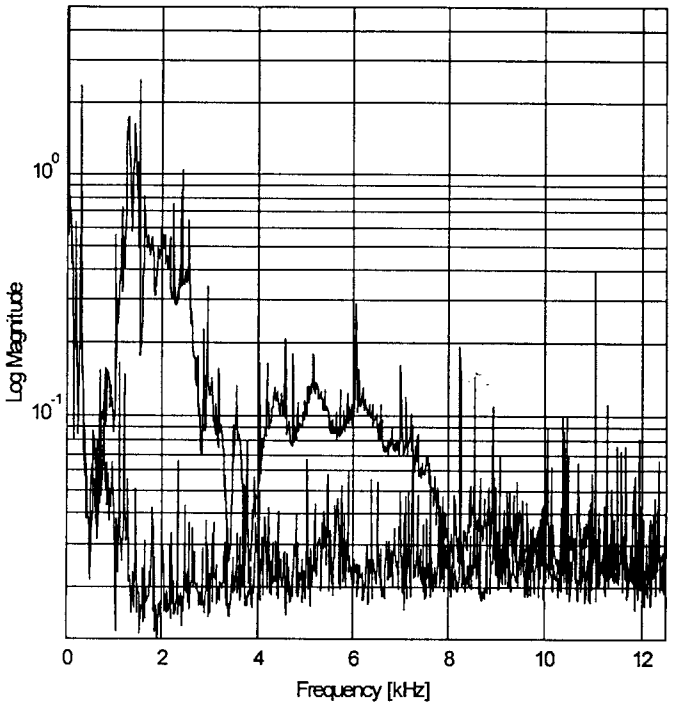

Figure 7-1: Signal vs. noise for the circumferential array measurements

The input for the keel end circumferential tests was slightly different. The broad-band white noise input signal was 2.5 Volts rms instead of 5 Volts rms. To compensate for this, the gain on the low-pass filter was boosted to 12 dB.

7.1.2 Assembling the data

The data collection for the circumferential arrays was conceptually the same as the data collection for the longitudinal arrays, but there were some significant differences. First, a commercial analyzer was used to collect and save the data instead of the Bondaryk's ldv program. Second, the cylinder had to be rotated by hand to each of the 125

measurement locations on the circumferential array. Third, the gain settings on some of the filters were higher. (See Appendix B for details.)

Data was collected at 125 points, spaced 1 centimeter apart to span almost 360 degrees around the cylinder. At each point, the radial velocity of the outer surface of the shell was measured with the laser. The sensitivity of the laser was set to 1 millimeter per second per Volt, the most sensitive setting. The laser lens was 17 inches from the shell and reflective tape was mounted at the measurement points to improve reflection of the laser beam. The laser remained fixed throughout the circumferential measurements, and the shell was rotated from point to point.

The circumferential test data was collected with the SRS frequency analyzer. For each point in the array, the input signal and the laser output signal were processed with 100 averages for 801 linearly-spaced frequencies between 0 and 12.5 kHz. For the plain end tests, the transfer function calculated by the analyzer were saved. For the keel end tests, the input and output autospectra and cross-spectrum were saved. The data were translated into MATLAB format, where the transfer functions were calculated by dividing the cross-spectrum by the input autospectrum. (See Appendix B for details.)

7.1.3 Calibrations

The input to the sources for the circumferential array tests was measured via a transfer function between the SRS analyzer's source signal and the output of the Wilcoxon impedance matching network, which is split twelve ways and fed into the twelve piezo-ceramic sources. The calibration was performed with a reduced voltage input of 0.2 volts. The transfer function shows the cumulative effect of the filters and amplifiers used to shape the signal before sending it to the sources.

Figure 7-2 shows the input calibration for the plain end circumferential array tests. The data is quite noisy because of the form of the transfer function (See Appendix B). The signal is flat between about 700 Hertz and 6 kHz with a linear gain of about 455 (53 dB).

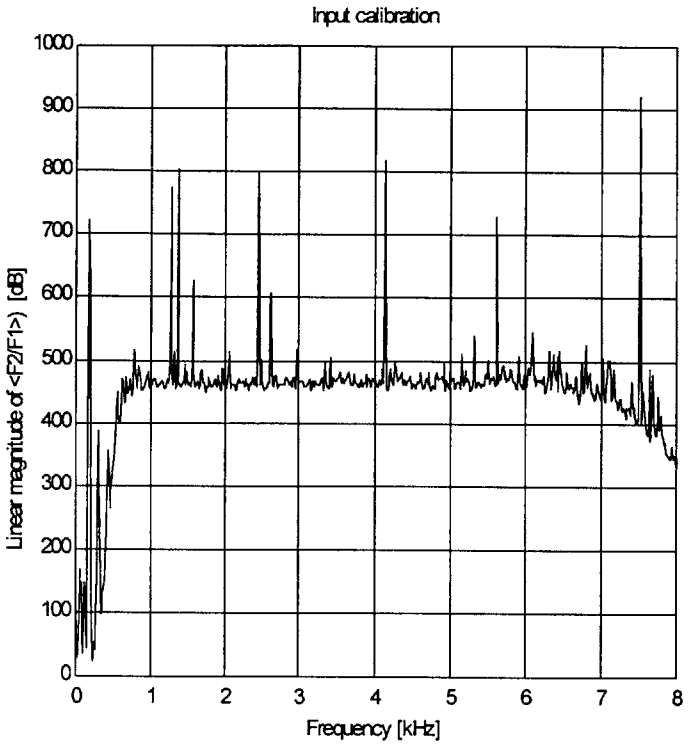

Figure 7-2: Input calibration for the plain end circumferential array tests.

Figure 7-3 shows the input calibration for the keel end circumferential array tests. At the high frequency end, the signal is flat up to 6 kHz, then drops off to 3 dB down at 8 kHz. In the low frequency range, the signal is flat above about 700 Hertz and 3 dB down at 500 Hertz. The total linear gain in the flat region is 910(59 dB). This is twice the gain used during the plain end measurements. However, the source signal voltage for the keel end measurements was half the voltage for the plain end measurements. Thus, the input level to the sources was the same during the two sets of measurements.

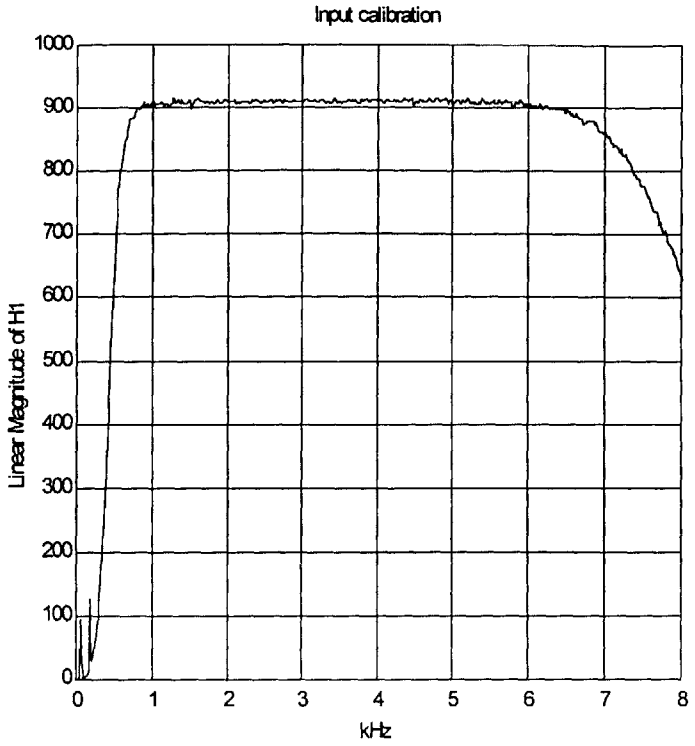

Figure 7-3: Input calibration for the keel end circumferential array tests

The output from the laser velocimeter was passed through various filters and amplifiers before going into the frequency analyzer for collection and processing. The cumulative effect of these filters and amplifiers is shown by the 'output transfer functions'. The 'input' for these transfer functions was a broad band white noise signal generated by the SRS frequency analyzer, which was used in place of an actual velocity signal from the laser.

Figure 7-4 shows the output transfer function for the plain end circumferential array. Again, the data is quite noisy because of the form of the transfer function (See Appendix B). The signal is flat between about 200 Hertz and 8 kHz with a linear gain of about 93 (40 dB).

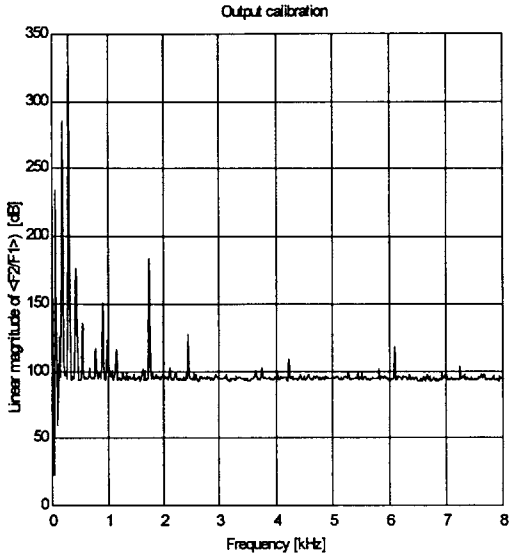

Figure 7-4: Output calibration for the plain end circumferential array test

Figure 7-5 shows the output transfer function for the keel end circumferential array. It is basically flat between 200 Hz and 8 kHz with drop-offs to 3 dB down at 100 Hz and 8 kHz respectively. The total linear gain in the flat region is 93 (40 dB).

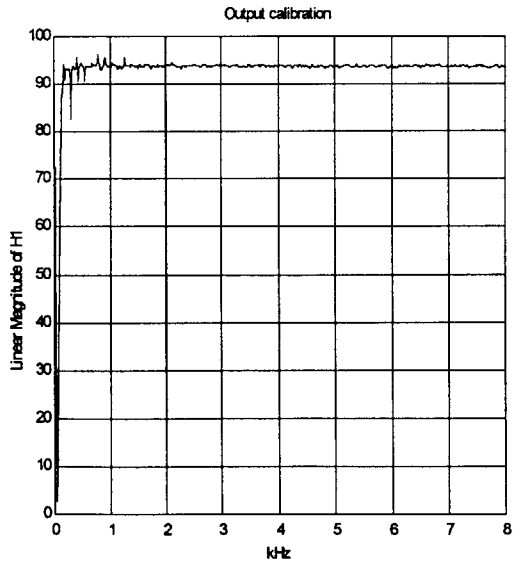

Figure 7-5: Output calibration for the keel end circumferential array test

7.2 Plain end circumferential array results

Figure 7-6 shows the wavenumber-frequency transform of the plain end circumferential array data. The transform shows the normalized circumferential wavenumber, $k_\theta a$, versus frequency. The circumferential wavenumber corresponds directly to the circumferential modal order of the waves.

For a homogeneous circular cylinder (without a keel), the circumferential modes can be expressed in terms of sin and cosine mode shapes, $\sin(n\theta)$ and $\cos(n\theta)$, where θ is the circumferential angle from 0 - 2π radians and n is the mode number. The mode number and circumferential wavenumber are related, $n = k_\theta * a$.

The longitudinal array data for the plain end of the shell (Figure 5-4) showed response along the dispersion curves of the three directly excited waves: mode 0 compressional, mode 0 flexural and mode 12 flexural. The circumferential array data shows the modal order associated with all these waves. Strong response is seen at $k_\theta a = 0$, corresponding to the mode 0 compressional and flexural waves. Response is also clearly seen along lines at $k_\theta a = +12$ and -12, corresponding to the mode 12 flexural wave.

The absence of strong response at other values of $k_\theta a$ indicates that no other modes were excited. This is an important finding, since it shows that the test setup was functioning as designed. The following three conclusions can be drawn from this measurement. 1) The source array was working as designed to excite only mode 0 and 12 waves on the shell. 2) The plastic test shell is sufficiently homogeneous to support single order waves without coupling to higher order modes. 3) There is no significant coupling to higher order modes at the ends of the shell or at the support ropes. These conclusions are for the plastic test shell, which has high damping, and may not be applicable to a test shell with lower damping.

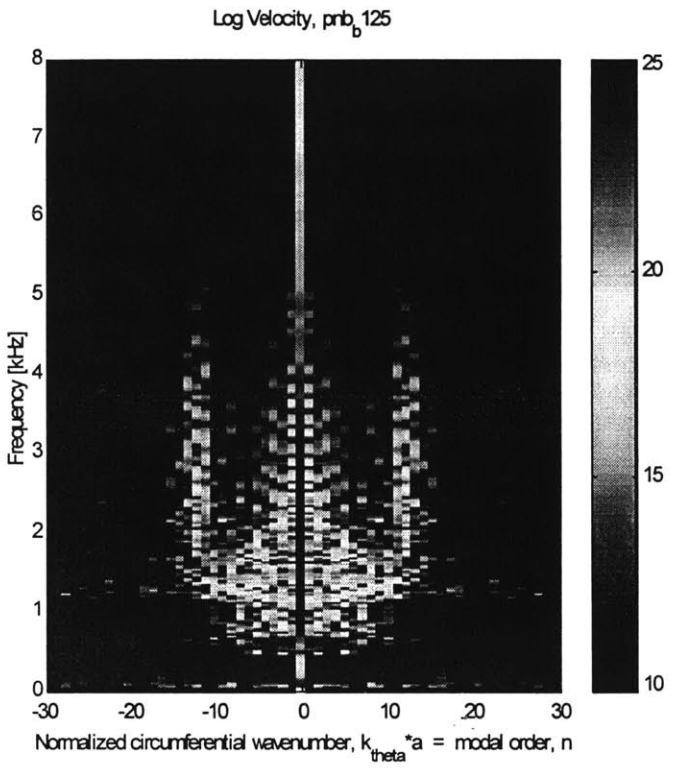

Figure 7-6: Circumferential array data for the plain end of the shell

7.3 Keel end circumferential array results

Figure 7-7 shows the wavenumber-frequency transform of the keel end circumferential array data. The transform shows the normalized circumferential wavenumber, $k_\theta a$, versus frequency. The circumferential wavenumber corresponds directly to the circumferential modal order of the waves.

For a homogeneous circular cylinder (without a keel), the circumferential modes can be expressed in terms of sin and cosine mode shapes, $\sin(n\theta)$ and $\cos(n\theta)$, where θ is the circumferential angle from 0 - 2π radians and n is the mode number. The mode number and circumferential wavenumber are related, $n = k_\theta * a$.

Addition of the keel changes the expected mode shapes. A wave traveling axially down the shell will still have an associated circumferential mode shape, but it may not be sinusoidal. However, the mode shape can be expressed as a sum of sinusoidal components, $A_1\sin(n_1\theta) + A_2\sin(n_2\theta)$ + etc. where n_1 and n_2 are the 'modal orders' of each component. In other words, the new mode shapes can be expressed as a summation of the old mode shapes.

The longitudinal array data for the keel end of the shell (Figure 5-26) showed response along 5 lines. Four of the response lines lay along the dispersion curves of the mode 0 compressional, mode 0 flexural and mode 12 waves for an uncoupled shell (without a keel). The fifth response 'line' was a sequence of high response points that laid along the dispersion curve of the keel wave. The circumferential array data shows the modal order associated with all these waves.

A strong response line is seen at $k_\theta a = 0$, which corresponds to a modal order of n = 0. Although the keel changes the 'mode 0' mode shapes, the dominant modal order of the 'mode 0' waves on the coupled shell is still expected to be n=0. Strong lines of response are also seen at $k_\theta a = +12$ and -12. These lines indicate the dominant modal order of the 'mode 12' flexural wave on the coupled shell. The new and exciting feature in Figure 7-7 is the presence of diagonal lines with higher modal orders. The diagonal lines extend over the whole excited frequency range, 500 Hz - 8 kHz, with modal order varying from about n = 7 to n = 30. The next section shows that the diagonal lines

correspond to the higher order flexural waves excited through trace-matched coupling with the mode 0 flexural and compressional waves and the keel wave.

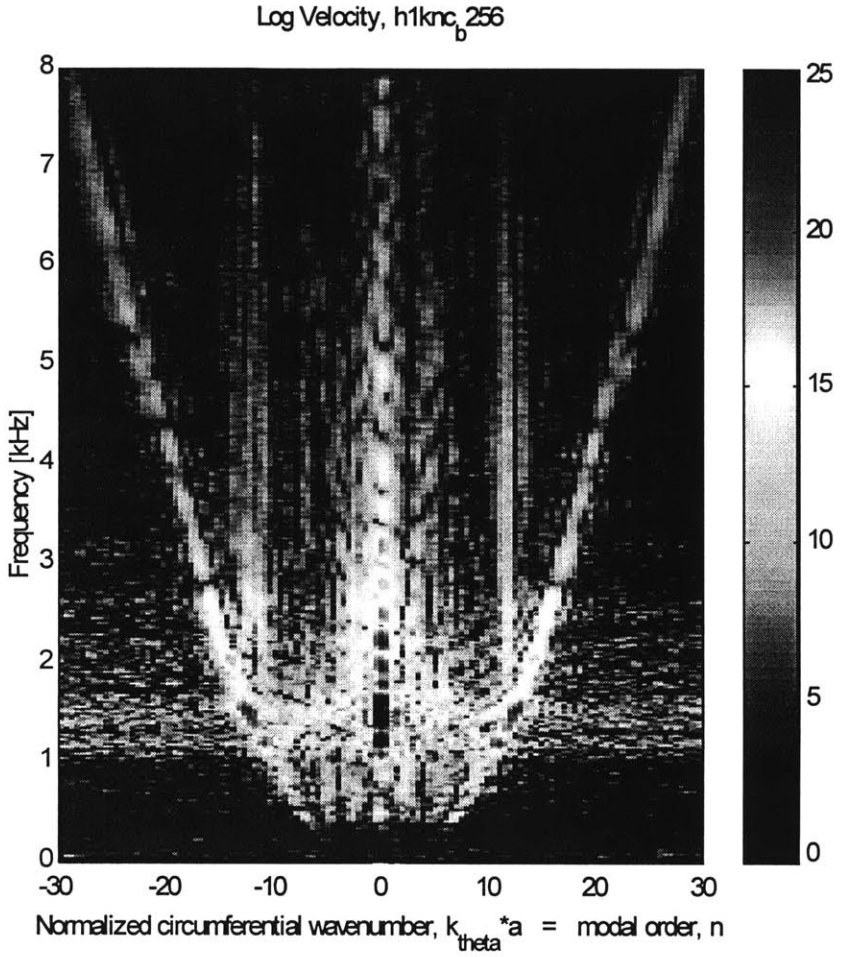

Figure 7-7: Circumferential array data for the end of the shell with a keel

7.3.1 Comparison with theory

The theoretical coupling points calculated in Section 6.3.1 (shown in Figures 6-6, 6-8, and 6-10 to 6-13) are each associated with a circumferential modal order, $n = k_\theta a$. Figure 7-8 shows the coupling points plotted as modal order versus frequency. The triangles are the coupling points between the keel wave and higher order flexural waves, the circles are the coupling points between the mode 0 compressional waves and higher order flexural waves, and the squares are the coupling points between the mode 0 flexural waves and higher order flexural waves. The keel wave coupling points and the compressional mode 0 coupling points are very close together at low frequencies, but spread apart at higher frequencies.

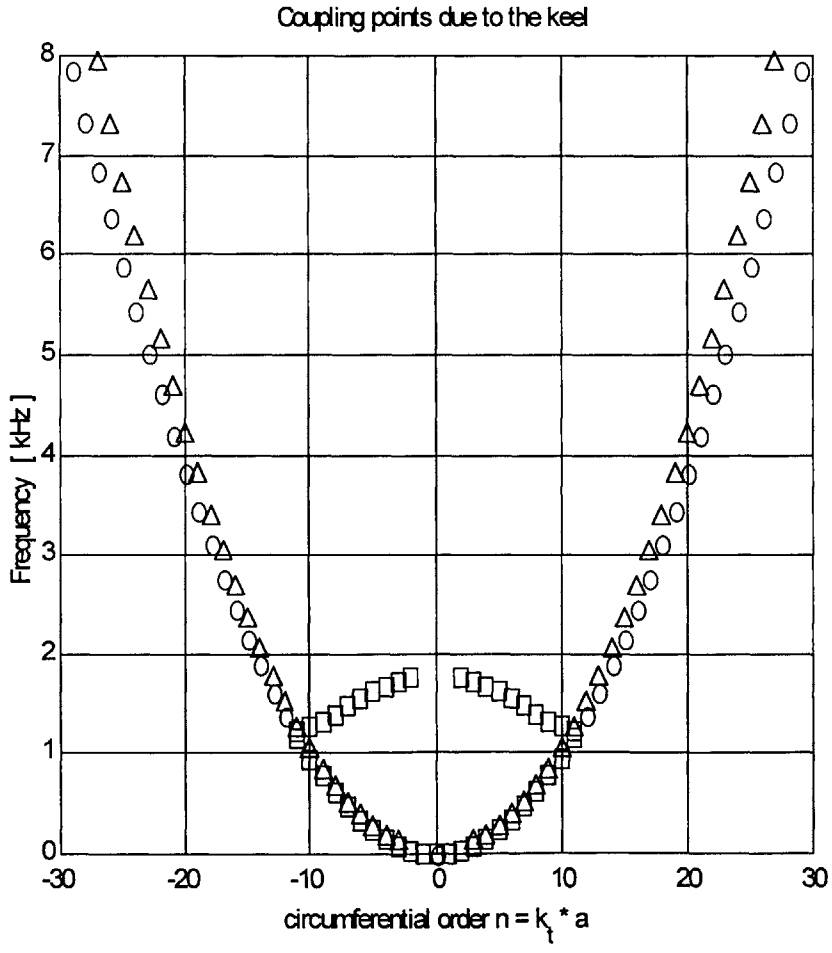

Figure 7-8: Theoretical coupling points plotted as modal order versus frequency

Figure 7-9 shows the coupling points (represented by lines) overlaid on the circumferential array data measured on the keel end of the shell. The theoretical coupling points clearly model the data quite well. The coupling points in the middle of the plot (at low wavenumbers and near the ring frequency) represent coupling between the flexural mode 0 wave and higher order flexural waves.

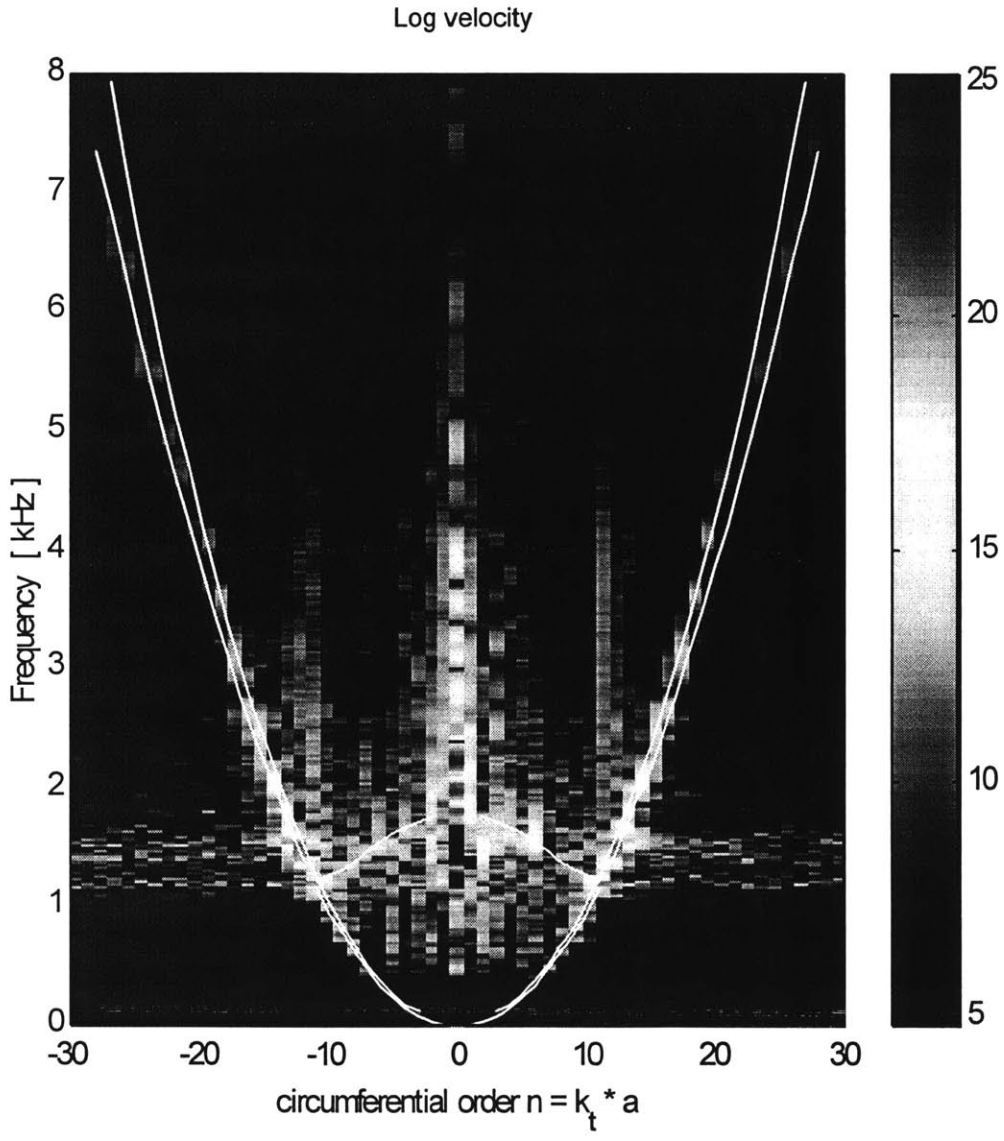

Figure 7-9: Coupling points due to the keel overlaid on the circumferential array data measured on the end of the shell with the keel

8. CONCLUSIONS AND FUTURE WORK

This thesis has shown that adding a longitudinal stiffener, or keel, to a circular cylindrical shell results in coupling between mode 0 waves and higher order flexural waves. Compressional and flexural mode 0 waves were excited on a plastic shell using a circumferential source array. The source array was located in the middle of a long shell, and a keel was attached to one end of the shell. Longitudinal and circumferential array measurements were taken on each end of the shell. Wavenumber frequency transforms were used to separate the data by modal order and wave type.

The addition of a keel to the cylindrical shell creates a new coupled system. The coupled system supports the waves associated with both of the coupling systems (keel and shell), but their dispersion relations will be different from the dispersion relations of the uncoupled systems. The significance of the changes depends on the frequency of interest and the strength of the coupling. In this thesis, changes in the dispersion relations of the shell waves due to coupling are not seen in the data. This result suggests that the changes are smaller than the resolution of the measurements.

The keel wave associated with bending of the keel was observed in the measured data. The axial velocity of this wave was found to be greater than the membrane shear wavespeed, but less than the bending wavespeed in the shell. A model was developed for the keel wave which showed that it was a coupled bending wave in the stiff direction of the keel. The neutral axis of the bending motion was shifted away from the neutral axis of the uncoupled keel. The other keel waves were not seen in the data.

The response of the keel wave is not directly measured in this thesis, since the longitudinal array measurements were taken along an axial line 90 degrees away from the keel. Rather, the measured response is that of the higher order flexural waves in the shell which are coupled to the shell wave through axial trace-matching. Trace-matching along the keel is shown to be a necessary geometric condition for wave coupling. However, the impedance ratio between the shell and the keel is also important in determining the efficiency of the coupling mechanism.

A plastic PVC test shell is used for the experiments in this thesis. The selection of this material was based in large part on cost. Fabrication of a steel cylinder without an axial seam was found to be prohibitively expensive. The use of plastic was critical in enabling the measurements conducted in this thesis, however. Because the compressional and shear wavespeeds are relatively slow in the plastic shell, membrane waves could be observed at lower frequencies in the plastic shell than in a steel shell. Also because of its relatively high damping, the reverberant build-up of wave amplitudes was not observed so that reflections from the ends of the shell did not interfere with the measurements. This enabled measurement of the direct and reflected wave amplitudes, which were used to calculate decay coefficients for the compressional mode 0 wave on the shell.

The conclusions drawn in this thesis are critically dependent on the relative levels of coupling and damping in the shell. On the plastic shell, the damping is relatively high. Coupling mechanisms have to be relatively strong to result in transfer of significant (i.e. measurable) amounts of energy between the coupled waves. High damping can mean that weak coupling factors do not have enough time to make a measurable change in wave energies. Conversely, on a shell with low damping, even weak coupling factors could result in significant energy transfer due to the high number of reflections and long travel path. In addition, other weak coupling factors might become significant on a shell with low damping. Coupling effects at the shell ends, at the support ropes, or due to slight bending or misshaping of the cylinder could become significant.

More in-depth modeling of the cylindrical shell with a keel could be used to determine specific design parameters for the keel. The models developed by Hayner [20] are suitable for analyzing either a shell with a complete homogeneous cross-section and a finite axial extent or a shell with a partial cross-section and an infinite axial length. Further development would be needed to accurately model a shell with a finite length keel. Further development would also be needed to model the wave coupling between an axial wave and higher-order circumferential waves.

In future experiments, the longitudinal wavenumber resolution should be increased by making the longitudinal array longer. This may enable distinction of changes in the shell dispersion relations due to the keel, and may enable better definition of the keel wave.

Better wavenumber resolution in the circumferential direction would also be helpful, since it might enable distinction between the compressional mode 0 coupling points and the keel wave coupling points, which are quite closely spaced in circumferential wavenumber. Another way to increase the distinction between the keel wave coupling points and the mode 0 compressional wave coupling points is to make the keel wave slower.

9. REFERENCES

1) Smith, T. L., "The Attenuation of Flexural Waves in Mass Loaded Beams," S. M. Thesis, MIT, May 1985.

2) Smith, Timothy L., Kodali Rao, and Ira Dyer, "Attenuation of Plate Flexural Waves by a Layer of Dynamic Absorbers," Noise Control Engineering Journal, Vol. **26**, March-April, 1986, pp. 56-60.

3) LePage, K. D., "The Attenuation of Flexural Waves in Asymmetrically Mass Loaded Beams," S. M. Thesis, MIT, 1986

4) Taylor, P. D., "Wave Propagation in a Beam Having Double Resonant Loading," S. M. Thesis, MIT.

5) Olivieri, L., "The Effect of Dynamic Absorbers on Longitudinal Wave Propagation in a Circular Rod," Master of Science Thesis, MIT, 1989.

6) Corrado, Charles, Rebecca Zavistoski, and Ira Dyer, "Coupled Wave Complexity in Structural Acoustics," ASME, Paper 90-WA/NCA-8, November, 1990.

7) Cremer, L., M. Heckl, and E. E. Ungar, Structure-Borne Sound, Springer-Verlag, New York, 1988, p 256.

8) Klyukin, I. I., "Attenuation of Flexural Waves in Rods and Plates by Means of Rsonance Vibrating Systems,," Sov. Phys. Acoust., **6**, 209-215, 1960.

9) Corrado, C. N., "Mid-frequency acoustic backscattering from finite cylindrical shells and the influence of helical membrane waves." Ph. D. thesis, Department of Ocean Engineering, MIT (1993).

10) Conti, M. and I. Dyer, "Scale model experiments on an internally loaded cylinder," Internal MIT Memorandum, June 1991.

11) Bondaryk, J., "Modal excitation and control of membrane waves on cylindrical shells," J. Acoust. Soc. Am., **103** (5), Pt. 1, 1998.

12) Rybak, S. A., "Waves in Random Media," N. N. Andreyev Acoustics Institute, Moscow, Russia.

13) Lin, Ching-Yu, "Pressure estimation of piezoelecctric rings embedded orthogonally in cylindrical shells," S. M. Thesis, MIT (1998).

14) Ricks, D., "Elastodynamic Modeling of Fluid-Loaded Cylindrical Shells with Multiple Layers and Internal Attachments," Ph. D. thesis, Department of Ocean Engineering, MIT (1994).

15) Guo, Y. P., "Sound scattering from an internally loaded cylindrical shell," J. Acoust. Soc. Am., **91** (2), 926-938 (1992).

16) Guo, Y. P., "Effects of structural joints on sound scattering," J. Acoust. Soc. Am., 93 (2), 857-863 (1993).

17) Guo, Y. P., "Sound scattering by bulkheads in cylindrical shells," J. Acoust. Soc. Am., **95** (5), 2550-2559 (1994).

18) Guo, Y. P., "Sound scattering from cylindrical shells with internal elastic plates," J. Acoust. Soc. Am., **93** (4), Pt. 1, 1936-1946 (1993).

19) Guo, Y. P., "Acoustic scattering from cylindrical shells with deck-type internal plate at oblique incidence," J. Acoust. Soc. Am., **99** (5), 2701-2713 (1996).

20) Hayner, M. A., "Wave-based finite element method applied to thick, in-vacuo, cylindrical shells with keel or bulkhead plate attachments at middle to high frequency," Ph. D. thesis, Department of Ocean Engineering, MIT (1998).

21) Klauson, A., G. Maze, and J. Metsaveer, "Acoustic scattering by submerged cylindrical shell stiffened by an internal lengthwise rib," J. Acoust. Soc. Am. 96, 1575-1581 (1994).

22) Borgiotti, G. V. and E. M. Rosen, "The state vector approach to the wave and power flow analysis of the forced vibrations of a cylindrical shell, part I: Infinite sylinders in vacuum." J. Acoust. Soc. Am. **91**, 911-925, 1992

23) Love, A. E. H., "The Small Free Vibrations and Deformations of a Thin Elastic Shell," Phil. Trans. Royal Soc. (London) series A, 179, pp. 491-549, 1888.

24) Lamb, H. "On the Deformation of an Elastic Shell," Proc. London Math. Soc., Vol. 21, pp. 119-146, 1891.

25) Leissa, A., Vibrations of Shells, American Institute of Physics, Woodbury, N.Y.,1993.

26) Donnell, L. H., "A Discussion of Thin Shell Theory," Proc. Fifth Intern. Congr. Appl. Mech., p. 66, 1938.

27) Mushtari, M., "Certain Generalizations of the Theory of Thin Shells," Izv. Fiz. Mat. Ob-va. Pri Kax. Un-te., Vol. 11, no. 8, 1938 (in Russian).

28) Junger, M. and D. Feit, Sound, Structures, and their Interaction, 2nd Edition, MIT Press, Cambridge, Massachusetts, 1986.

29) Mirsky, I. and G. Herrmann, "Nonaxially Symmetric Motions of Cylindrical Shells," J. Acoust. Soc. Am., Vol **29** (10), 1957.

30) Timoshenko, S., D. H. Young, and W. Weaver, Jr., Vibration Problems in Engineering, 4th Edition, John Wiley & Sons, Inc., New York, 1974, p 432.

31) Randall, R. B., Frequency Analysis, K. Larsen & Son A/S, Glostrup, Denmark, 1987 (for Bruel & Kjaer).

Appendix A: CYLINDRICAL SHELL THEORY

A-1 Cylindrical shell theory

The equations of motion for a thin-walled cylindrical shell have been a topic of interest for over 100 years [23,24]. Hundreds of papers have been published dealing with the basic equations of motion and various improved formulations [25]. In spite of the many choices, the relatively simple equations presented by Donnell [26] and Mushtari [27] continue to be used for many studies. Junger and Feit [28] have used these equations to study the scattering of acoustic waves incident on an empty cylindrical shell. Corrado [9] has used the Donnell-Mushtari equations to interpret the scattered acoustic field data for cylindrical shells representative of submarine structures with stiffeners, end caps, and internal structures.

Improvements to the basic Donnell-Mushtari equations typically focus on corrections for 1) lower order ($n \leq 2$) circumferential modes, and 2) thick shells and high frequencies, where transverse shear and rotary inertia corrections may be required. Both types of correction are important for the research in this thesis. The lower order membrane waves are important because they are significant contributors to scattering and radiation. Shear and rotary inertia are expected to be important in describing the high order bending waves, which are coupled to the membrane waves by the keel.

Many of the improvements to the basic shell equations are described by Leissa [25], but papers with improved shell theories continue to be published. Borgiotti and Rosen [22] studied vibration waves using a state vector formulation which included the effects of rotary inertia and transverse shear deformations. Ricks [14] used a direct global matrix technique to develop numerical models with the full three-dimensional elasticity equations. These models can be used as reference models to check the accuracy of simpler thin-shell theories. They can also be used to study the dynamic behavior of layered shells. Hayner [20] has used the two-dimensional thick shell theory of Herrmann-Mirsky [29] to develop a wave-based finite element method, WFEM. He has

validated this thick shell theory by comparing solutions with numerical results from a full three-dimensional elastic analysis.

The improved shell theories can provide greater accuracy, particularly for lower order circumferential waves, $n \leq 2$, and for high frequencies. Unfortunately, the greater complexity of these improved theories may cloud the physical insight that can be gained from a simpler theory. The work presented in this thesis is primarily experimental. Theory is used to gain a physical understanding of the measured data, so simplicity is important. It is worth studying the assumptions behind the simple Donnell-Mushtari equations and exploring ways in which these equations can be used to interpret the measured data. The more exact shell equations can be used if necessary to expand the range of applicability of this thesis.

The Donnell-Mushtari equations for a cylindrical shell are analogous to the Bernoulli-Euler equations for bending of a beam or flat plate [7]. They neglect the effects of rotary inertia and transverse shear deformations. For cylindrical shells, the assumptions associated with this simplification were introduced by Love [Reference 28, p216].

1. The shell thickness is small compared to the radius.
2. The displacement is small compared to the thickness.
3. The transverse normal stress acting on planes parallel to the shell's middle surface is negligible (no thickness deformation).
4. Sections of the shell normal to the middle surface remain so after deformation.

With these assumptions, the stress across the thickness of the shell wall can be expressed in terms of a displacement vector, [u] and its derivatives, where [u] represents the displacement of the centerline of the shell wall in the axial (u), circumferential (v) and radial (w) directions.

$$[u] = \begin{bmatrix} u \\ v \\ w \end{bmatrix}$$

More complex theories such as Herrmann-Mirsky [29], Borgiotti and Rosen [22] and Hayner [20] expand the displacement vector to include the mid-surface rotations (or transverse shearing angles) about the two in-plane axes. In these theories, the rotation angles are no longer assumed to equal the spatial derivative of the mid-surface radial displacement.

$$[u] = \begin{bmatrix} u \\ v \\ w \\ \varphi_\theta \\ \varphi_x \end{bmatrix}$$

In general, the homogeneous (unforced) equations of motion for a cylindrical shell can be written using a differential operator, [L].

$$[L][u] = [0]$$

The Donnell-Mushtari operator takes the form $[L_{D\text{-}M}]$ =

$$\begin{bmatrix} \left[\frac{\partial^2}{\partial x^2} + \frac{(1-\nu)}{2}\frac{1}{a^2}\frac{\partial^2}{\partial \theta^2} - \frac{1}{c_\ell^2}\frac{\partial^2}{\partial t^2}\right] & \left[\frac{(1+\nu)}{2}\frac{1}{a}\frac{\partial^2}{\partial x \partial \theta}\right] & \left[\nu\frac{1}{a}\frac{\partial}{\partial x}\right] \\ \left[\frac{(1+\nu)}{2}\frac{1}{a}\frac{\partial^2}{\partial x \partial \theta}\right] & \left[\frac{(1-\nu)}{2}\frac{\partial^2}{\partial x^2} + \frac{1}{a^2}\frac{\partial^2}{\partial \theta^2} - \frac{1}{c_\ell^2}\frac{\partial^2}{\partial t^2}\right] & \left[\frac{1}{a^2}\frac{\partial}{\partial \theta}\right] \\ \left[\nu\frac{1}{a}\frac{\partial}{\partial x}\right] & \left[\frac{1}{a^2}\frac{\partial}{\partial \theta}\right] & \left[\frac{1}{a^2} + \kappa^2\nabla^4 + \frac{1}{c_\ell^2}\frac{\partial^2}{\partial t^2}\right] \end{bmatrix}$$

where the x-coordinate runs along the axis of the shell, the θ-coordinate is angular about the x-axis, and a is the radius of the shell. The elastic modulus and density of the shell are defined in terms of the 2-D longitudinal wavespeed, or plate wavespeed, as defined by Cremer & Heckl (a condition of plane stress). [Reference 7, C_{LI}, p 86]

$$c_\ell = \sqrt{\frac{E}{\rho(1-\nu^2)}}$$

where E is Young's modulus, ρ is the material density, and ν is Poisson's ratio.

A-2 Description of model chosen for this research

Theoretical dispersion curves for the test shell were calculated using the state space equations presented by Borgiotti and Rosen [22]. These equations represent a theory similar to that of Herrmann-Mirsky [29], including the effects of rotary inertia and shear deformations. This theory was expected to model the test cylinder more accurately for high frequencies.

Borgiotti and Rosen [22] present a state vector approach that can be used to determine the dispersion relations for a thick-walled cylindrical shell. A state vector with ten elements is used for the thick shell. These include five "velocity" variables and five corresponding "force" variables, selected so that the product of pairs of velocity and force variables is power. The velocity variables include the velocity in the radial, tangential, and circumferential directions and the angular velocities about the axial and circumferential directions. The force variables include the membrane extensional force, in-plane and transverse shear forces, and moments about the axial and circumferential directions. The state-vector approach leads to matrix equations in the form

$$\frac{d\mathbf{X}(z,n)}{z} = A(n)\mathbf{X}(z,n) + B(n)\mathbf{Y}(z,n)$$

and

$$C(n)\mathbf{X}(z,n) + D(n)\mathbf{Y}(z,n) = 0$$

where X(z,n) is the state vector, z is the axial direction, n is the circumferential wave number, Y(z,n) is a secondary state vector, and A(n), B(n), C(n), and D(n) are matrices of shell parameter values, given by equations 9, 10, 11, and 12 of reference 22. These equations can be easily solved for the eigenvalues and eigenvectors as a function of

frequency and circumferential wave number. The eigenvalues provide the desired axial wavenumbers which can be compared with the measured data obtained for this thesis.

The theoretical dispersion relations formulated by Borgiotti and Rosen were programmed into MATLAB by Mark Hayner. Hayner's program sorts the roots of the eigenvalue matrix formulated by Borgiotti into wave types: flexural, compressional, shear, evanescent, and through-thickness. The flexural, compressional and shear roots sorted by Hayner's programs include complex values below the cut-off frequencies. The complex values were removed from the theoretical curves and the remaining real-valued flexural, compressional and shear dispersion curves were constructed. A plot of the normalized axial wavenumber as a function of frequency for mode 0-30 flexural, mode 0 compressional and mode 0 shear waves is shown in Figure A-1.

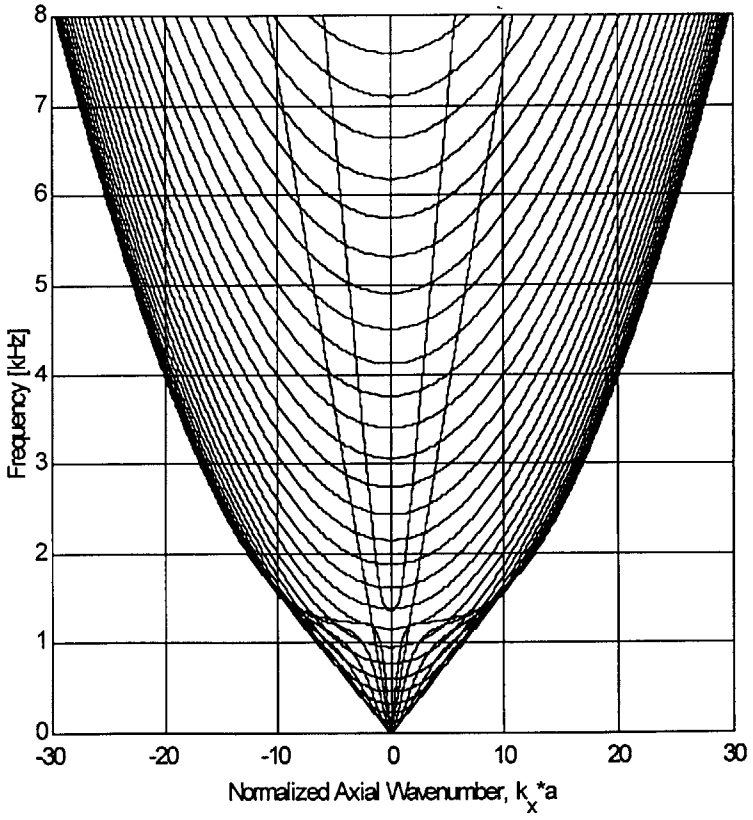

Figure A-1: Theoretical dispersion curves

Appendix B: RAW DATA

B-1 Plain end longitudinal array data

Data on the plain end of the shell was collected at 120 longitudinal array points with the laser Doppler vibrometer. A broad-band random input was generated by the SRS analyzer.

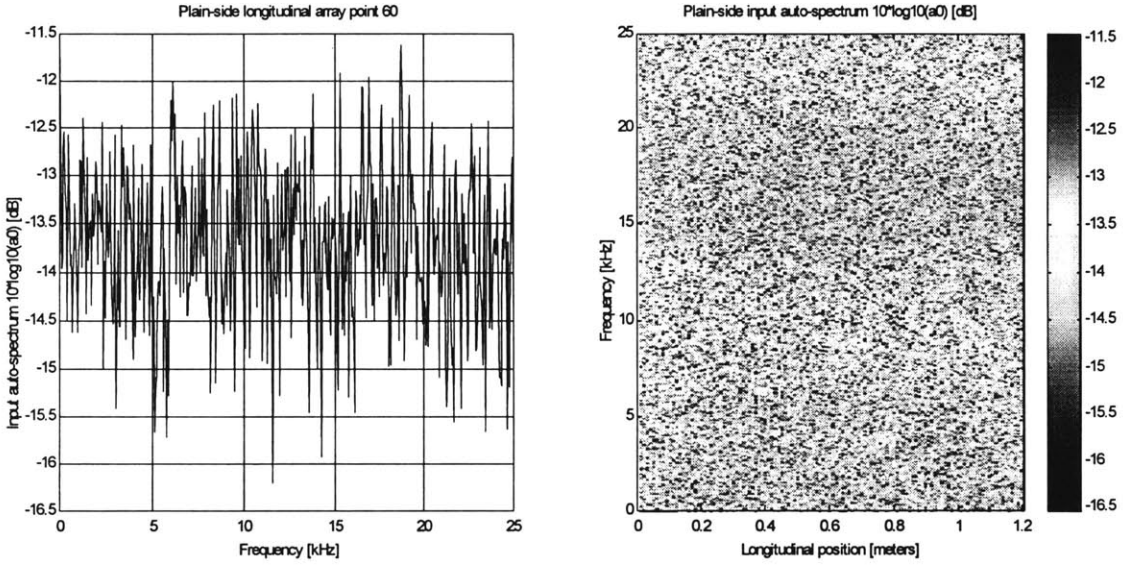

Figure B-1: Input auto-spectra for the plain end longitudinal array measurements

Spectra with 512 frequency lines, a sampling frequency of 50 kHz, a Hanning window, and 30 averages were collected and saved using the ldv system, which outputs a MATLAB file (a2.mat) containing the input and output auto-spectra, the cross-spectrum and the transfer function matrices. An 8 kHz low-pass filter was applied to the input signal after it was measured but before it was sent to the piezo-ceramic sources. The output auto-spectrum, cross-spectrum and transfer function data shown in Figures B-2, B-3 and B-4 are therefore valid only below 8 kHz.

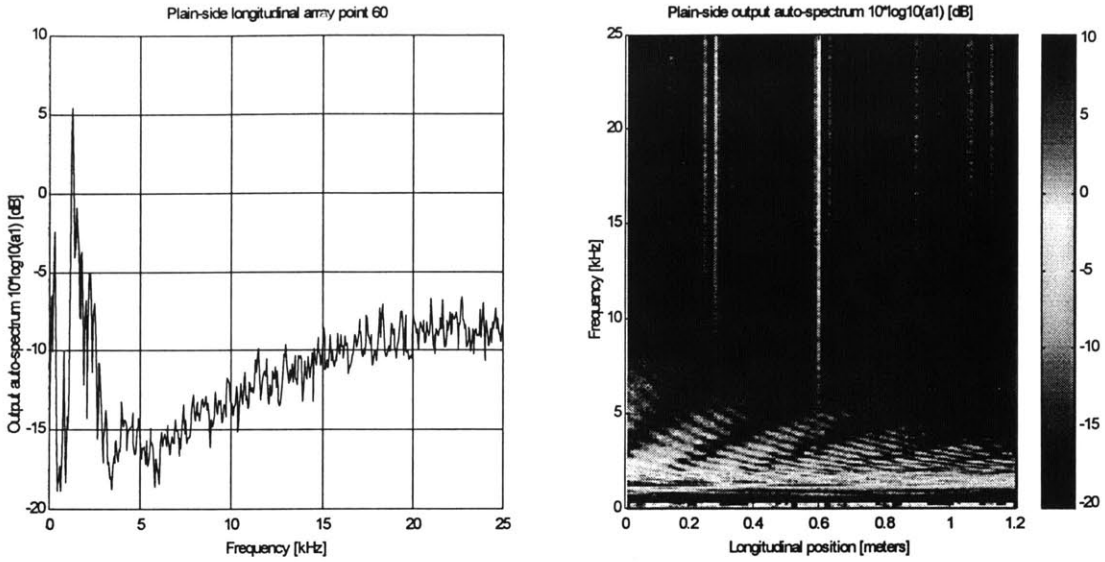

Figure B-2: Output auto-spectra for the plain end longitudinal array measurements

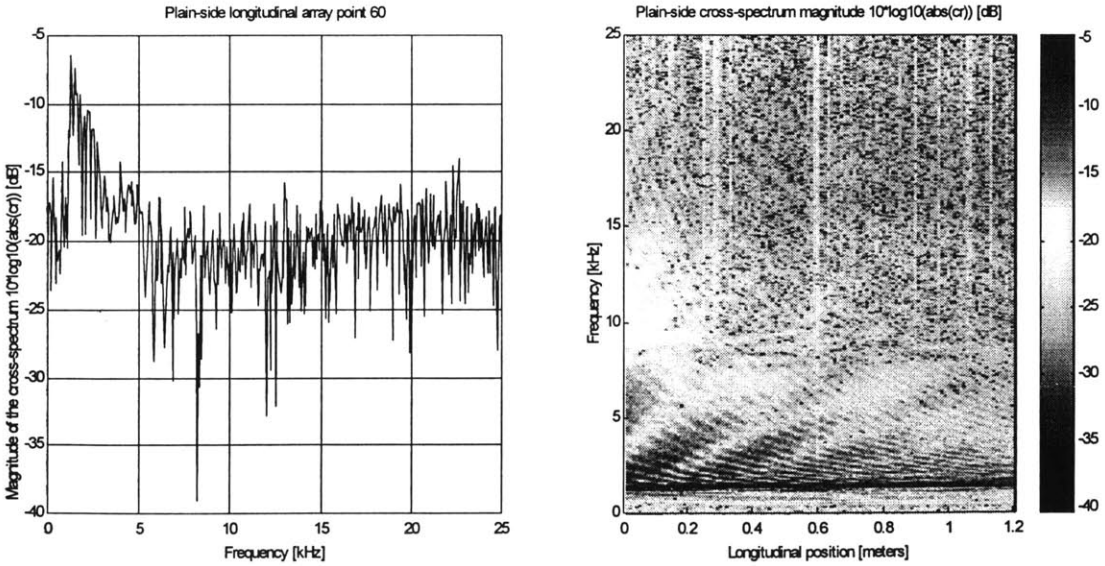

Figure B-3: Cross-spectra for the plain end longitudinal array measurements

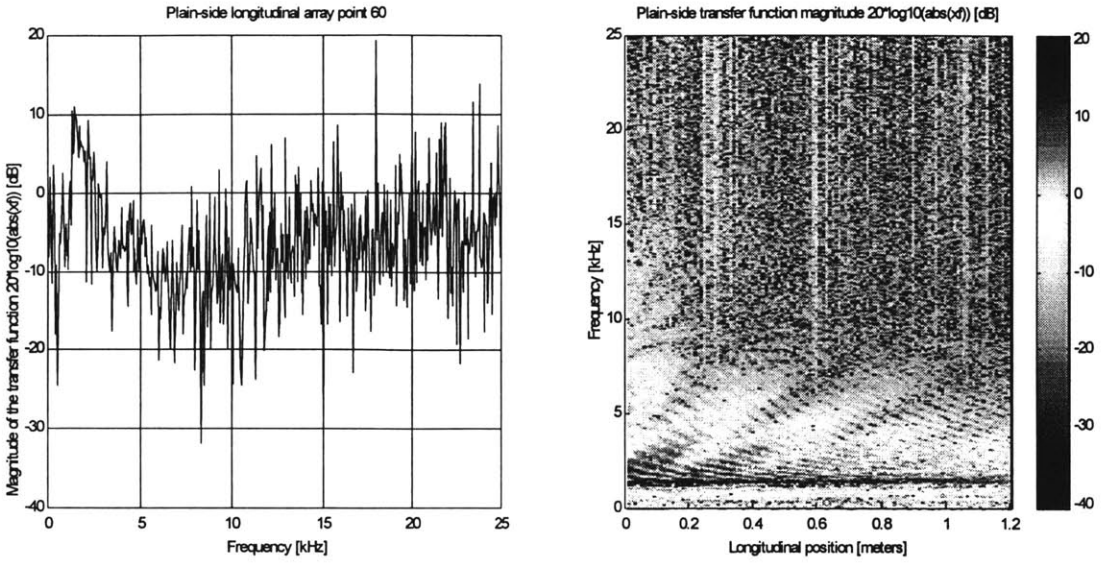

Figure B-4: Transfer function for the plain end longitudinal array measurements

The transfer function matrix calculated by the ldv program is quite noisy. An alternative way to calculate the transfer function is to divide the averaged cross-spectrum by the averaged input auto-spectrum. The phase information is contained in the cross-spectrum and is not lost during the averaging process. Magnitude information is smoothed by the use of the averaged cross-spectrum and averaged input auto-spectrum.

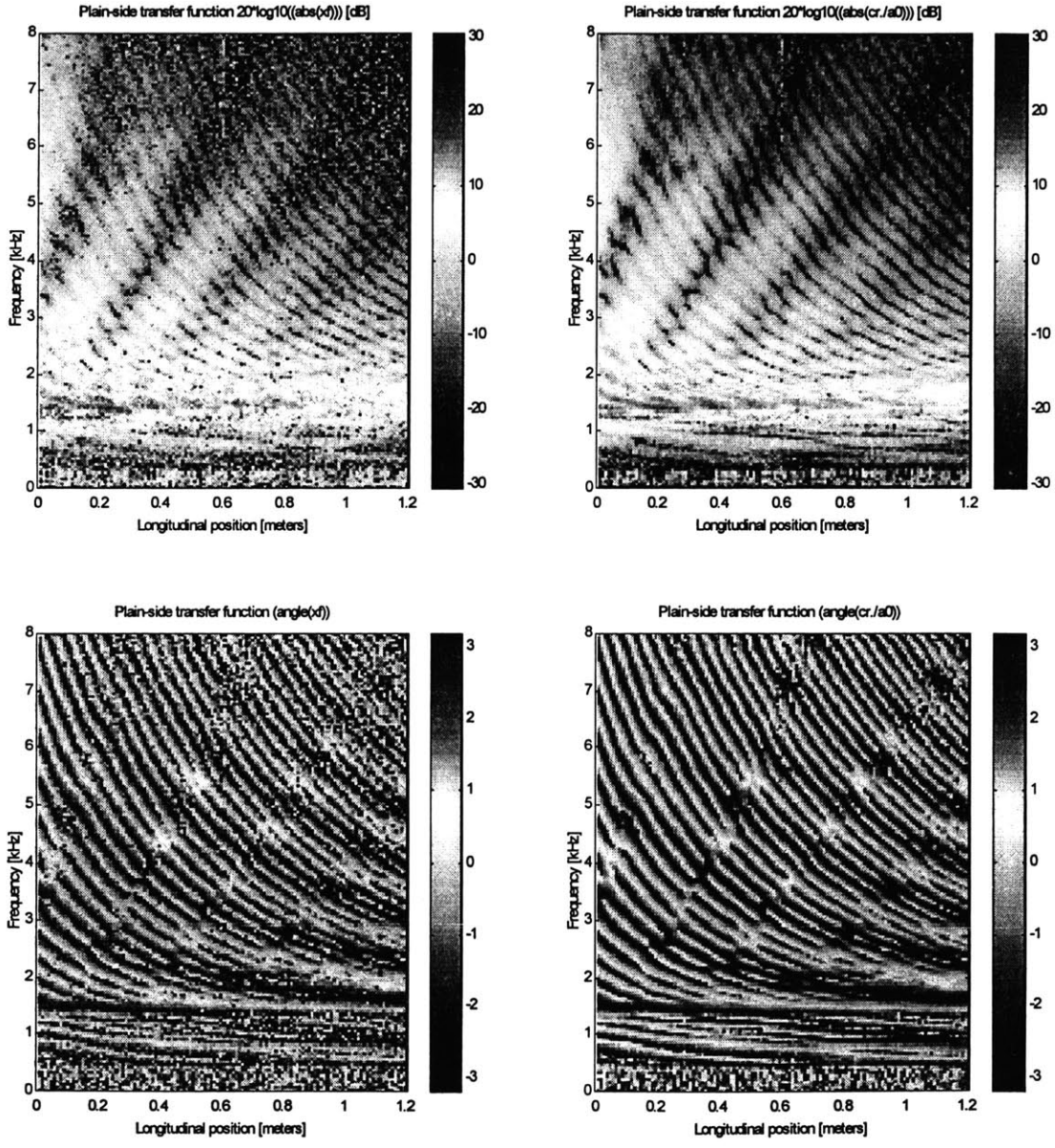

Figure B-5: Transfer function xf vs. cr/a0 for the plain end longitudinal array data

The transfer function matrices were spatially transformed to obtain wavenumber-frequency matrices. A Hanning window and zero-padding (256 points) were used to minimize edge effects and to smooth the data. The wavenumber-frequency matrices show the radial velocity response per unit volt input in dB. Use of the calculated transfer function cr/a0 reduces the noise in the wavenumber-frequency diagram considerably. The data presented in the main chapters of this thesis is based on the calculated transfer function cr/a0.

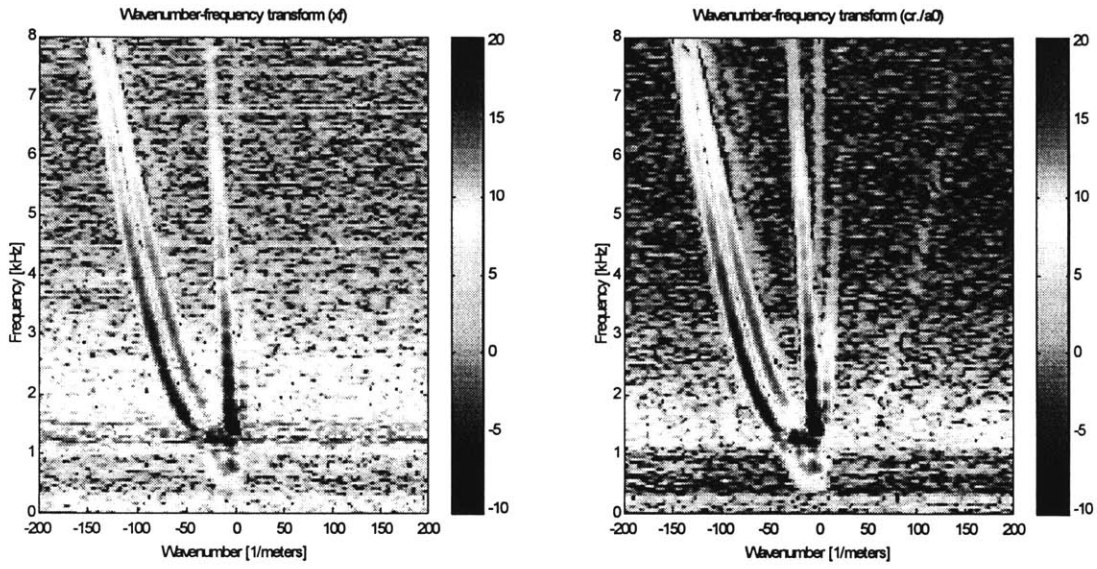

Figure B-6: Plain end longitudinal array wavenumber-frequency matrices: xf from ldv program (left) and calculated transfer function, cr/a0 (right)

B-2 Keel end longitudinal array data

The collection and processing of the keel-end longitudinal array data was identical to that of the plain-end data. Data on the keel end of the shell was collected at 120 longitudinal array points with the laser Doppler vibrometer. A random input was generated by the SRS analyzer.

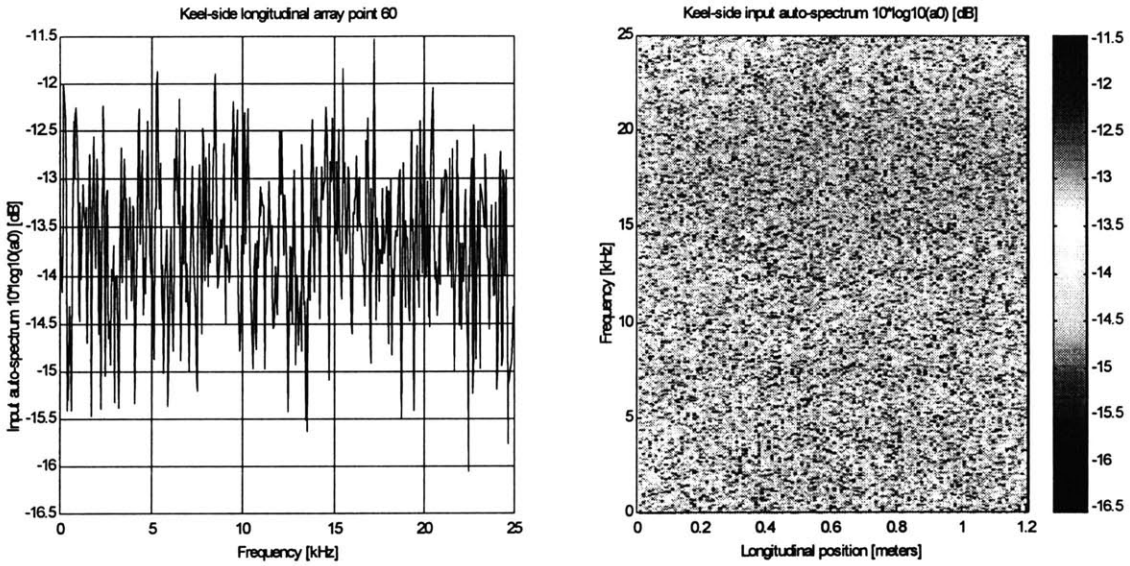

Figure B-7: Input auto-spectra for the keel end longitudinal array measurements

Spectra with 512 frequency lines, a sampling frequency of 50 kHz, a Hanning window, and 30 averages were collected and saved using the ldv system, which outputs a MATLAB file (a2.mat) containing the input and output auto-spectra, the cross-spectrum and the transfer function matrices. An 8 kHz low-pass filter was applied to the input signal after it was measured but before it was sent to the piezo-ceramic sources. The output auto-spectrum, cross-spectrum and transfer function data shown in Figures B-8, B-9 and B-10 are therefore valid only below 8 kHz. The stripes in the output autospectrum were determined to be caused by dust on the reflective tape mounted on the shell at the measurement locations. The response of the dust appears to be frequency dependent, with more response at higher frequencies.

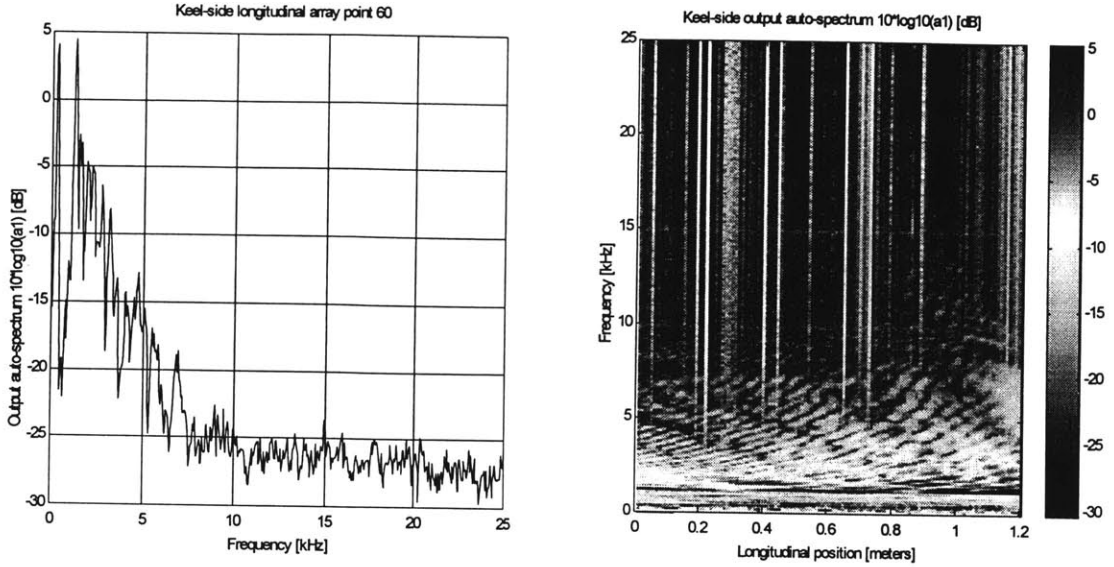

Figure B-8: Output auto-spectra for the keel end longitudinal array measurements

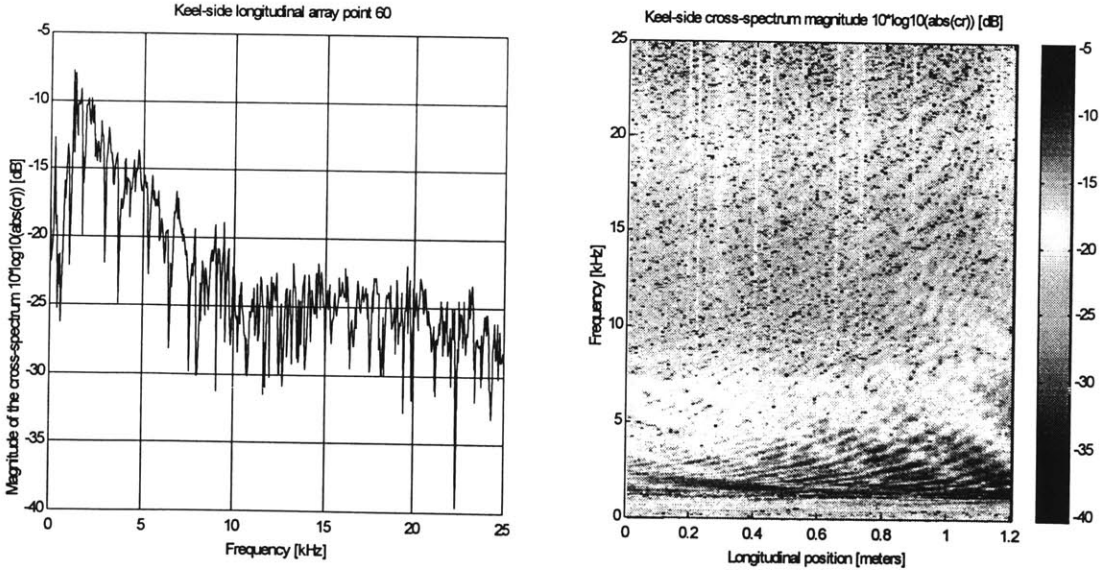

Figure B-9: Cross-spectra for the keel end longitudinal array measurements

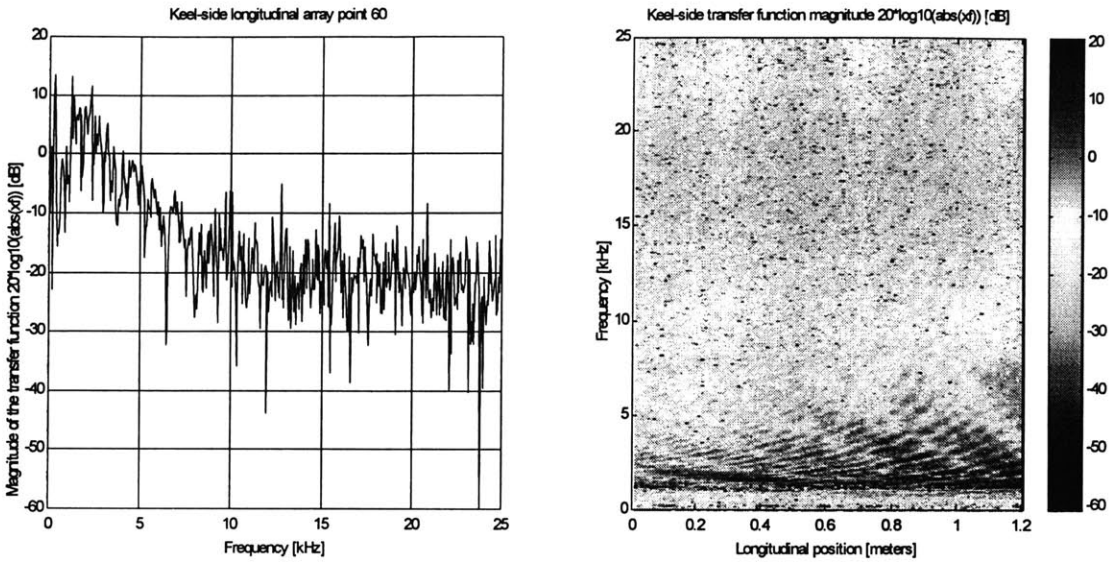

Figure B-10: Transfer function for the keel end longitudinal array measurements

The transfer function matrix calculated by the ldv program is quite noisy. An alternative way to calculate the transfer function is to divide the averaged cross-spectrum by the averaged input auto-spectrum. The phase information is contained in the cross-spectrum and is not lost during the averaging process. Magnitude information is smoothed by the use of the averaged cross-spectrum and averaged input auto-spectrum.

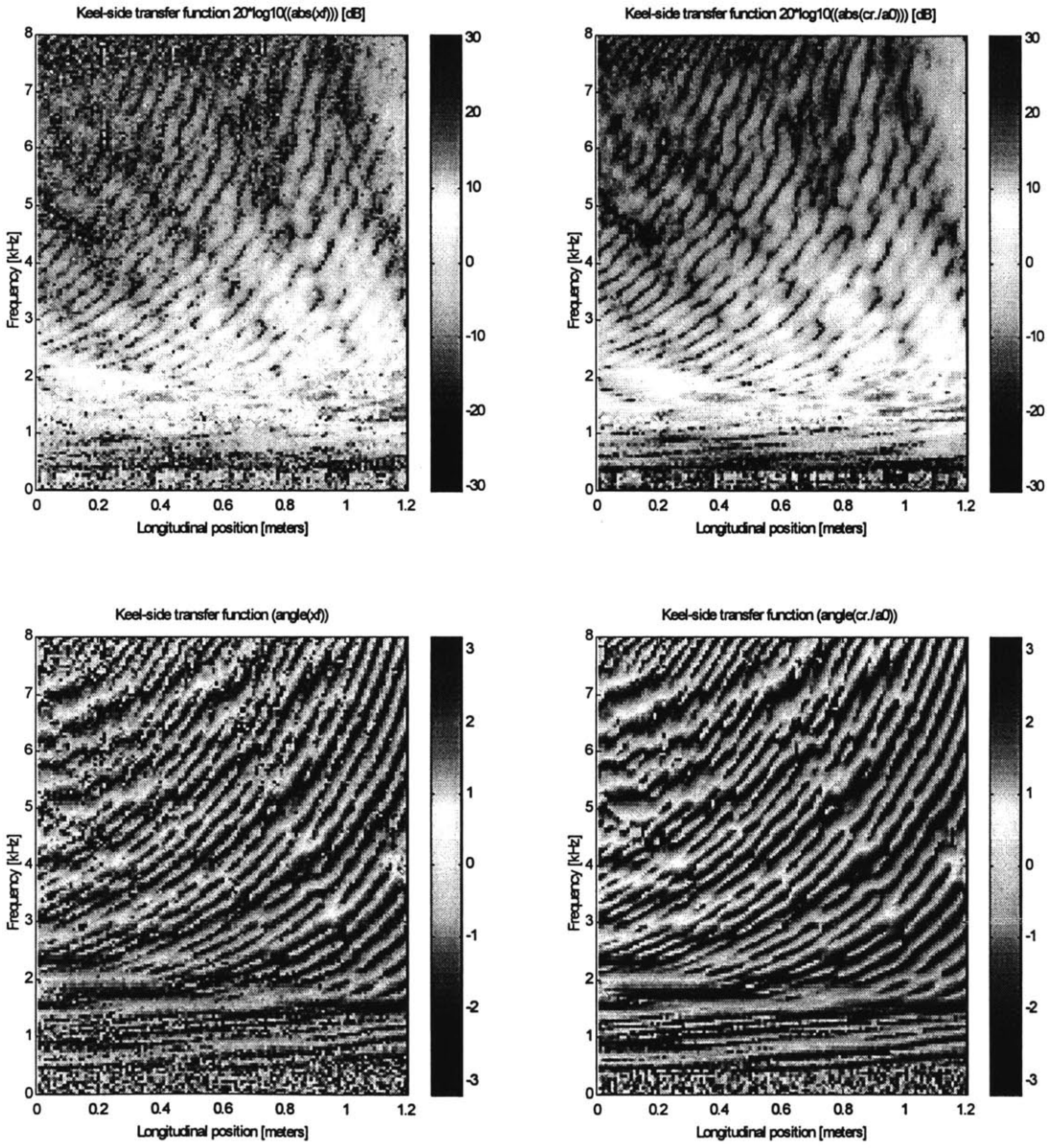

Figure B-11: Transfer function xf vs. cr/a0 for the keel end longitudinal array data

The transfer function matrices were spatially transformed to obtain wavenumber-frequency matrices. A Hanning window and zero-padding (256 points) were used to minimize edge effects and to smooth the data. The wavenumber-frequency matrices show the radial velocity response per unit volt input in dB. Use of the calculated transfer function cr/a0 reduces the noise in the wavenumber-frequency diagram considerably. The data presented in the main chapters of this thesis is based on the calculated transfer function cr/a0.

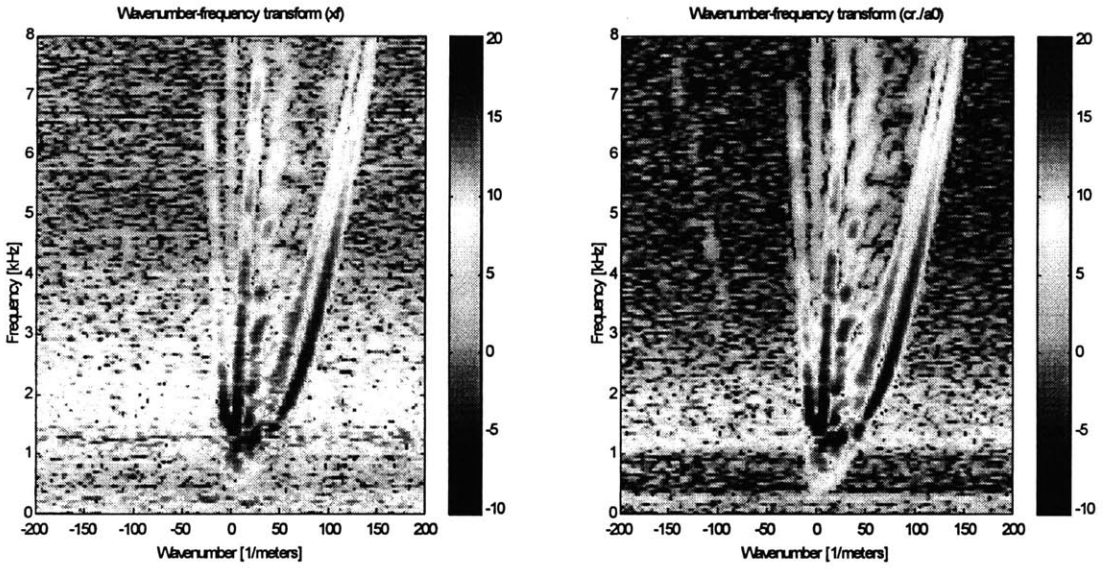

Figure B-12: Keel end longitudinal array wavenumber-frequency matrices: xf from ldv program (left) and calculated transfer function, cr/a0 (right).

B-3 Keel end circumferential array data

The data processing for the circumferential arrays was conceptually the same as the data processing for the longitudinal arrays, but a commercial analyzer was used to collect and save the data instead of the ldv program. For the keel end data, the input and output autospectra and the cross-spectrum were collected with 100 averages, a Hanning window, and a maximum un-aliased frequency of 12.8 kHz. Data was collected at 125 measurement locations, one at a time, and saved onto a floppy in the analyzer's proprietary format. An 8 kHz low-pass filter was applied to the input signal after it was measured but before it was sent to the piezo-ceramic sources. The output auto-spectrum, cross-spectrum and transfer function data shown in Figures B-14, B-15 and B-16 are therefore valid only below 8 kHz.

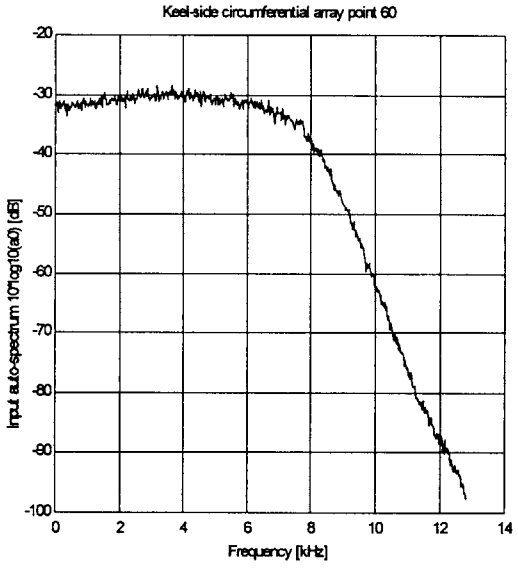

Figure B-13: Input autospectrum for keel end circumferential array point 60

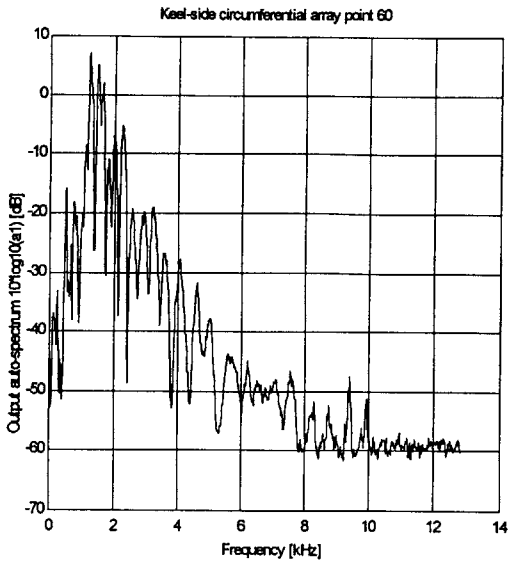

Figure B-14: Output autospectrum for keel end circumferential array point 60

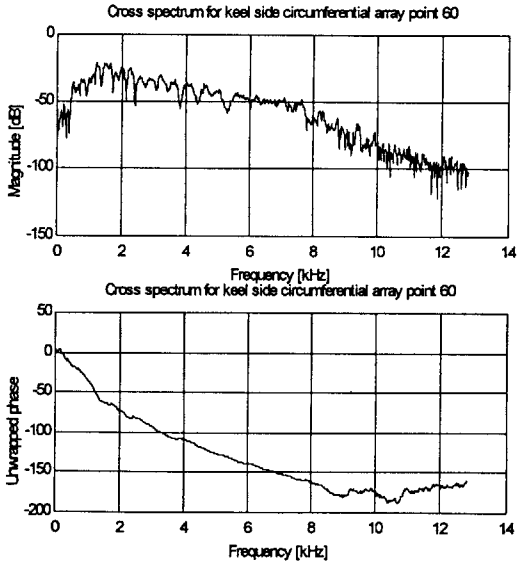

Figure B-15: Cross-spectrum for keel end circumferential array point 60

The input and output autospectra and the cross spectrum were translated into MATLAB. The transfer function at each measurement location was calculated by dividing the averaged cross-spectrum by the averaged input auto-spectrum. This form of the transfer function, commonly called H1, is preferred when noise is present in the output signal [31]. The phase information is contained in the cross-spectrum and is not lost during the averaging process. Magnitude information is smoothed by the use of the averaged cross-spectrum and averaged input auto-spectrum.

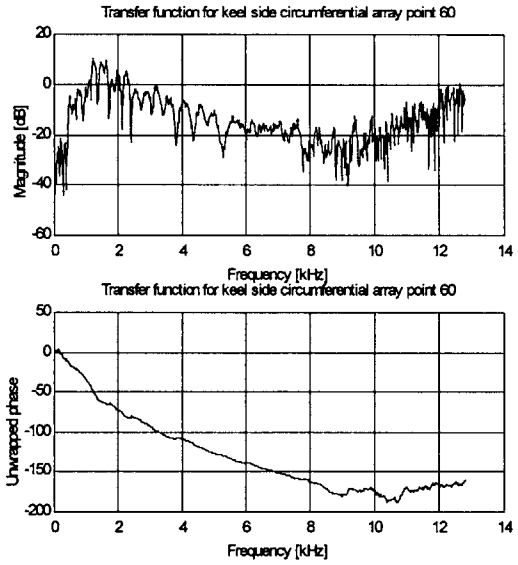

Figure B-16: Transfer function h1 = <cr>/<a0> for keel end circumferential array point 60

The 125 transfer functions were assembled into a matrix which was spatially transformed to obtain the wavenumber frequency transform. The circumferential arrays went all the way around the shell, so the assumption that the spatial sample is periodic made when taking the Fourier transform is true. Therefore, no window was applied to the data and no zero-padding was used. The wavenumber-frequency matrices show the radial velocity response per unit volt input in dB.

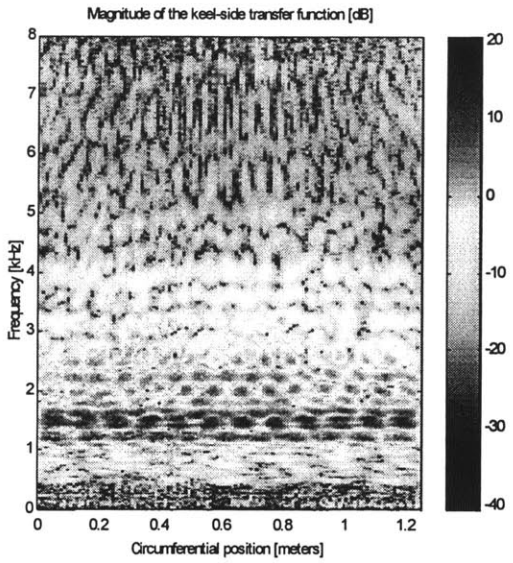

Figure B-17: Magnitude and unwrapped phase of the transfer function matrix for the keel end circumferential array

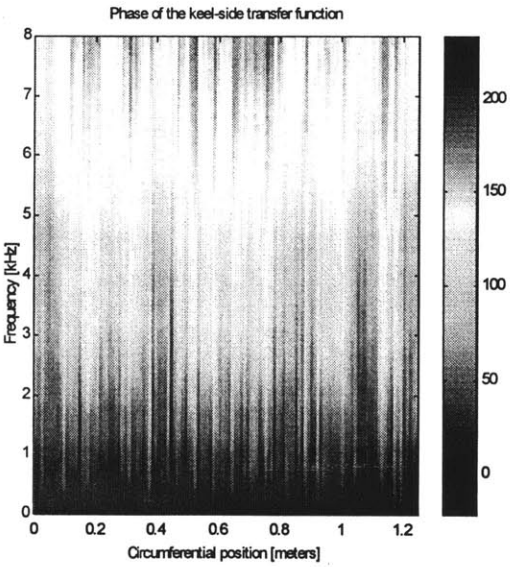

Figure B-18: Unwrapped phase of the transfer function matrix for the keel end circumferential array

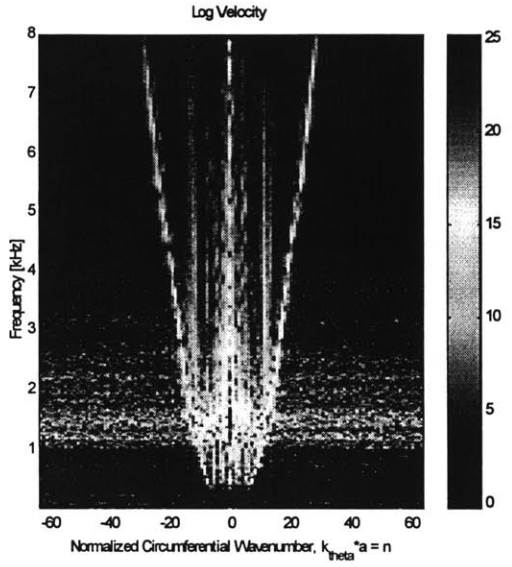

Figure B-19: Magnitude of the wavenumber frequency transform for the keel end circumferential array

B-4 Plain end circumferential array data

The data processing of the plain end circumferential array data was conceptually the same as the processing of the keel end data, but a different form of the transfer function was used. The commercial analyzer used to collect and save the data provided two forms of the transfer function; <F2/F1> and <F2>/<F1>, where F1 is the spectrum of the input and F2 is the spectrum of the output. Data was collected at each measurement point one at a time, and both forms of the transfer function were saved onto a floppy.

Neither of these forms of the transfer function were ideal, however. <F2/F1> maintained phase relationships, but did nothing to reduce the noise in the output signal. <F2>/<F1> reduced the noise considerably, but lost the phase. The magnitude of the wavenumber-frequency transform calculated with the first form is very noisy. On the other hand, the magnitude of the wavenumber-frequency transform calculated with the second form contains 'data' at zero wavenumber and at twice the wavenumber of the real data, artifacts of the processing. In future work, neither of these forms of the transfer function should be used. The H1 transfer function [31], <cr>/<a0> works best to eliminate noise in the output and preserves phase.

For the plain-end circumferential array, data was collected at 125 points around the circumference, 1 centimeter apart, to cover almost 360 degrees around the shell. A random input was generated by the SRS analyzer. The input and the response measured by the laser Doppler vibrometer were Fourier transformed and saved by the SRS analyzer. Spectra with 801 frequency lines were collected out to an un-aliased maximum frequency of 12.5 kHz. A Hanning window was applied and 100 averages were taken.

The two forms of the transfer function saved by the analyzer, <F2/F1> and <F2>/<F1>, are shown below for point 60 on the circumferential array. Because the source was newly generated for each measurement, the phase of the input was random over the 125 measurement points. Averaging of the input spectrum therefore averaged out the

phase. The same loss of phase occurred for the response spectrum, so that the <F2>/<F1> transfer function did not contain any phase information.

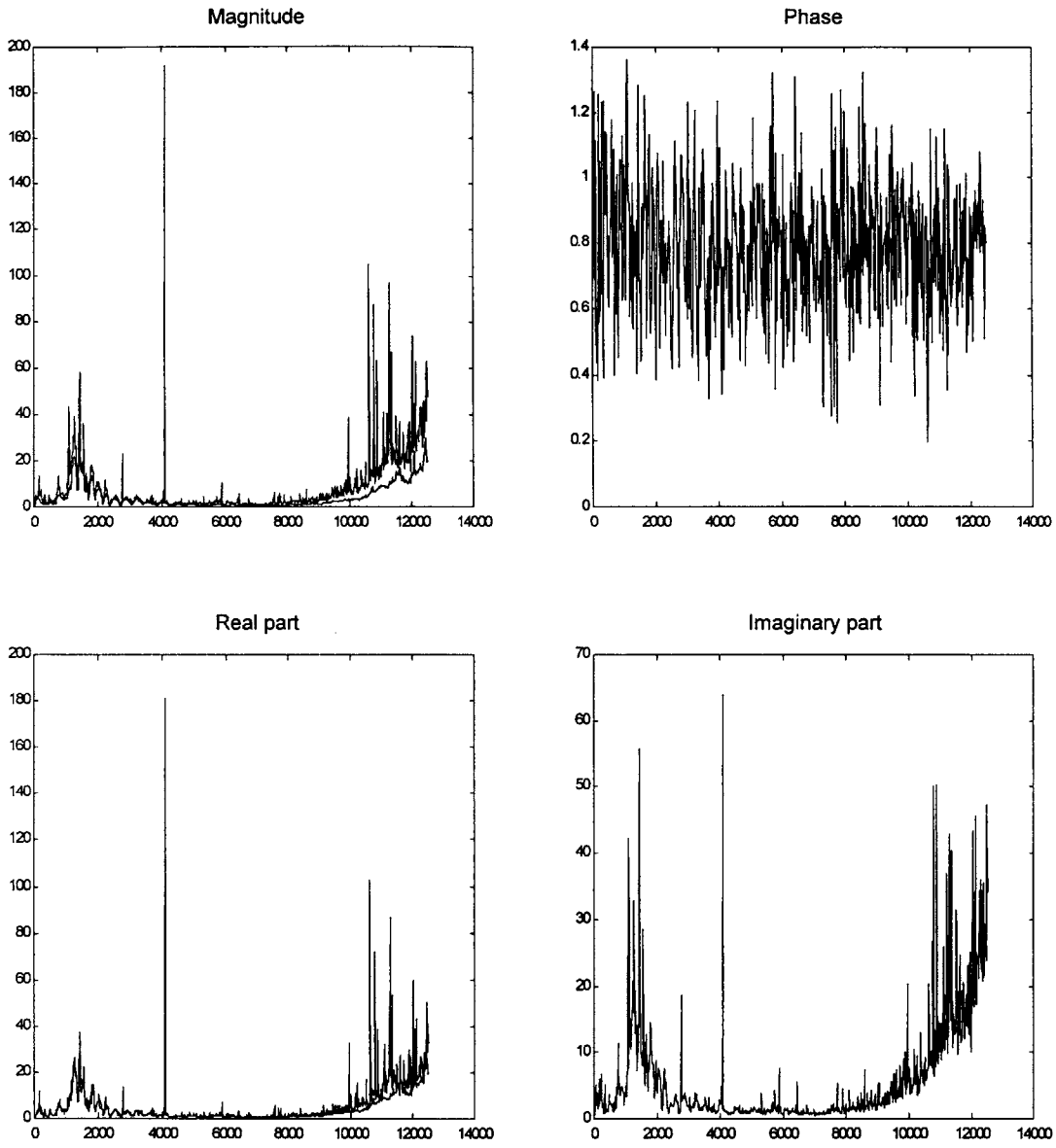

Figure B-20: Two forms of the transfer function saved by SRS

An 8 kHz low-pass filter was applied to the input signal after it was measured but before it was sent to the piezo-ceramic sources. The transfer functions shown in Figure B-20 above are therefore valid only below 8 kHz.

Transfer function <F2/F1> was not saved for point 21. Data from point 20 was substituted. The measurement locations were closely spaced relative to the measured wavelengths, so that the transfer functions for two consecutive locations were quite similar.

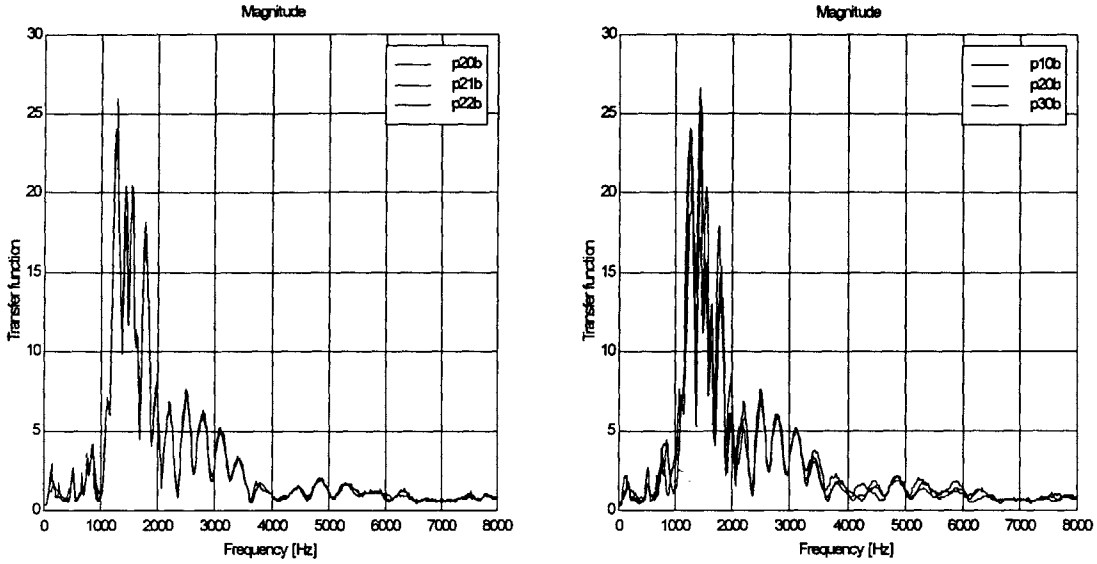

Figure B-21: Variation of pnb data for points 20, 21 & 22 and 10, 20 & 30.

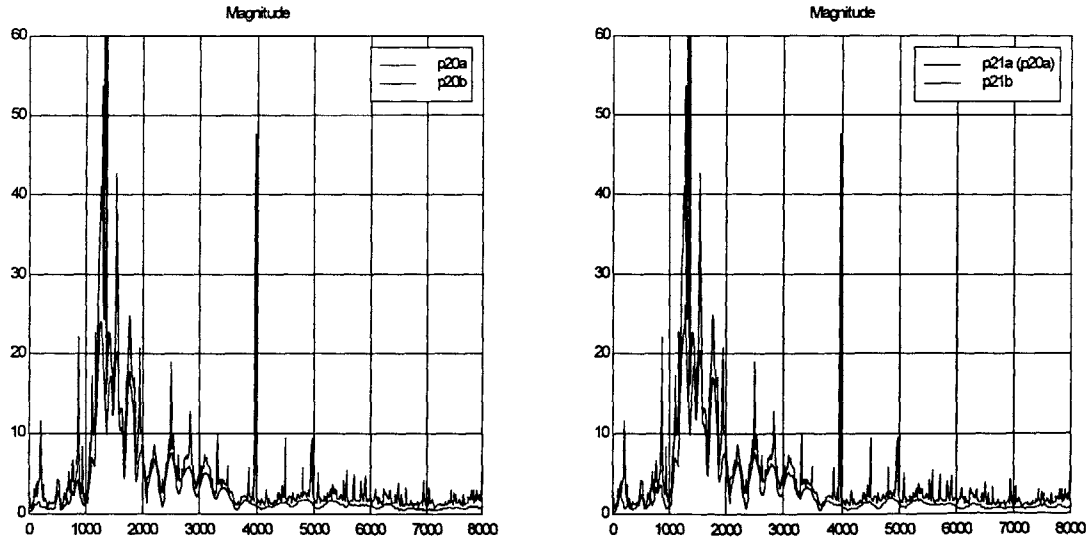

Figure B-22: Substitution of p20a data for missing p21a data.

The transfer function files were translated into MATLAB format using 'translate.m' which runs the SRS translation program 'srtrans.exe'. The resulting files were assembled into two transfer function matrices, one for each form of the transfer function, 'pna' and 'pnb', using 'assemble.m', which created files 'pna.mat' and 'pnb.mat'.

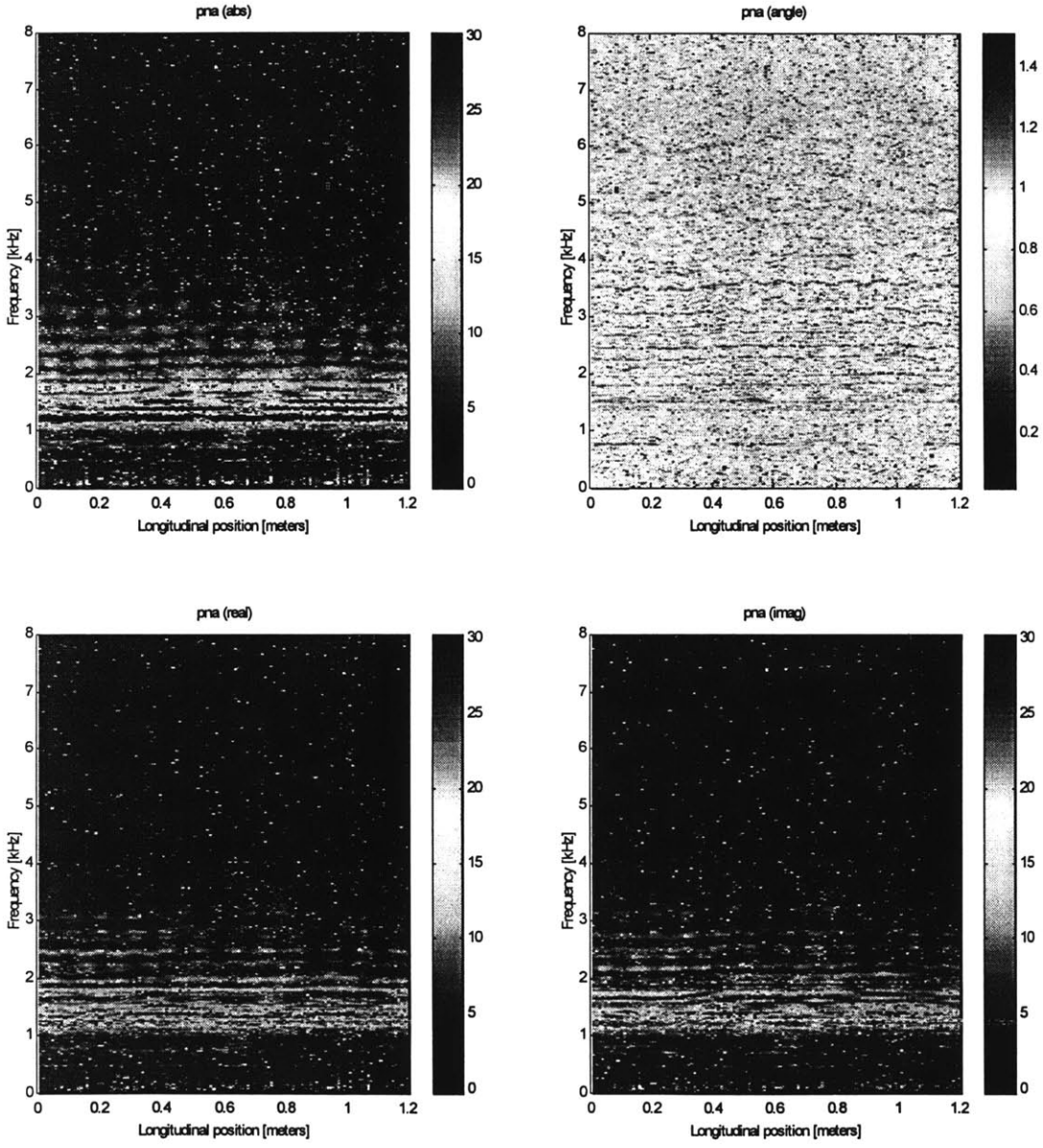

Figure B-23: Transfer function matrices for the plain-end circumferential array

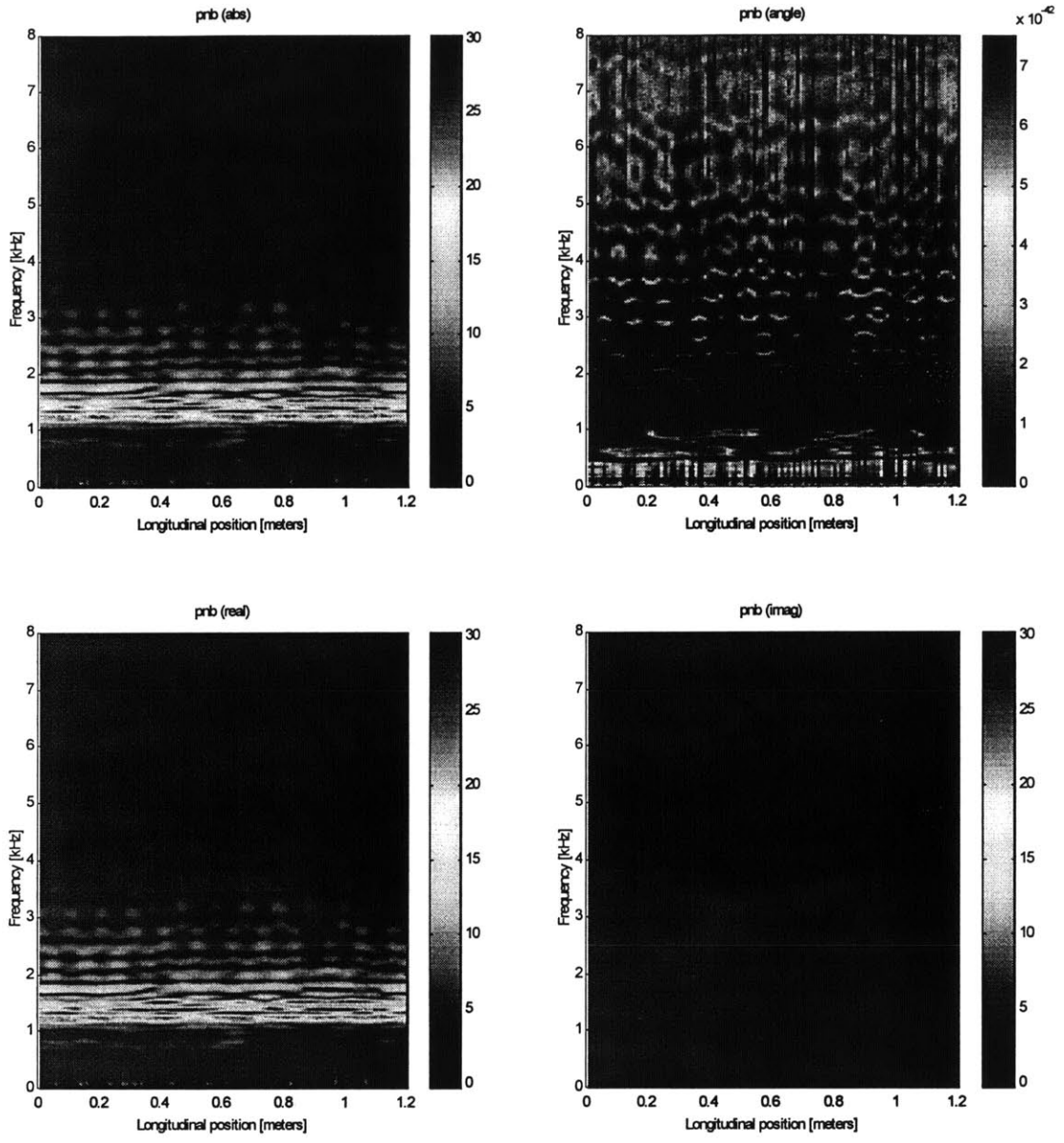

Figure B-24: Transfer function matrices for the plain-end circumferential array

Replotting the transfer functions in decibels shows their character more clearly. The averaged transfer function matrix <F2/F1> is quite noisy. The transfer function calculated from the averaged input and response spectra, <F2>/<F1>, has a much cleaner magnitude, but the phase is lost.

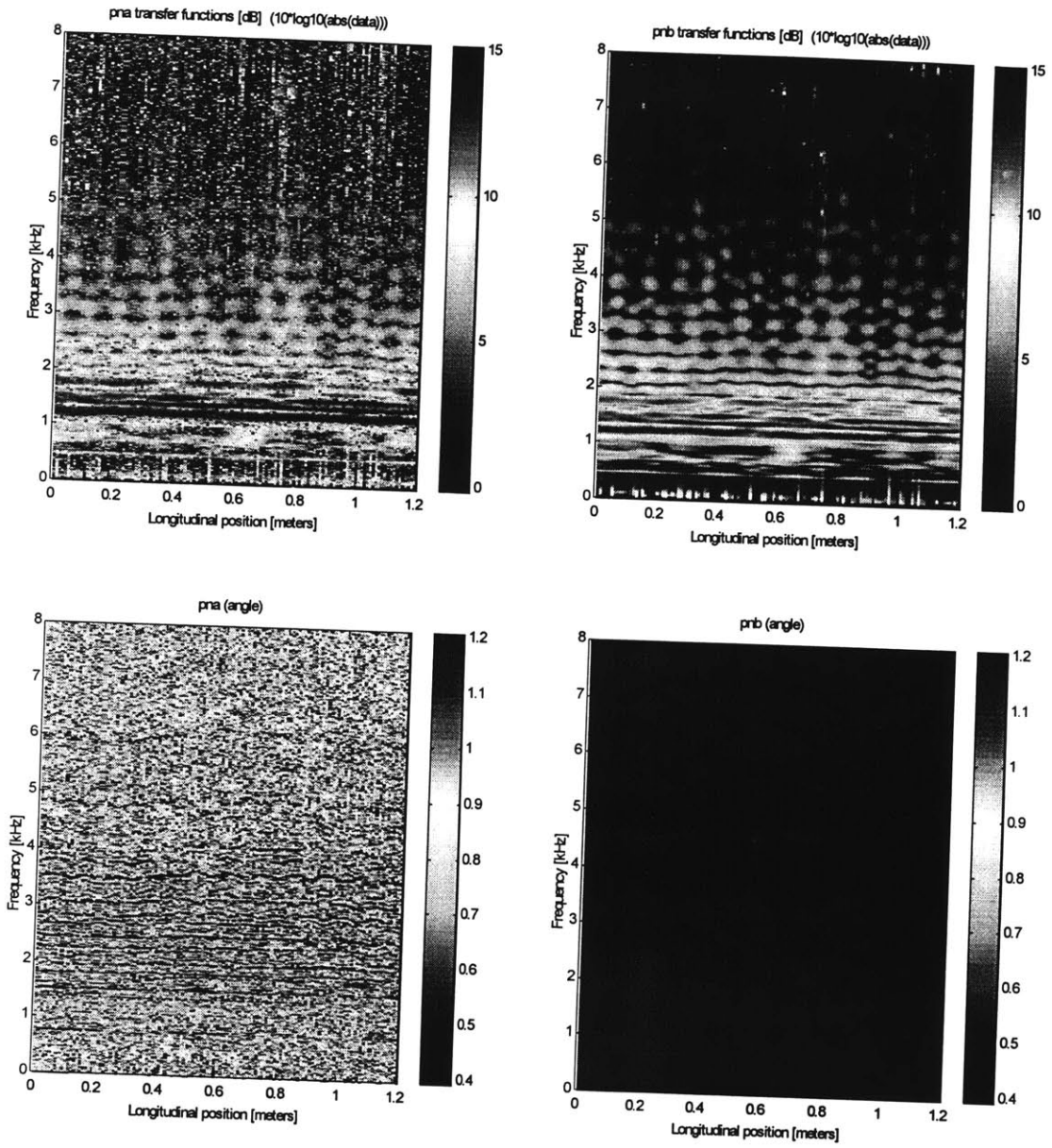

Figure B-25: Transfer function matrices for the plain-end circumferential array

The transfer function matrices were spatially transformed to obtain wavenumber-frequency matrices. The circumferential arrays went all the way around the shell, so that the assumption that the spatial sample is periodic made when taking the Fourier transform is true. Therefore, no window was applied to the data and no zero-padding was used. The wavenumber-frequency matrices show the radial velocity response per unit volt input in dB. Use of the transfer function <F2>/<F1> reduces the noise in the

wavenumber-frequency diagram considerably, but puts an artificial spike at zero wavenumber.

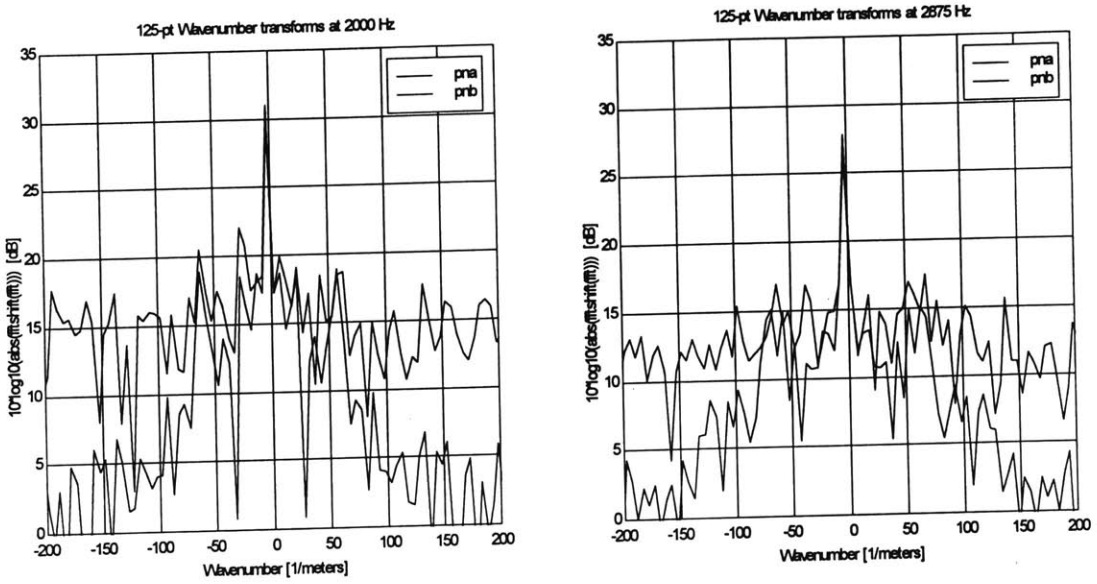

Figure B-26: Spatial transforms of the 2000 Hz and 2875 Hz data

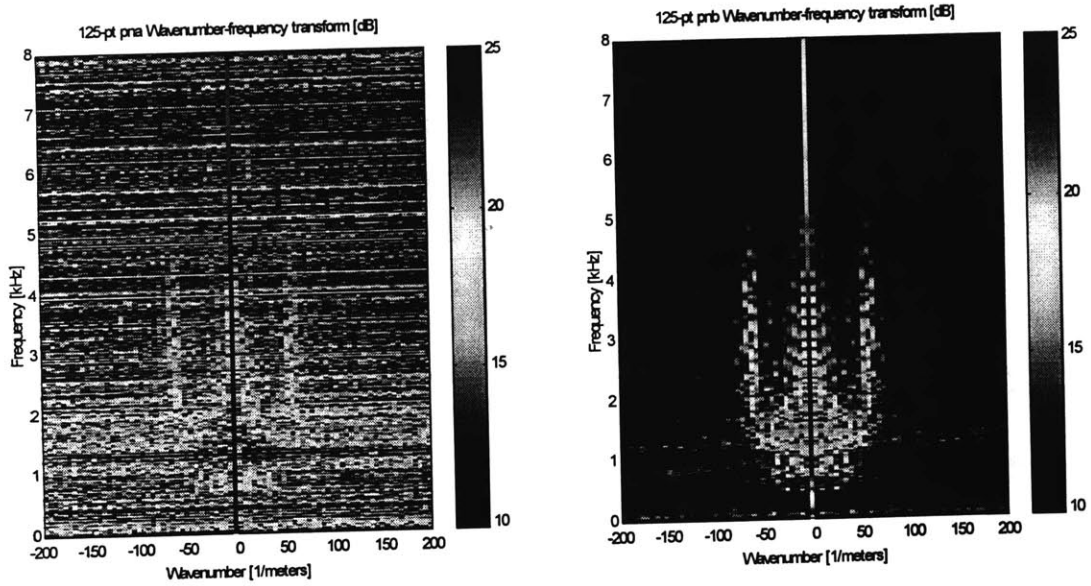

Figure B-27: Wavenumber-frequency matrices for the plain-end circumferential array

2991-74